Stresses and strains frozen into optical fibers

A. D. Yablon

OFS: 600 Mountain Avenue, Room 7E-226, Murray Hill, NJ 07974-0636
Voice: 908-582-1958, Fax: 908-582-2913, Email: ayablon@ofsoptics.com

Abstract: In addition to residual elastic stresses and strains, viscoelasticity can also be frozen into optical fibers. Frozen-in viscoelasticity affects guiding properties of optical fibers and has been harnessed to produce all-fiber fundamental mode beam expanders.
©2004 Optical Society of America

1. Introduction

Both draw-induced and thermally-induced residual elastic stresses and strains in optical fibers have been extensively discussed in numerous publications stretching back to the earliest days of optical fiber technology [1-5]. Residual elastic strains are local deformations resulting from residual stresses, which are stresses inside the fiber that persist even when no external forces are applied to the fiber. Residual elastic stresses and strains are important primarily because they perturb the fiber's refractive index profile [4], thus altering its waveguiding characteristics, although they can also affect the mechanical strength and reliability of optical fibers [5,6]. Most polarization-maintaining (PM) optical fibers derive their birefringence from desirable residual elastic stresses and strains, while undesirable residual elastic stresses and strains have been cited as a source of polarization-mode-dispersion (PMD) in non-PM fibers [7].

Residual elastic stresses and strains result from heterogeneities in the fiber's physical structure; for example the presence of a core and cladding, with corresponding differences in viscosity and/or thermal expansion coefficient. Several different models describe how residual stresses and strains arise from heterogeneities in the fiber's structure, but these can be summarized into two general categories: thermal and draw-induced (also termed mechanical). Thermal stresses primarily arise from non-uniformities in the thermal expansion coefficient of the fiber whereas draw-induced residual stresses primarily arise from non-uniformities in the viscosity of the fiber.

Recently, an important "new" source of draw-induced refractive index perturbations, *frozen-in viscoelasticity*, was identified [8]. Frozen-in viscoelasticity is distinct from residual stresses and strains in that it is a "stress-free" perturbation to the room temperature glass. In contrast to residual stresses and strains, frozen-in viscoelasticity can significantly perturb the refractive index of a homogeneous glass fiber exhibiting uniform viscosity and uniform thermal expansivity. Frozen-in viscoelasticity primarily affects the highest-viscosity portion of conventional silica optical fibers, which is typically the pure silica cladding. Frozen-in viscoelasticity can also serve as the basis for novel optical fiber devices. Although the ceramics community has been aware of frozen-in strains for some time [9-11], its importance to the optical fiber community has only recently been recognized and quantified [8].

2. Theory

High temperature silica is a viscoelastic material, meaning that it responds to an applied load (such as draw tension) with an instantaneous (termed "elastic") as well as a time-dependent (termed "relaxational") deformation. These deformations can be further specified as deviatoric, which are shape changing, or dilatational, which are density and volume changing. Prior analyses of optical fiber viscoelasticity did not consider the time-dependence of the dilatation and consequently they were only capable of predicting conventional residual elastic stresses and strains in room temperature fibers [3]. When a fiber under tension is rapidly cooled through its glass-forming (or "fictive temperature") regime, the time-dependent ("relaxational") portion of the tension-induced dilatation is frozen and cannot relax when the tension is removed from the room temperature fiber. This results in a "stress-free" density, and hence refractive index, perturbation in the room temperature silica glass. This refractive index perturbation is notable for its low degree of birefringence; the isotropic portion of the refractive index perturbation is much larger than the anisotropic portion [8]. The refractive index perturbation can be reversed by briefly heating the fiber to a temperature close to, or above, its fictive temperature in the absence of any applied forces.

Varying the cooling rate of most glasses induces a "stress-free" room temperature density (and hence refractive index) perturbation because the cooling rate controls the glass-forming temperature, which in turn controls the room temperature density of the sample [11]. However, high-purity (low–OH) silica is known to be an exception since it exhibits a broad room-temperature density maximum [12] in the vicinity of practical optical fiber glass-forming

temperatures [2], meaning that the room temperature refractive index, is largely independent of cooling rate. Refractive index perturbations in silica optical fibers resulting from cooling rate (and hence glass-forming temperature) shifts are estimated to be on the order of 1×10^{-5}, which is more than an order of magnitude smaller than the refractive index changes resulting from residual stress and strains or frozen-in viscoelasticity.

The refractive index perturbation viscoelastically frozen into the cladding of a pure-silica clad fiber, Δn, can be derived from the properties of high-purity silica to be [8,13]

$$\Delta n = -6.35\times10^{-6}\sigma \qquad (1)$$

where σ is the effective draw tension in units of MPa. This relation differs slightly from that in [8] since it was computed using data provided in [14] rather than [15]. Figure 1 compares the annealing-induced index change measured using the Transverse Interferometric Method (TIM) [16] to the magnitude of Eq. (1) for several different high-purity silica fibers drawn at different draw tensions. Some of the fibers included a (low-viscosity) doped core, in which case the pure-silica cladding index change is plotted, while others were homogeneous. The plot includes measurements of both $\Delta n_\perp$ and Δn_z, which are the annealing-induced index changes experienced by optical waves polarized transversely and parallel to the fiber axis, respectively. The difference between these quantities, which is the birefringence of the frozen-in refractive index perturbation, is seen to be small.
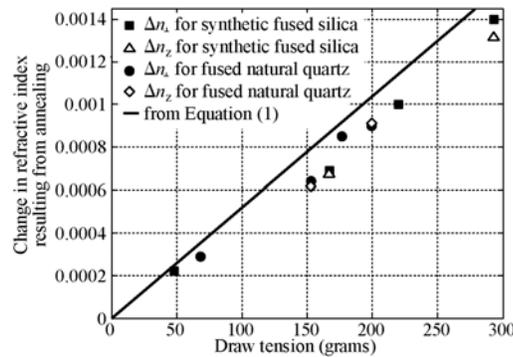

Fig. 1. Annealing-induced index change measured in a 125 μm diameter fiber compared to Eq. (1).

At high draw tensions ($\geq$220 g), large refractive index perturbations ($\geq 1\times10^{-3}$) are induced in the pure silica cladding of conventional 125 μm diameter optical fibers, in addition to refractive index perturbations induced by residual elastic stresses and strains. Unlike the refractive index perturbations induced by residual elastic stresses and strains, index perturbations induced by frozen-in viscoelasticity cannot be readily detected with a polarscope [7]. Moreover, many commercial optical fiber refractive index profilers erroneously assume that the refractive index of the pure silica cladding is constant and independent of draw tension. These facts help to explain why the optical fiber community has overlooked frozen-in viscoelasticity.

We have found that we can modify the viscoelasticity frozen into optical fibers by cooling down an already-drawn fiber from a temperature near its fictive temperature while maintaining a controlled tension on the fiber. Proper control of the processing conditions can minimize deformation of the fiber (viscous flow) while substantially changing the fiber's refractive index profile. These changes to the fiber's refractive index profile can be made relatively rapidly along the fiber's length, over distances on the order of a fiber diameter.

3. Application to Beam Expanders and High-Power Connectors

Frozen-in viscoelasticity was recently harnessed to fabricate all-fiber high-performance fundamental mode beam expanders. Tailoring the dopant concentration of an MCVD preform permits the fabrication of an optical fiber whose refractive index profile is particularly sensitive to the frozen-in viscoelasticity. Both residual elastic stresses and strains as well as frozen-in viscoelasticity contribute to the refractive index profile, and hence the optical performance, of these beam expanders. The as-drawn 125 μm diameter fiber exhibits an index profile and mode-field diameter similar to standard single-mode fiber (Fig. 2, solid line in plot), while a special heat treatment applied to the drawn fiber alters the frozen-in viscoelasticity, as well as the residual elastic stresses and strains, to yield an index profile similar to a step index multimode fiber (Fig. 2, dashed line in plot) [13,17]. Optimized fiber processing conditions yield transition zones that adiabatically couple the mode-field from the as-drawn single-mode region into the fundamental LP_{01} modefield of the multimode fiber region.
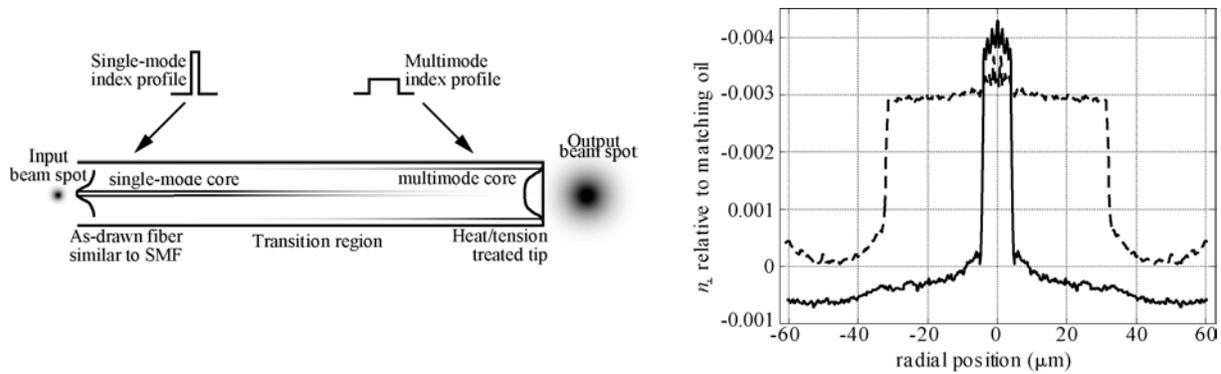
Fig. 2. Schematic illustration of all-fiber beam expanders fabricated with the aid of frozen-in viscoelasticity (*left*). Refractive index profiles of beam expander fiber: as-drawn (*solid line*) and after brief heat treatment (*dashed line*). [13,17]

The refractive index profiles in Fig. 2 may be directly compared to each other since they were acquired with identical reference oil using TIM. Mechanical equilibrium requires that the residual axial stresses integrate to zero over the fiber's cross section, so if the non-axial residual stresses are assumed to be negligible [5,6] and the elasto-optic properties are assumed to be independent of dopant concentrations, then the integral of the difference in refractive index over the fiber cross section in Fig. 2 should be zero. However, the refractive index change in the small cross sectional area core cannot balance the opposite direction refractive index change observed in the large cross sectional area outside the core so the difference between these index profiles cannot be completely explained by residual elastic axial stresses.

Enlarging the fundamental mode spot size has the dual advantage of reducing the local power density while also increasing the free space collimation range by reducing diffraction. Decreasing the power density increases the damage threshold and thus improves reliability of fibers and components. Increasing the free space collimation range and reducing diffraction can enhance coupling between optical fiber terminations and free space optics (such as MEMS-based switches) or optical sources or detectors. The expanded modefield diameter of these beam expanders is about 40 µm at 1550 nm, which is four times that of the as-drawn fiber or standard single-mode fiber. Coupling losses between two opposing beam expander tips are less than 0.8 dB when separated by an air-gap as large as 800 µm. Several different connectors (LC, FC, SC) were fabricated from such beam expanders and they exhibited losses as good as standard connectors. These beam expanders are suitable for high-volume manufacturing [13,17].

3. References

[1] K. Brugger, "Effect of Thermal Stress on Refractive Index in Clad Fibers," Appl. Opt. **10**, 437-438 (1971).
[2] U. C. Paek and C. R. Kurkjian, "Calculation of Cooling Rate and Induced Stresses in Drawing of Optical Fibers," J. Am. Ceram. Soc. **58**, 330-335 (1975).
[3] G. W. Scherer and A. R. Cooper, "Stress in optical waveguide fibers," in Advances in Ceramics, Volume II, Physics of Fiber Optics, edited by B. Bendow and S. Mitra (American Ceramic Society, Columbus, OH, 1981) 193-203.
[4] G. W. Scherer, "Stress-induced index profile distortion in optical waveguides," Appl. Opt. **19,** 2000-2006 (1980).
[5] L. Rongved, C. R. Kurkjian, F. T. Geyling, "Mechanical tempering of optical fibers," J Non-Crystalline Sol. **42**, 579-584 (1980).
[6] A. K. Varshneya, D. Varshneya, V. Jain, "On 'Mechanical Tempering of Optical Fibers'," J Non-Crystalline Sol. **93**, 215-216 (1987).
[7] Y. Park, U.-C. Paek, D. Y. Kim, "Determination of stress-induced intrinsic birefringence in a single-mode fiber by measurement of the two-dimensional stress profile," Opt. Lett., **27**, 1291-1293 (2001).
[8] A. D. Yablon, M. F. Yan, P. Wisk, F. V. DiMarcello, J. W. Fleming, E. M. Monberg, D. J. DiGiovanni, J. Jasapara, and M. E. Lines, "Anomalous refractive index changes in optical fiber," in Proceedings of the Optical Fiber Communications Conference, Vol. 86 of OSA Proceedings Series (Optical Society of America, Washington, D.C., 2003), Postdeadline paper PD6.
[9] J. F. Stirling, "Frozen Strains in Glass Fibers," J. Soc. Glass Technol., **39**, 134T-144T (1955).
[10] W. H. Otto, "Compaction effects in Glass Fibers," J. Am. Ceram. Soc., **44**, 68-72 (1961).
[11] R. Gardon, "Evolution of Theories of Annealing and Tempering: Historical Perspective," American Ceramic Society Bulletin **66**, 1594-1599 (1987).
[12] R. Bruckner, "Properties and Structure of Glasses and Melts versus Preparation," in *Glass Science and Technology Vol. 4A*, D. R. Uhlmann and N. J. Kreidel, eds. (Academic Press, 1990), Chap. 2.
[13] A. D. Yablon, M. F. Yan, D. J. DiGiovanni, M. E. Lines, S. L. Jones, D. N. Ridgway, G. A. Sandels, I. A. White, P. Wisk, F. V. DiMarcello, E. M. Monberg, and J. Jasapara, "Frozen-in Viscoelasticity for Novel Beam Expanders and High-Power Connectors," accepted for publication in J. of Lightwave Technol.
[14] D. M. Krol, K. B. Lyons, S. A. Brawer, C. R. Kurkjian, Phys. Rev. B **33**, 4196-4202 (1986).
[15] A. Bucaro and H. D. Dardy, J. Appl. Phys. **45**, 5324-5329 (1974).
[16] D. Marcuse, *Principles of Optical Fiber Measurements,* (Academic, Orlando, Fla. 1981), Chap. 4.
[17] A. D. Yablon, M. F. Yan, D. J. DiGiovanni, S. L. Jones, D. N. Ridgway, G. S. Sandels, and I. A. White, "Novel Beam Expanders and High-Power Connectors," in Proceedings of the National Fiber Optic Engineers Conference (NFOEC), Sept. 7-11, 2003 Orlando, FL.

Sub Glass Transition Relaxation in Optical Fibers

J. W. Fleming

(908) 582-4499

OFS Laboratories, Murray Hill, NJ 07974
jwf@ofsoptics.com

Abstract

Investigations of the viscoelastic properties of silica-based optical fiber have revealed a fiber relaxation more than 700 ^{o}C below the glass transition temperature. The phenomenon is essentially dependent on the magnitude of the tension with which the fiber is drawn.

Introduction

We have assembled a novel apparatus called a fiber dilatometer that can be used to measure thermal expansion coefficient, viscosity and relaxation on fiber specimens. In this paper we report on the observed magnitude and temperature dependence of a unique fiber draw artifact, a sub glass transition relaxation. Fiber draw leaves it's signature on the glass being drawn. Typical glass quenching rates during optical fiber draw are in the range of 10^3 to 10^4 ^{o}C/sec.[1] This rapid cooling and the associated draw stress maintained during cooling are known to affect certain properties of other glass fiber such as textile fiber.[2,3,4] The rapid cooling can result in a tremendous increase in the temperature at which the liquid glass begins behaving as a solid, the fictive temperature, T_f. Draw tensions are typically greater than 80 gm. That translates into more than 9000 psi, enough to cause an elastic increase in a meter length of fiber > 1 mm.

In silica, draw stress has been connected with at least one specific draw induced defect.[5] Another observed effect is a change in the Δn between core and cladding as a function of draw tension.[6] It's not difficult to imagine such stresses at high temperature altering the glass structure.

Experimental procedure

The fiber dilatometer is shown schematically in figure 1. It is built on an optical bench providing vibration
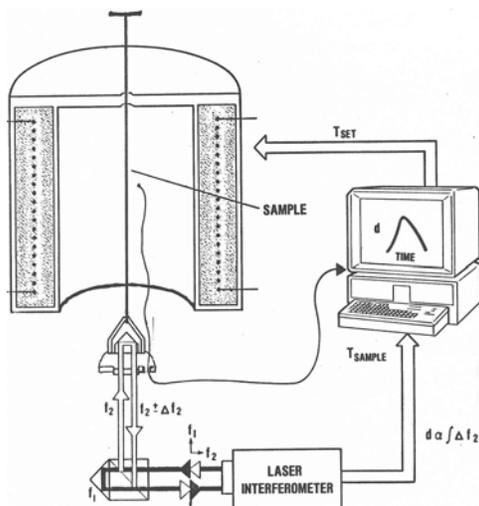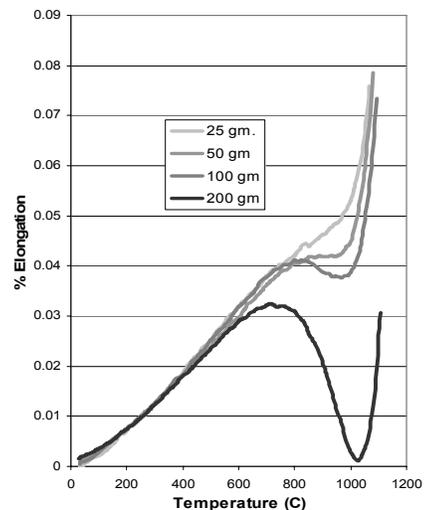

Figure 1. Schematic of the fiber dilatometer.

Figure 2. Elongation vs. Temperature Type 1 silica

isolation. A stand mounted on the bench supports a tube furnace above the bench with the axis of the tube oriented vertically. The purpose of the furnace is to heat a given length of fiber at a controlled rate such that the temperature distribution over the fiber length remains uniform at any time during an experiment. The top and bottom of the furnace are insulated to provide a very sharp temperature gradient at each end. Capillary

2

tubing having an id of 1 mm is placed through the center of the insulation for fiber access to the furnace.

The furnace used in this study is operable from room temperature to 1550 ^{o}C. Typically, the heating rate for our fiber measurements was 10 ^{o}C/min. The hot zone length and heated fiber length is 500 mm. Temperature was controlled to ±1 ^{o}C at six evenly spaced zones in the furnace using thermocouples a few millimeters from the fiber position. For fiber surface protection, the fibers were coated with epoxy acrylate during draw. Fibers are stripped of this coating in hot sulfuric acid and cleaned. They are then assembled in the apparatus being supported on a fixed mount above the furnace, threaded through the furnace, and to the end below the furnace, a corner cube assembly is clamped. Using micropositioners on the upper end, the fiber was oriented so that it hung unobstructed through the furnace.

The apparatus uses a laser Doppler interferometer to measure the vertical displacement of the corner cube. This instrument has a resolution of 10 nm. The corner cube assembly has a mass of 8.78 gm. Elongation and temperature data were recorded under computer control. Frequency of data acquisition was 3 to 10 times per minute.

Samples used in this investigation were single material fiber specimens of various commercially available silica. Table I lists these materials. We also measured commercially available fiber specimens from several manufacturers. When considering the relaxation effect in an optical fiber including core and cladding, one needs to account for the viscoelastic response of the core to temperature. Perhaps the temperature at which relaxation occurs is dependent on the T_g. The amount of low temperature relaxation observed is a function of temperature.

Table I.
Optical fiber materials investigated
Type 1. Natural quartz derived silica, >ppm metal impurities, 180 ppm OH
Type 2. Natural quartz derived silica, < ppm metal impurities, < 1ppm OH
Type 3. Wet synthetic silica from vapor deposition, 150 ppm OH
Type 4. Wet synthetic silica from vapor deposition, 1000 ppm OH from soot

Fibers were drawn from rods of the glass using a standard lightguide fiber drawing furnace such as that described in the introduction. Several draw speeds and draw tensions were used. Fiber diameter for all specimens was 125 ±1 μm. Specifically selected draw conditions were 1, 3, and 5 m/sec and 25, 50, 100, 150, 200 grams tension.

The resultant elongation vs. temperature data was analyzed using a computer program designed to extract characteristic features of the plot such as thermal expansion coefficient, temperature of the onset of relaxation, maximum relaxation, and T_g .

Results and discussion

Characteristic results of our measurements are shown in figure 2. As can be seen, at about 700 ^{o}C there is a relaxation or shrinking in the fiber that depends on draw tension.

This displacement is a complicated compound effect that is a function of thermal expansion below and above the glass transition, the delayed elastic relaxation, and viscous flow under load. In this study those factors are happening simultaneously with their response time being temperature dependent.

In addition to our standard test that involved continuous heating at a constant rate we made a number of isothermal measurements with the primary objective to observe the rate of relaxation as a function of temperature. In these experiments we were able to observe relaxation at as low as 400 ^{o}C as shown in figure 3. As mentioned in the introduction, changes in glass properties as a function of fiber drawing conditions have been observed for many years by researchers interested in the textile glass fiber and insulation fiber industries. The interesting aspect of this study is that the relaxation is observed at 400 ^{o}C. That it is hundreds of degrees below T_g of silica, 1175 ^{o}C. In figure 4 the relaxation of the four types of silica studied are
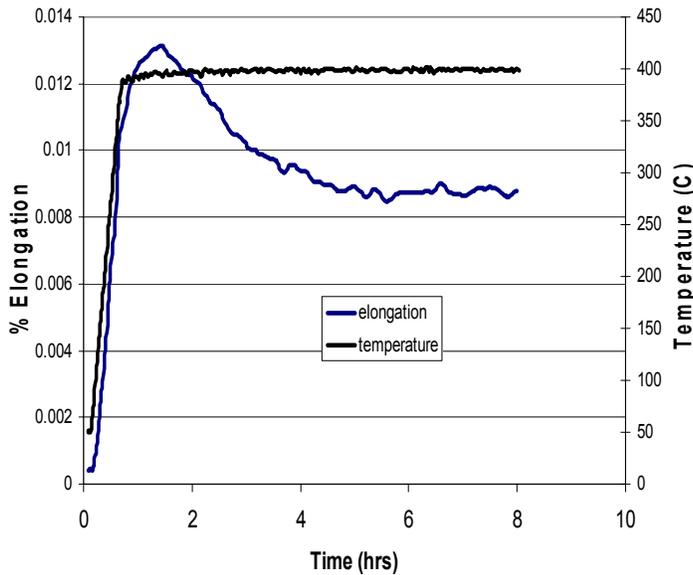
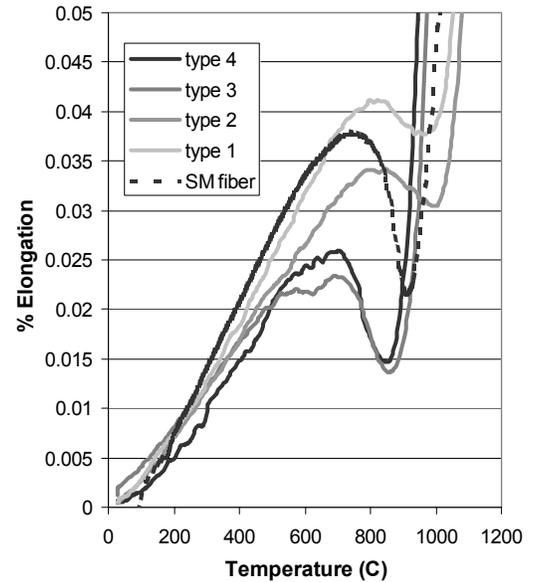Figure 3. Isothermal relaxation of synthetic silica fiber.

Figure 4. Relaxation in the 5 types of silica fiber.

shown. All were drawn with 100 gm tension. Also included is data for a commercially available single mode fiber drawn at 110 gm tension. It is clear that the relaxation is material as well as draw tension dependent. We have also examined hundreds of fiber specimens of various types of commercially available glass fiber. Today's high silica content optical fibers are drawn at temperatures in the range of 2000 to 2200°C. Tensions employed vary from a few to hundreds of gm. Draw speeds vary from 1 to 30 m/sec. We have observed the sub-T_g relaxation in all fibers studied with the magnitude of relaxation dependent on draw tension. Not surprisingly, relaxation and other thermophysical properties of the optical fiber are quite similar to those of the single material silica from which they are primarily comprised.

Conclusion

We have constructed an apparatus that can make very precise measurements of the thermophysical properties of optical fiber and optical fiber materials. A structural relaxation that occurs at unexpectedly low temperatures was observed. The relaxation is primarily dependent on draw stress and fiber material. Optical fiber and single material fiber show similar relaxation behavior.

References

[1] U. C. Paek and C. R. Kurkjian, "Calculation of Cooling Rate and Induced Stresses in Drawing of Optical Fibers," J. Am. Ceram. Soc. 58 [7-8] 330-335 (1975).

[2] J. F. Stirling, "Frozen Strains in Glass Fibers," J. Soc. Glass Technol., 39, 134-44T (1955).

[3] W. H. Otto, "Compaction Effects in Glass Fibers," J. Am. Ceram. Soc., 44 [2] 68-72 (1961).

[4] T. Takamori, "Effects of Thermomechanical History on Properties of Glasses," J. Am. Ceram. Soc., 46 [8], 366-370 (1963).

[5] Y. Hibino, H. Hanafusa and S. Sakaguchi, "Formation of Drawing-Induced E' Centers in Optical Fibers," Jap. J. of Appl. Phys., 24, [9] 1117-1121 (1985).

[6] A.D. Yablon, M.F. Yan, P. Wisk, F. V. DiMarcello, J. W. Fleming, W. A. Reed, E. M. Monberg, D. J. DiGiovanni, J. Jasapara and M. E. Lines, "Anamolous Refractive Index Changes in Optical Fibers Resulting From Frozen-in Viscoelastic Strain," in Proceedings of OFC 2003, Paper PD6-1 (2003).

Bending-induced thermal stress birefringence in single-mode fibers

Hagen Renner
Technische Universität Hamburg-Harburg, 21071 Hamburg, Germany
renner@tu-harburg.de

Abstract: The field deformation in bent fibers causes a non-symmetric field overlap with the thermal fiber stress profile and yields large modal stress birefringence. The latter can fully compensate the well-known bending-induced mechanical stress birefringence.

1. Introduction

In optical fiber transmission systems, fiber birefringence is undesired as it causes polarization-mode dispersion (PMD) as one of the most serious capacity limitations [1]. Special effort is required to overcome the PMD-induced system degradation on the electronic side [2] or directly on developing improved fiber technologies [1]. Bending-induced birefringence has been found to be one of the most important causes of the total fiber birefringence. Fibers without bending-induced birefringence are desirable in all situations where the fibers experience strong or variable bendings, such as in fiber gyroscopes [3] or in all device-connecting patchcords. Until now bending-induced birefringence has been attributed mainly to mechanical stresses exerted on the fiber during bending [4]. We show here that another mechanism contributes to the overall bending-induced birefringence to an amount that can be even much larger than the well-known mechanical stress birefringence. The bending-induced off-axis shift and deformation of the fundamental-mode field lead to a non-symmetric overlap of the mode intensity with the intrinsic thermal stress profile of the fiber and thus causes significant bending-induced thermal stress birefringence. In fluorine-doped fibers it can be much larger than the bending-induced mechanical stress birefringence.

2. Bending-induced thermal stress birefringence

It is well known that bending a single-mode fiber causes significant modal birefringence. The birefringence B is the difference of the effective indices of the two orthogonally polarized fundamental modes. The major contribution in bent fibers as identified up to now is the bending-induced mechanical stress birefringence B_M caused by the elastic deformation of the fiber and has been given by [4]

$$B_M = E(C_1 - C_2)b^2/(2R_B^2) \simeq -0.137\, b^2/R_B^2, \tag{1}$$

where $2b$ is the outer fiber diameter, R_B the bending radius of the fiber axis, E is Young's modulus and C_1 and C_2 are stress-optic coefficients. The approximation on the right-hand side is obtained from the experimental data for vitreous silica, $C_1 = 0.65 \times 10^{-5}$ mm^2/kg, $C_2 = 4.22 \times 10^{-5}$ mm^2/kg and $E = 7.7 \times 10^3$ kg/mm^2 at $\lambda = 546$ nm [5]. Bending-induced form birefringence has been reported to be smaller than the mechanical stress birefringence of Eq. (1) by about three orders of magnitude [6] and is not considered here.

In this paper we show that bending-induced birefringence can be caused to a large or even the major amount by a quite different mechanism as follows: In doped optical fibers axial stresses are caused by the different expansion coefficients of the dopants creating the refractive-index profile [7, 8, 9]. Since fibers are drawn at high temperatures, there are significant longitudinal stresses at room temperature. It follows from common elasto-optical theory [7, 8], that these stresses also cause a local birefringence for light propagating parallel to the fiber axis at each transversal position of the fiber cross section.

In the cross-sectional plane of a circular fiber, the local birefringence at a certain radial distance changes sign along the azimuthal coordinate every $90°$. Since in the straight fiber the fundamental-mode intensity is also circularly symmetric and concentric to the fiber axis, the azimuthally varying birefringence is 'seen' by the mode to equal parts and is thus averaged out and no modal birefringence results.

However, if the field is shifted off-axis or is elliptically deformed by bending the fiber [10] the local birefringence contributions are no longer cancelled out. Thus, bending a fiber must cause additional stress birefringence by the modified overlap of the mode intensity with the transverse thermal stress profile.
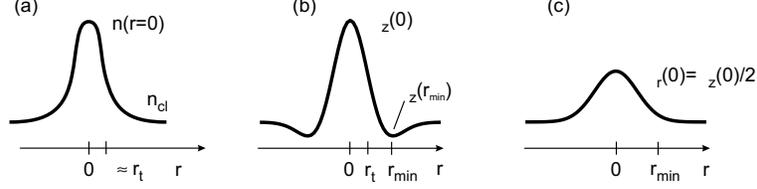
Figure 1. Schematic illustration of a) the refractive-index profile $n(r)$ versus the radial coordinate r in the fiber with core radius ρ, b) the profile of the longitudinal stress component $\sigma_z(r)$, c) the profile of the radial stress component $\sigma_r(r)$.

In order to quantify the bending-induced thermal stress birefringence, we first approximate the profile of the axial stress in a fiber by

$$\sigma_z(r) = A_1 \left(1 - r^2/\eta^2\right) \exp\left(-r^2/\eta^2\right) + A_2. \tag{2}$$

and fit the maximum at the fiber axis $\sigma_z(0)$ and the minimum $\sigma_z(r_{\min})$ (Fig. 1) to experimentally obtained axial stress profiles [8]. The resulting local birefringence can be calculated from σ_z as [7, 8]

$$\delta n(r, \phi) = \frac{1}{2} C \left[2\sigma_r(r) - \sigma_z(r)\right] \cos(2\phi), \qquad \sigma_r(r) = \frac{1}{r^2} \int_0^r \sigma_z(r') \, r' \, \mathrm{d}r', \tag{3}$$

where (r, ϕ) are cylindrical coordinates and $\sigma_r(0) = \sigma_z(0)/2$.

Second, the scalar fundamental-mode field is calculated by a variational method in cylindrical coordinates adapted to the geometry of the fiber bending [11] using a Gaussian field ansatz

$$\Psi(x, y) = \Psi_0 \exp\left\{-\frac{1}{2}\left[\frac{(x-s)^2}{w_x^2} + \frac{y^2}{w_y^2}\right]\right\}, \tag{4}$$

where $x = r \cos \phi$ and $y = r \sin \phi$ are cartesian coordinates with the origin in the fiber axis. The off-axis field shift s and the two mode-field widths w_x and w_y obtained this way depend on the bending radius R_B of the fiber axis.

Finally, the overlap integral (in cylindrical geometry) of the deformed mode-field intensity with the thermal stress-birefringence profile $\delta n(r, \phi)$ gives the bending-induced thermal stress birefringence B_T of the fundamental mode [11],

$$B_T \simeq \frac{2 \iint (1 + x/R_B) \, \delta n \, \Psi^2 \, \mathrm{d}x\mathrm{d}y}{\iint [1 - (x/R_B) + (x/R_B)^2] \, \Psi^2 \, \mathrm{d}x\mathrm{d}y}. \tag{5}$$

3. Results

A particularly strong bending-induced thermal stress birefringence is found for pure-silica core fibers with a fluorine-doped cladding. Such fibers have low losses and the fluorine-doping is for decreasing the index of the cladding [12, 13]. However, to our knowledge, no experimental results for the bending-induced birefringence are available for this type of fiber. It was observed for fluorine-doped fibers [8, 9] that the isotropic index of a fiber with nominal index difference $\Delta n(F = 0) = 6.6 \times 10^{-3}$ reduces with increasing fiber-drawing force F as $\Delta n(F) = \Delta n(0) - 4.8 \times 10^{-3} \times (F/\text{N})$, while the axial stress difference increases as $\Delta\sigma_z = 72 \text{ kg/mm}^2 \times (F/\text{N})$. In order to investigate the bending-induced thermal stress birefringence in such fibers, we thus assume the relation $\Delta\sigma_z = 1.5 \times 10^4 \text{kg} / \text{mm}^2 \times [\Delta n(0) - \Delta n(F)]$ between index difference and axial stress difference. In Fig. 2 the bending-induced thermal stress birefringence B_T multiplied by R_B^2 is shown for $R_B = 50$ mm (solid lines) and $R_B = 20$ mm (dotted lines) in order to illustrate the approximate proportionality to $1/R_B^2$ for large bending radii. Labelling parameter is the core/cladding index difference Δn, and the wavelength is $\lambda = 1550$ nm. The horizontal dash-dotted line gives -1 times the bending-induced mechanical stress birefringence B_M from Eq. (1). It is interesting that for $\Delta n \leq 0.0052$, the bending-induced thermal stress birefringence B_T is larger than the bending-induced mechanical stress birefringence B_M. For $\Delta n \leq 0.003$, the ratio B_T/B_M is even larger than 10. Fig. 2 (b) shows the bending losses for the investigated fibers calculated according to Ref. [15] for $R_B = 20$ mm. Obviously, it should be possible to realize pure-silica core fibers with flourine-doped cladding with low bending losses, in which the bending-induced thermal and mechanical stress birefringences cancel each other independently of the fiber bending radius. In Fig. 2 (a), a fiber with $\Delta n = 0.0052$ and a single-mode value of the normalized frequency $V = 2\pi\rho(2n\Delta n)^{1/2}/\lambda$ of 2.4 requires an easily realizable core radius of $\rho = 3.1\mu$m to let the thermal and the mechanical bending-induced stress birefringence cancel each other.
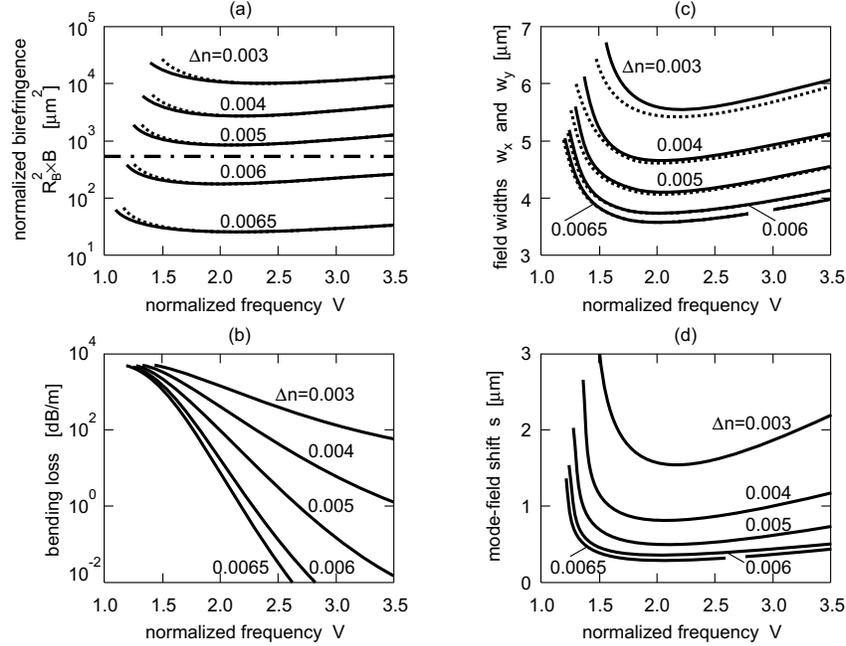
Figure 2. (a) Bending-induced thermal stress birefringence of pure-silica core fibers with fluorine-doped cladding calculated for $R_B = 20$ mm (dotted lines) and $R_B = 50$ mm (solid lines). The dash-dotted line shows the bending-induced mechanical stress birefringence according to Eq. (1) for an outer fiber diameter $2b = 125\mu$m. (b) Bending loss for $R_B = 20$ mm. (c) Field widths w_x (solid line) and w_y (dotted line) for $R_B = 20$ mm. (d) Off-axis field shift s for $R_B = 20$ mm.

In the right side of Fig. 2, the corresponding field widths w_x and w_y (Fig. 2 c) and the off-axis field shift s (Fig. 2 d) are shown for $R_B = 20$ mm. As can be seen $w_x \simeq w_y$, and the bend-induced thermal stress birefringence is mainly caused by the asymmetric overlap of the thermal stress profile with the mode-field intensity off-axis shifted by s.

For GeO$_2$-doped fibers, we deduce $\Delta\sigma_z \simeq \Delta n \times 500$ kg/mm^2 from the data given in [14]. For these fibers, B_T was found to be comparable in magnitude to B_M only for very small core index differences $\Delta n = 2 \times 10^{-3}$, for which the bending losses are already above 10^2 dB/m at $R_B = 50$ mm for all core radii which ensure single-mode operation. For larger index differences, B_T/B_M decreases and goes down to 10^{-1} for $\Delta n = 6 \times 10^{-3}$, and to 10^{-2} for $\Delta n = 2.4 \times 10^{-2}$. This may be the reason why the bending-induced thermal stress birefringence has not been identified experimentally until to now.

4. Conclusions

We have shown theoretically that in addition to the well-known bending-induced mechanical stress birefringence, a strong bending-induced thermal stress birefringence can occur in fibers due to the asymmetric overlap of the mode-field intensity with the thermal stress profile of the fiber. Both effects can be used to cancel each other and obtain zero bending-induced fiber birefringence.

References

1. K. Walker, Proc. OFC 2003, Atlanta, Georgia, USA, paper WJ4, pp. 369-370 (2003)
2. C. Xie, L. Moller, H. Haunstein, S. Hunsche, Proc. OFC 2003, Atlanta, Georgia, USA, paper TuO1, pp. 258-259 (2003)
3. R. Usui and A. Ohno, 15th Optical Fiber Sensors Conference, Technical Digest. OFS 2002, vol.1, (2002) pp.11-14.
4. R. Ulrich, S. C. Rashleigh, and W. Eickhoff, Opt. Lett. **5**, (1980) 273-275.
5. W. Primak and D. Post, J. Appl. Phys. **30**, 779-788 (1959).
6. S. J. Garth, J. Lightwave Technol. **6** (1988) 445-449.
7. G. W. Scherer, Appl. Opt. **19**, 2000-2006 (1980).
8. W. Hermann, M. Hutjiens, and D. U. Wiechert, Appl. Opt. **28**, pp. 1980-1983 (1989).
9. Y. Hibino, F. Hanawa, and M. Horiguchi, J. Appl. Phys. **65** (1989) 30-34.
10. D. Marcuse, J. Opt. Soc. Am. **66** (1976) 311-320.
11. H. Renner, to be published.
12. M. Oto, S. Kikugawa, N. Sarukura, M. Hirano, and H. Hosono, IEEE Photon. Technol. Lett. **13** (2001) 978-80.
13. S. Unger, J. Kirchhof, S. Schroter, A. Schwuchow, H. Frost, Proc. SPIE-Int. Soc. Opt. Eng, vol.**4616** (2002) 161-72.
14. P. K. Bachmann, W. Hermann, H. Wehr, and D. U. Wiechert, Appl. Opt. **26**, pp. 1175-1182 (1987).
15. J. Sakai and T. Kimura, Appl. Opt. **22** (1978) 1499-1506.

Destruction of silica fiber cladding by fiber fuse effect.

E.M.Dianov, I.A.Bufetov and A.A.Frolov
Fiber Optics Research Center at the A. M. Prokhorov General Physics Institute of the Russian Academy of Sciences,
38 Vavilov Street, 119991, Moscow, Russia
tel: 7 (095) 135-0566, fax: 7 (095) 135-8139, E-mail: dianov@fo.gpi.ru

Abstract: The phenomenon of silica fiber cladding destruction by the fiber fuse effect has been observed for the first time. The cladding destruction leads to the termination of the optical discharge propagation in a fiber.
©2003 Optical Society of America
OCIS codes: (060.2400) Fiber properties; (140.3330) Laser damage; (140.3440) Laser induced breakdown.

1. Introduction

The fiber fuse effect under a modest power of the laser radiation is characterized by the formation and propagation of the optical discharge dense plasma along the fiber core with the speed of ~ 1 m/s. The estimated values of the plasma pressure and the temperature are ~ 10^4 atm and ~ 10^4 K [1–5].

In case of standard silica-based fibers with the cladding diameter of 125 μm this phenomenon results in a catastrophic damage of the fiber core manifested itself as a set of bubbles in the core [1, 2] and change of the refractive index profile [6]. The silica cladding of fibers is strong enough to withstand the action of the propagating plasma. The reduction of the fiber cladding strength by any way can lead to the deformation or even the destruction of the cladding under the high temperature and pressure of propagating plasma. This can result in changing parameters of the optical discharge propagation.

2. Experimental results

In our experiments the reduction of the cladding strength was achieved by decreasing its thickness. A stripped section of a fiber ~ 2 mm long was etched in hydrofluoric acid to get a number of waist-formed samples of fibers with the minimal cladding diameter *d* in the range of (10 ÷ 60) μm (Fig. 1, **a**). We studied single-mode fibers of different types, but most experiments were carried out using SMF28.
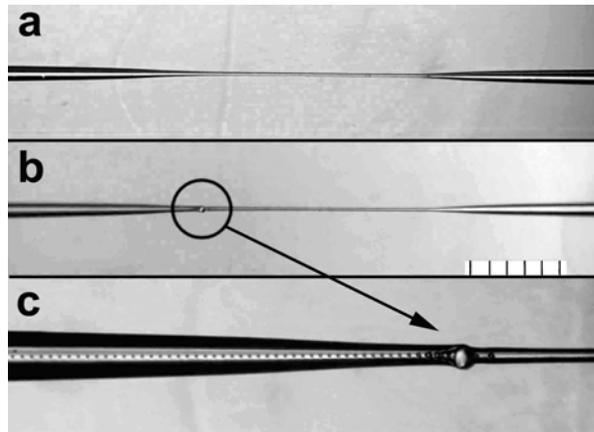

Fig. 1. Waist-formed length of SMF28 (Table 1, #1). **a** – before the optical discharge propagation, **b** and **c** – after the optical discharge propagation. One division of the scale corresponds to 0.1 mm fort **a** and **b**; **c** – the width of the frame corresponds to 1 mm. The laser radiation propagated from the right to the left.

The light source was an Yb-doped fiber laser operating at the wavelength of 1.06 μm or a Raman fiber laser operating at 1.24 μm. The fiber under investigation was spliced with output fibers of the lasers. The launched radiation powers *P* were between 1.3 and 3 W. The optical discharge was initiated by contacting the end of the fiber with a light absorbing surface.

The fibers listed in Table 1 were all tested to determine the mode field diameter (**MFD**) at the wavelength of laser radiation and the minimal power P_{th} required for the optical discharge propagation along the fiber with an silica cladding diameter of 125 μm.

Table 1. Parameters of fibers investigated.

Fiber#	**MFD**, μm	P_{th}, W	**d**, μm	**P**, W	d_c, μm	Fuse stopped
1	9.5	1.1	10.5	2.0	33	yes
2	9.5	1.1	15.5	1.6	30	yes
3	9.5	1.1	17	1.3	28.5	yes
4	9.5	1.1	18	2.9	32.	yes
5	9.5	1.1	25	3.0	33	yes
6	9.5	1.1	33	2.9	33	yes
7	9.5	1.1	38	3.0	–	no
8	5.8	0.57	15	1.5	23	yes
9	11.1	1.4	42	2.0	–	no
10	11.1	1.4	50	2.0	–	no
11	11.1	1.4	60	2.0	–	no

We have fulfilled a number of experiments to investigate the features of plasma propagation through the etched sections with various waist diameters. If the diameter of the etched section of the fiber was large enough, that is much more then some critical value d_c ($d > d_c$), the discharge propagation was practically the same as in a standard fiber (Table 1, #10 and 11). When the diameter of the waist of the etched section was only slightly larger than d_c the character of the fiber damage was changed dramatically (Fig. 2). If in a nonetched section of the fiber the damage represented a periodic set of bubbles (Fig. 2, **3**), the damage of the etched section took the form of a long capillary (Fig. 2, **2**). After passing the etched section the optical discharge formed a periodic structure of the damage again (Fig. 2, **1**).

When $d < d_c$ the optical discharge couldn't pass through the etched section of the fiber (Fig. 1, **b**,**c**). The high temperature and pressure of the plasma caused the formation of a large bubble at the cross-section of the fiber with the cladding diameter equal to d_c . The spreading of the absorbing plasma results in the decrease of the laser radiation absorption. . This breaks the necessary condition of the discharge propagation and so it terminates. Sometimes we observed the complete destruction of the fiber at the point where the fuse stopped (Fig. 3). Note that the observed increase in the threshold of fuse damage in microstructured fibers [7] is also connected with the density reduction of the optical discharge plasma because of its spreading.

The value of d_c may be estimated as follows. Assume that the fiber destruction is caused mainly by the pressure of the optical discharge occupying a cylinder with the diameter equal to **MFD** . Then the minimum diameter d_c of the etched section of the fiber, required to balance plasma pressure, can be estimated as $d_c = \textbf{MFD} \cdot (1 + \frac{p}{\sigma})$, where σ is the breaking strength of silica glass and **p** is the plasma pressure. Taking $\sigma \sim 10^9$ Pa and $p \sim 10^4$ atm $\approx 10^9$ Pa we obtain the reasonable estimation $d_c \approx 2 \cdot \textbf{MFD}$ (see Table 1).

One can see from Table 1 that the value of d_c doesn't practically depend on the power of the laser radiation for the particular fiber. This makes it possible to use the observed phenomenon of the optical discharge termination to protect optical fiber systems from the catastrophic damage when an accidental optical discharge occurs. One needs just to put into a fiber line a small waist-formed length of a fiber with the minimal cladding diameter slightly less then d_c , which will not allow any further propagation of the fuse.

The fact that the value of d_c doesn't increase with the laser radiation power (Table 1) means that such protective device will also effectively operate at higher laser powers unlike the device [8], which is based on a local increase of **MFD** in a fiber.
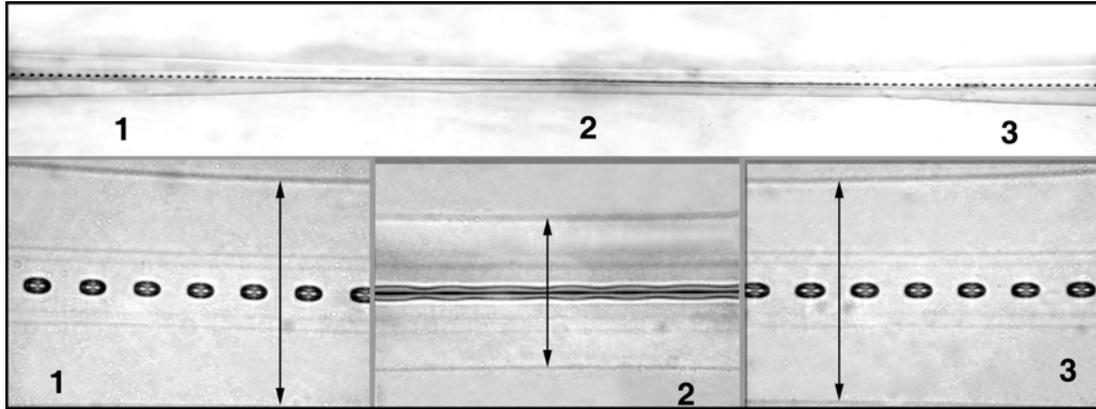
Fig. 2. Waist-formed section of the fiber after the optical discharge propagation without stopping, Table 1, #9. At the top of the figure is the general view of the fiber section, at the bottom regions **1**,**2** and **3** are shown at an enlarged scale. The laser radiation propagated from the left to the right. Scale: **1**–the length of the arrow 64.5 μm; **2**–the length of the arrow is 42 μm; **3** – 63 μm.
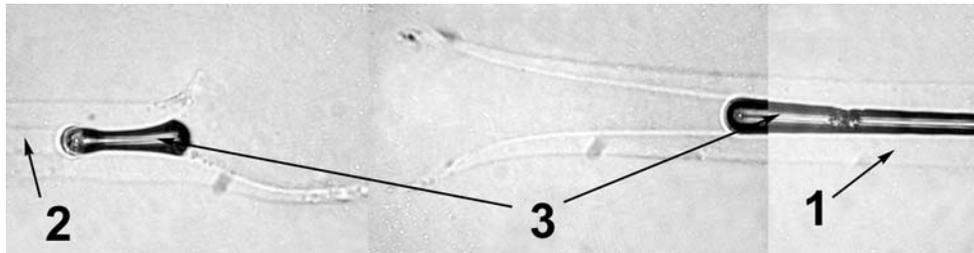

Fig. 3. The etched fiber section disintegrated after the optical discharge stopping. The picture was taken using immersion. Table 1, #8. 1 - silica cladding; 2 – undisturbed fiber core; 3 — bubbles or voids formed in the core after optical discharge passing. The bubble at the left corresponds to the discharge stopping point. The width of the frame is 250 μm. The laser radiation propagated from the left to the right.

Conclusion. It has been shown, that the diameter of a fiber silica cladding can substantially influence the process of the optical discharge propagation in a fiber. The observed phenomenon of the silica fiber cladding destruction by fiber fuse effect is a direct confirmation of the high pressure plasma formation in the fiber core, which is necessary for the discharge propagation. This phenomenon allows one to use a section of a fiber with reduced cladding strength as a protective device against the propagation of optical discharge in a fiber. Plasma spreading, occurring under cladding destruction results in the optical discharge termination.

7. References

1 R.Kashyap, K.J. Blow. "Observation of catastrophic self-propelled self-focusing in optical fibers." Electron. Lett., **24**, .47-49 (1988).

2 D.P. Hand, P.St.J. Russell. Solitary thermal shock waves and optical damage in optical fibers: the fiber fuse. Optics Letters, Vol.13, No.9, pp. 767-769 (1988).

3 Davis D.D., S.C. Mettler. "A comparative evaluation of fiber fuse models." Proc. SPIE vol. 2966, pp.592-606 (1997).

4 Yu.P. Raizer, "Laser-Induced Discharge Phenomena" (Plenum Publishing, New York, 1977), pp.189-263.

5 Dianov E. M., I.A.Bufetov, V.G.Plotnichenko, A.A.Frolov, V.M.Mashinsky, M.F.Churbanov, G.E.Snopatin. "Catastrophic destruction of optical fibres of various composition caused by laser radiation." Quantum. Electronics, **32**, 476-478 (2002).

6 E.M.Dianov, V.M.Mashinsky, V.A.Myzina, Y.S.Sidorin, A.M.Streltsov, A.V.Chickolini. "Change of refractive index profile in the process of laser-induced fibre damage." Sov. Lightwave Commun. **2** , 293-299 (1992).

7 E.Dianov , A. Frolov, I. Bufetov, Y. Chamorovsky, G. Ivanov, I.Vorobjev. "Fiber fuse effect in microstructured fibers." In OFC-2003 Technical Digest Vol.2 pp. 868-869, FH2 (2003).

8 D.P.Hand, T.A. Birks. "Single-mode tapers as fiber fuse damage circuit-breakers." Electron. Lett., **25**,. 33-34 (1989).

Towards the low limits of 1383 nm loss in PCVD enabled single mode fibre production

P.Matthijsse; D.R.Simons;
Draka Comteq, PO Box 1442, 5602BK, Eindhoven, the Netherlands,
Email: p.matthijsse.@drakafibre.com
Zhang Shuqiang; Luo Jie;
Yangtze Optical Fibre and Cable Co.Ltd, China;
J.Vydra; H.Fabian.
Heraeus Tenevo AG, Germany;

Abstract: Based on a pilot development series it is shown that careful prevention of OH⁻ contamination in all PCVD process steps enables industrial production of SM fibres with a 1383 nm loss reaching below 0.30 dB/km.

1. Introduction

Optimal usage of the enormous intrinsic transmission capacity of single mode fibre asks for a significant reduction of the OH⁻ excess loss (the so-called water-peak). This enables future use of DWDM systems in the E-band and also supports full exploitation of CWDM systems. In various papers [1], it has been shown that the technology to produce low or even zero water-peak SM fibres (LWP) on a large scale is available for some time already. As a result of this, standards like ITU-T: G.652.C and IEC: B1.3 have been approved and such fibres have been offered, including those being manufactured by PCVD core production technology. In this paper we will show for the first time that applying the PCVD based process allows for excess OH⁻ loss levels far below the levels required for practical use and approaching the theoretical limits of state-of-the-art fibres. The presented results are based on a joint R&D effort of the companies listed above.

2. Excess loss caused by hydroxyl contamination and its sources

The main objective of the LWP SM fibre is opening up the 1360 - 1460 nm E-band. Applying the Walker fibre loss model [2], it can easily be derived that for an OH⁻ excess below 0.02 dB/km, the maximum attenuation in the E-band is predominantly determined by intrinsic Rayleigh scattering loss at the 1360 nm edge and is at a level below 0.285 dB/km. Therefore our main goal is to achieve an excess OH⁻ loss ≤ 0.02 dB/km as a tolerable level in LWP SM fibre. As a restrictive second goal the cost-effectiveness of our current 500 km preform standard production process should not be affected.
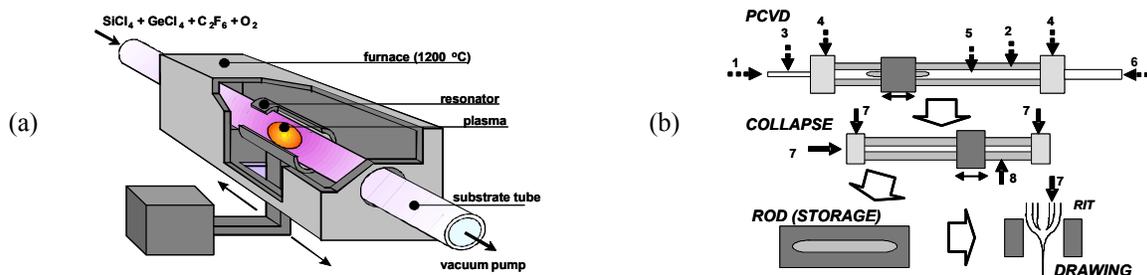

Fig. 1 Setup of a PCVD core production machine (a) and total process flow (b) with arrows showing potential sources of contamination

In the PCVD-based core rod production process (Fig. 1a) the gaseous reactants are directly vitrified into dense glass layers on the inside of a fused silica substrate tube, hence making this process step extremely sensitive to the incorporation of hydroxyl groups. Any subsequent purification of the deposited layers, e.g. drying by chlorine, is hardly effective. In Fig. 1b the various sources for OH⁻ contamination in the complete production cycle are indicated. A distinction can be made between a) basic material, i.e. chlorides, oxygen and the fused silica substrate tube (1, 2), b) non-ideal machine components like gas supply seals and connections (3), low pressure feed throughs (4) and c) process-cycle related surface contamination originating from tube mounting (5,6), collapsing (7,8), core rod storage

and rod-in-tube (RIT) mounting. Note that all contaminations in the PCVD process are directly incorporated in the core area. Surface contamination is important at three critical interfaces: i) the core rod centre-line that is exposed during the collapsing process, ii) the interface between deposited PCVD material and substrate tube and iii) the interface between core rod and jacket tube.

The contribution of the hydroxyl in the jacket tube and in the coating process may be neglected due to the large distance to the fibre core.

3. Reducing the hydroxyl contaminations

In view of the fact that later purification of plasma deposited material will be extremely difficult, the most straightforward solution is: *Prevention!* For the basic materials, gases and tubes, this involved intensive discussions with our supply partners resulting in the required quality of starting materials. In this discussion also the quality of auxiliary quartz in e.g. tube handles was taken into account. However, it is not sufficient to consider material quality alone. To get the pure materials uncontaminated into the process equipment asked for many improvements. Important examples are the chloride vessel (re)filling procedures, leak-tightness check procedures of the gas supply system, as well as proper and careful tube cleaning and handling. Redesign of machine parts sensitive to surface contamination during tube (de)mounting resulted in a decrease of surface area and "dead volumes". A very challenging task was the further optimization of the PCVD feed through construction to reach the required high leak-tightness of the PCVD low vacuum system. As for the *collapsing heat sources*, it appeared that the use of both electrical furnace and hydrogen-oxygen burners leads to similar results. Apparently, the formation of OH⁻ groups due to the flame of an H_2-O_2 burner can be reduced by a surface treatment (see below).

Quite another approach is to reduce the hydroxyl content in the environment surrounding delicate machine parts. In Fig 2 an example is given of the positive effect of reducing the relative humidity in the immediate vicinity of the feed throughs showing the extreme conditions for the low pressure process.
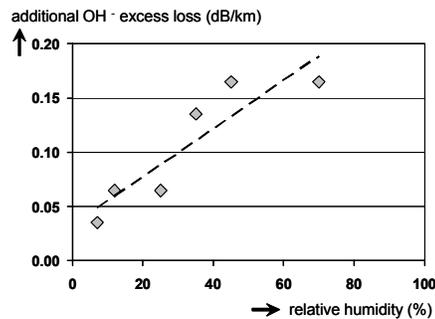
Fig. 2 Effect of reduction of relative humidity on OH⁻ excess loss compared with an arbitrary reference level.

4. Reducing the effect of residual hydroxyl contaminations

Although prevention can lead to a very low OH⁻ contamination, a small residue will always remain. The effect of this residue can be reduced by various means. The positive effect of *fluorine doping* has been recognized from its inception [3]. Optimization of the doping level showed a further excess loss reduction. Additional purification of the fluorine source itself appeared very essential.

Every open air exposure of a fused silica surface immediately leads to adsorption of a thin layer of water, which can lead to further in-diffusion during subsequent hot processes. A *surface etching treatment* is essential and effective in removing these surface contaminations. In the PCVD process this is done by O_2/C_2F_6 plasma etching. In the collapse stage C_2F_6 etching is applied to remove the centre-line contamination while after collapsing, a room temperature HF wet-chemical etch removes any possible surface contamination of the preform.

Careful modeling of the OH⁻ diffusion during core rod collapsing and fibre drawing revealed that the diffusion effect is very much dependent upon the precise chemical reactions underlying the OH⁻ transport. In the glass matrix both stable and meta-stable hydroxyl groups can be distinguished [4]. The stable OH⁻ species diffuse only very slowly due to the covalent bond to the silica glass matrix. This is the case in state-of-the-art synthetic fused silica produced by soot deposition (like the substrate tube) as it is free of molecular hydrogen and water. Hydroxyl groups incorporated in the glass surface during hot processes tend to have a meta-stable character. The rapid diffusion of this type of hydroxyl might be dominated by diffusion of either molecular hydrogen and/or molecular H_2O [5, 6].

Diffusion of residual OH⁻ groups into the core region during collapsing and fibre drawing is also determined by the *distance* from the substrate and from the surface of the preform to the core area. In the standard SM fibre

production process these interfaces are major factors in process productivity [7], and hence the fibre cost price. Increasing these distances could be prevented up to now by surface etching. Another development will be a high quality substrate tube with a significantly reduced hydroxyl content of the bulk glass (less than 100 ppb).

5. The result of the combined measures

Even though the total effect will be less than the sum of the individual effects, the combination of all the measures mentioned above, yield a layered defense against hydroxyl based on redundancy. The total effect is also determined by statistical factors during process execution. Careful process control, improved operational procedures and feedback based on fibre results usually shows a learning curve effect leading to the ultimate yield of the required product characteristics after some time. For this reason it was very encouraging that even in the first pilot run on a line fully equipped with the combination of all measures the first <0.30 dB/km fibre was produced already (Fig. 3c). For reference, the set target (a) and a loss limit as standardized by ITU-T and IEC (b) are also indicated in figure 3
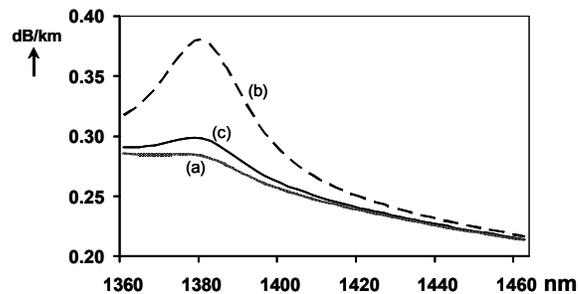

Fig. 3 E-band loss curves: (a) target with 0.285 dB/km loss at 1383nm, (b): example of G.652-c limit loss of 0.38 dB/km at 1383 nm for a fibre specified as 0.38 dB/km @ 1310 nm and (c) current best result from pilot PCVD series

At low levels of the OH^- excess loss, *aging* due to the reaction of free hydrogen with defects in the core silica structure may become significant [8]. Again, countermeasures are in curing (e.g. deuterium fibre treatment [9]) and in prevention by careful choice of material composition and heat-treatment during drawing. Applying this latter method resulted in negligible aging effects without affecting the operational PCVD and drawing processes significantly.

As none of the above measures is restrictive with respect to *scalability* we will apply the developed improvements also in the next generation 2000 km preforms. With PCVD core rod technology and very large synthetic fused silica cylinders (RIC: Rod-In-Cylinder technology) we are able to produce preforms with a diameter of 150 mm and larger, yielding high quality fibres. Applying the developed improvements to these concepts allows for even more cost-effective LWP fiber production.

6. Conclusions

Careful and precise quantification of all the hydroxyl contamination sources combined with skillful engineering and supply of high purity raw materials revealed that the production of enhanced LWP fibre with the PCVD based SM fibre production process is feasible. A sub-ppb residual OH^- concentration in the fibre core region has been achieved corresponding with a total loss level below 0.30 dB/km, i.e. far beyond the limits as set in the international standards for LWP fibres. As none of the measures is restrictive with respect to product type and process scale the result is sustainable for future process steps. These may be in applying the developed improvements also in other fibre types where applications in the E-band are relevant and in further scaling-up steps.

7. References

[1] S.K.Das et al, "Coarse-WDM throughput of up to 20 Gb/s in the 1330-1440 nm region over 63 km of low water peak fibre", Proc. NFOEC, pp 850-855, (2001)
[2] S.S.Walker, "Rapid modeling and estimation of total spectral loss in optical fibers", J. of Lightw. Techn., Vol LT-4, pp 1125-1131, (1986)
[3] P.Bachmann et al, "Low OH excess loss PCVD fibres prepared by fluorine doping", Electronics Letters, vol. 20, no 1, pp 35 -36 (1984)
[4] R.W. Lee, "On the role of hydroxyl in the diffusion of hydrogen in fused silica", Phys. and Chem. of Glass, Vol. 5, No. 2, pp 35–42, (1964)
[5] J. E. Shelby, "Protonic species in vitreous silica", J. of Non-Crystalline Solids, 179, pp 138 – 147, (1994)
[6] R. H. Doremus, "Diffusion of water in silica glass", J. Mater. Res., Vol. 10, No. 9, pp 2379 – 2389, (1995)
[7] A.H.van Bergen et al, "Large, all synthetic, PCVD preform manufacturing, Proc. EFOC, pp 220-224, (1992)
[8] K.H.Chang et al, "New hydrogen aging loss mechanism in the 1400 nm window", Proc. OFC; paper PD 22-1; (1999)
[9] J.Stone, "Interactions of hydrogen and deuterium with silica optical fibers: a review", J. of Lightw. Techn., Vol LT-5, pp 712-733, (1987)

Positive-Medial Dispersion Fiber of Ring-core profile with attenuation as low as 0.210dB/km and Aeff about 125μm²

Katsunori Imamura,   Kazunori Mukasa,   and   Takeshi Yagi

Fitel Photonics Laboratory, R&D Division, FURUKAWA Electric Co., Ltd.
6, Yawata-Kaigandori, Ichihara, Chiba 290-8555 Japan
E-mail address: imamura.katsunori@furukawa.co.jp

Abstract: Attenuation of Positive-Medial Dispersion Fiber using a ring-core profile has been successfully decreased from 0.240dB/km to 0.210dB/km keeping large Aeff as 125μm². Attenuation of P-MDF using a conventional profile was also decreased as low as 0.180dB/km.

1. Introduction

Recently, dispersion management transmission line as SMF plus RDF has been paid a considerable attention for the long-haul WDM transmission [1-2]. But, to realize long-haul 40Gb/s transmission, the suppression of a maximum accumulated dispersion in a span will be required addition to the conventional requirements. To respond these requirements, we have already reported the dispersion management transmission line consisted of P-MDF plus and N-MDF [3]. Typical characteristics of MDF are shown in Table 1.

Table 1. The typical characteristics of MDF (1550nm)

Fiber	Attenuation	Dispersion	Slope	DPS	Aeff	PMD	Bend Loss
	dB/km	ps/nm/km	ps/nm²/km	nm	μm²	ps/rkm	dB/m
P-MDF	0.190	14.5	0.070	207	95	0.04	5
N-MDF	0.220	-14.5	-0.040	290	32	0.05	5

As shown in Table, MDF has successfully suppressed local dispersion to 14.5ps/nm/km, and the maximum accumulated dispersion in a span would be successfully suppressed. But Aeff of P-MDF, about 95μm², might not be enough considering future's high-capacity transmission. So, P-MDF with Enlarged Aeff (P-MDF[EA]) was already developed and reported. By introducing a ring-core profile (Fig.1-2), Aeff was enlarged more than 100μm² keeping low dispersion about 11ps/nm/km [4]. Typical characteristics of P-MDF[EA] are shown in Table 2.
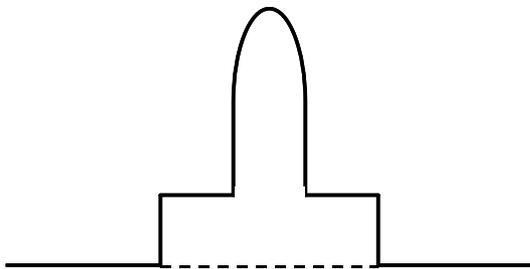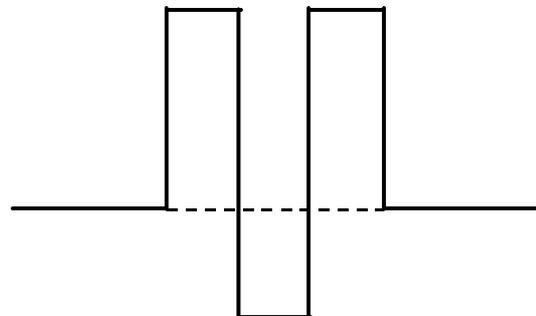

Fig. 1-1. Profile of Conventional P-MDF

Fig. 1-2. Ring core profile

Table 2. The typical characteristics of P-MDF^{EA} (1550nm)

Fiber	Attenuation	Dispersion	Slope	DPS	Aeff	PMD	Bend Loss
	dB/km	ps/nm/km	ps/nm^2/km	nm	μm^2	ps/rkm	dB/m
P-MDF^{EA}	0.240	11.0	0.070	157	110	0.04	10

As shown in table, P-MDF^{EA} has drastically enlarged Aeff compared with conventional P-MDF, keeping suppressed dispersion. But, attenuation of P-MDF^{EA} has increased as 0.240dB/km because of slightly special profile as ring-core profile, and it has been a big obstacle for practical use. Addition to that, further attenuation reduction of conventional P-MDF from 0.190dB/km is fascinating as the future transmission technology. This time, we set the target of dispersion at 13ps/nm/km considering easiness of dispersion compensation, and investigated about attenuation reduction of P-MDF from two points of view, attenuation reduction of ring core profile and ultimate attenuation reduction of conventional P-MDF by use of F-doped clad, so the results will be reported.

2. Attenuation reduction of P-MDF with ring-core profile

As reported in the reference [4], fibers which have depressed layer in center core as ring-core profile are attractive from such a point of view as consistent with suppressing dispersion and enlarging Aeff, but these fibers tend to have high attenuation. We thought there is a strong correlation between attenuation and the refractive index of depressed layer (Δ_1), so we fabricated few fibers with Ring-core profile as figure 1-2 to investigate about relations between Δ_1 and attenuation (Fig. 2-1). By the before-mentioned research, it became clear that there is suitable Δ_1 to achieve low attenuation. In the figure, Δ_1 is normalized setting the Δ_1 of conventional P-MDF^{EA} as 1.

P-MDF with ring-core profile was optimized by computer simulation setting Δ_1 around suitable value for the lowest transmission attenuation, and fabricated based on calculation results (Table 3). As shown in table, dispersion is suppressed around 13ps/nm/km, dispersion slope was lower than 0.07ps/nm2/km, Aeff is enlarged to 125μm^2, and attenuation, which has been about 0.240dB/km at lowest before, was reduced such a low value as 0.210dB/km. Dispersion and attenuation spectrum of this P-MDF with Ring-core profile are shown in Figure 2-2.
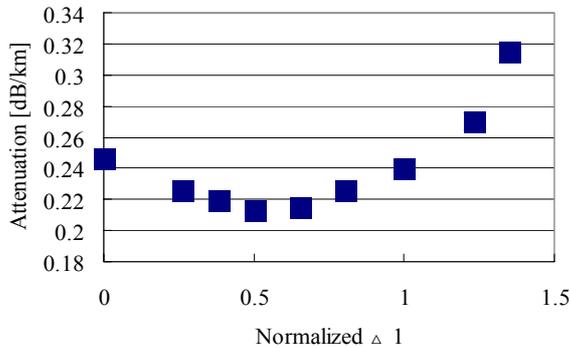

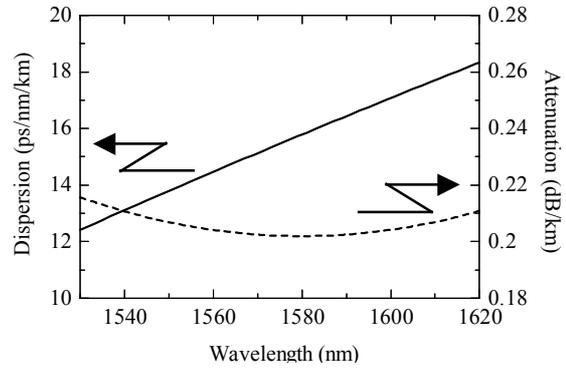Fig 2-1. Normalized $\triangle$ 1 vs. Attenuation

Fig. 2-2. Dispersion and Attenuation of Type-1

Table 3. The results of P-MDF with Ring-core profile (1550nm)

Fiber	Attenuation	Dispersion	Slope	DPS	Aeff	PMD	Bend Loss
	dB/km	ps/nm/km	ps/nm^2/km	nm	μm^2	ps/rkm	dB/m
Type-1	0.210	13.5	0.068	207	125	0.05	6

3. Development of low attenuation P-MDF with F-doped clad

As another approach to decrease the attenuation of P-MDF, F-doped clad method was tried selecting the same profile with conventional P-MDF (Fig. 1-1). As the result, the attenuation of P-MDF was successfully

decreased to 0.180dB/km from traditional value as 0.190dB/km. Moreover, by optimizing the profile, dispersion was decreased to 12.9ps/nm/km keeping Aeff 95μm^2, so the suppression of a maximum accumulated dispersion would be achieved (Table 4). Dispersion and attenuation characteristics of P-MDF with F-doped clad are shown in Figure 3, and attenuation is suppressed under 0.20dB/km from C-band to L-band.
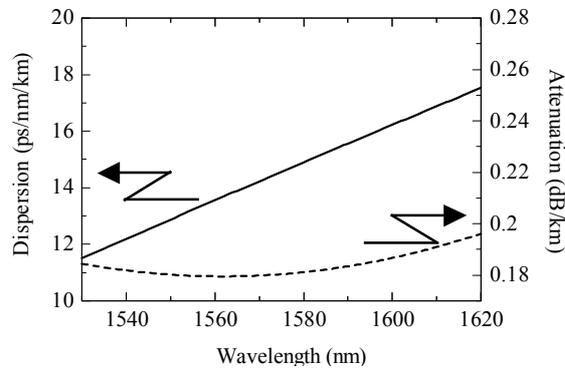

Fig. 3.   Dispersion and Attenuation of Type-2

Table 4. The results of P-MDF with F-doped clad (1550nm)

Fiber	Attenuation	Dispersion	Slope	DPS	Aeff	PMD	Bend Loss
	dB/km	ps/nm/km	ps/nm^2/km	nm	μm^2	ps/rkm	dB/m
Type-2	0.180	12.9	0.068	190	95	0.05	10

4. Total characteristics of Type-1, 2 P-MDF + N-MDF

Total characteristics of developed two types of P-MDF plus N-MDF are shown in Table 6. N-MDF was optimized setting dispersion about −13ps/nm/km, as shown in Table 5, to compensate dispersion characteristics of these two types of P-MDF. In this new N-MDF, absolute value of dispersion slope was enlarged to −0.070ps/nm^2/km, so dispersion flatness of total line could be achieved in the wide band.

As a result, future's long-haul high-bit-rate WDM transmission would be enabled using these types of transmission line.

Table 5. The characteristics of N-MDF (1550nm)

Fiber	Attenuation	Dispersion	Slope	DPS	Aeff	PMD	Bend Loss
	dB/km	ps/nm/km	ps/nm^2/km	nm	μm^2	ps/rkm	dB/m
N-MDF	0.220	-13.0	-0.070	186	35	0.05	5

Table 6. Characteristics of total links (1550nm)

Fiber	Attenuation	Dispersion	Slope	Aeff	PMD
	dB/km	ps/nm/km	ps/nm^2/km	μm^2	ps/rkm
Type-1 + N	0.215	0.0	-0.002	77	0.05
Type-2 + N	0.201	0.0	-0.001	65	0.05

5. References

[1] K.Mukasa et al, Proceeding of ECOC'97 (1997), Mo3C
[2] K.Mukasa et al, OFC'01 Technical Digest (2001), TuH7
[3] K.Mukasa et al, Proceeding of ECOC'00 (2000), 2-4-2
[4] K.Mukasa et al, Proceeding of ECOC'02 (2002), 5-1-2

Negative dispersion-flattened fiber for full-spectrum signal transmission in metropolitan networks

T. Okuno, H. Hatayama, T. Sasaki, K. Soma, A. Moto*, Y. Hirano*, M. Onishi, and M. Shigematsu

Optical Communications R&D Laboratories, Sumitomo Electric Industries, Ltd.
*Transmission Devices R&D Laboratories, Sumitomo Electric Industries, Ltd.
Tel :+81-45-853-7122, Fax :+81-45-851-1557, E-mail : okuno-toshiaki@sei.co.jp

Abstract: New dispersion-flattened fibers having negative dispersion of about −8ps/nm/km over whole telecommunication band are developed. Transmissions with 10Gb/s directly modulated LDs over 51km at 1275nm and over 80km at 1550nm are realized without dispersion compensation.
©2003 Optical Society of America
OCIS codes: (060.2280) Fiber design and fabrication, (060.2330) Fiber optics communications

1. Introduction

Metropolitan networks have become more important because of requirement of high speed communication for global internets. Recently, a directly-modulated laser (DML) has become attractive for metropolitan networks, because it costs lower compared with an externally modulated transmitter. DMLs, however, have a large chirp due to carrier-induced change in the mode index, which limits transmission distance owing to small dispersion tolerance. In order to improve the tolerance, many techniques have been studied. One method is, of course, to reduce the amount of chirp by improving laser diode designs. In a case of a improved 2.5Gb/s DML, successful 560km SMF transmission has been reported[1]. There are some other methods, for example, to cut down the chirp externally by a narrow band-pass filter[2], to use spectral inversion for inverting chirp direction[3], and so on.

While, another approach is to utilize negative dispersion property in a transmission fiber[4]. Because DMLs have positive chirp in principle, this negative dispersion compensates laser chirp and keep signal eyes opened. Recently, transmission over 100km with 10Gb/s DMLs has been succeeded with a negative dispersion fiber (NDF) in C-band[5]. Another type of fiber, water-peak-suppressed nonzero dispersion shifted fiber (WPS-NZDSF), for metropolitan networks has been suggested[6], which has low absolute dispersion values in whole telecommunication band from 1.3μm to 1.6μm, and whose water peak at 1.38μm is well suppressed. 10Gb/s CWDM transmission with this WPS-NZDSF has also been reported[7], which shows that transmission has been successfully realized over 28.5km in O-band and with 12km in 1.5μm band.

However, a type of above NDF has a large absolute dispersion value at O-band around 1.3μm, which limits transmission distance at this band. While, the WPS-NZDSF has a positive dispersion in C-band and L-band, and it is difficult to enlarge transmission distance over 20km in these regions. In order to solve these issues, we have developed a new fiber, a negative dispersion-flattened fiber (NDFF) for metropolitan networks, whose dispersion value of around −8ps/nm/km is almost constant in whole telecommunication band from O-band to L-band. Transmission experiments with 10Gb/s DMLs verify the validity of this NDFF, which successfully demonstrates the record distance of 51km both at O-band and C-band without dispersion compensation. In addition, although the nonlinear coefficient γ of a NDFF is a little higher than that of a typical SMF, input power up to 16dBm with 80km is available.

2. Fiber characteristics

Figure 1 shows a typical attenuation and dispersion properties of fabricated NDFFs. Dispersion is kept within an appropriate value of around −8ps/nm/km. For comparison, dispersion properties of a single mode fibers (SMF) and a fabricated NDF are also plotted in figure 1. It is apparent that OH excess loss around 1.38μm is well suppressed and the available wavelength region is from O-band to L-band. Typical fiber parameters are shown in table 1. Although attenuation is still a little bit higher than that of a SMF, it is expected to be reduced up to 0.2dB/km by improving manufacturing process. So as to decrease cut-off wavelength for full-spectrum transmission like NDFF1 whose cut-off wavelength is 1.23μm, effective area A_{eff} should be kept as small as 36μm^2. Splice loss between these NDFFs is 0.06dB, but is still as high as 0.38dB between NDFF and SMF, which is expected to be reduced to less than 0.2dB with an appropriate splice conditions.
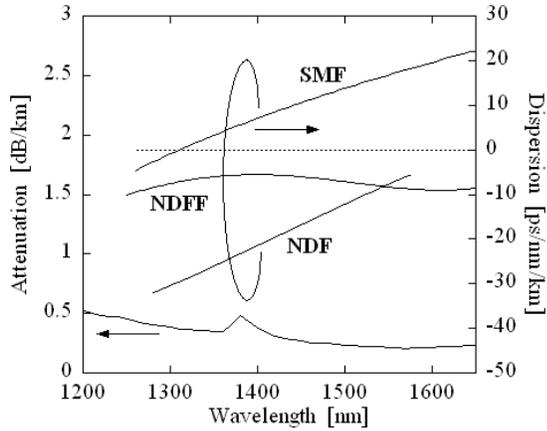
Fig.1 Typical attenuation and dispersion property of fabricated NDFF. Dispersion curves of SMF and NDF are also plotted.

Table 1 Fiber parameters of fabricated NDFFs. For comparison, parameters of fabricated NDF and conventional SMF are put.

	α @1310nm	α @1550nm	D @1310nm	D @1550nm
NDFF1	0.40	0.224	-6.9	-6.7
NDFF2	0.46	0.214	-8.7	-8.3
SMF	0.33	0.19	-0.08	16.4
NDF	0.35	0.215	-29.6	-7.9
	[dB/km]	[dB/km]	[ps/nm/km]	[ps/nm/km]

	Dslope @1550nm	A_eff	PMD
NDFF1	-0.043	36.1	0.03
NDFF2	-0.020	43.6	0.02
SMF	0.056	80	0.02
NDF	0.091	57	0.11
	[ps/nm²/km]	[μm²]	[ps/rt-km]

3. 10Gb/s directly modulated LD transmission experiments

In order to evaluate the performance of NDFFs, 10Gb/s directly modulated transmission experiments are carried out. Tested wavelengths of DFB-LDs are 1275nm, 1310nm, and 1550nm, in O-band and C-band. Output power of each laser is 7dBm, -2.5dBm, 7dBm, respectively. Extinction ratio is 7dB and cross-point is set to around 45%. Transmitted signal is 10Gb/s PRBS2^{31}-1. A typical PIN-PD type receiver is used for BER measurements.

First, transmission performance in O-band is evaluated. Figure 2 (a) shows BER dependence on the NDFF length. Because of the effect of accumulate negative dispersion, it can be observed that sensitivity of the receiver improves as the fiber length becomes longer. 51km transmission can be successfully realized with negative penalty of −3.5dB. Longer distance conditions cannot be evaluated due to loss limit in our experimental setup. Figure 2 (b) shows dependence of penalty on fiber length for two different wavelengths. Difference of penalty between the two wavelengths is due to the difference of the dispersion value at each wavelength.

For comparison, fabricated NDFs in table 1 are evaluated. Figure 2 (c) shows measured BERs in the case of 25km NDF by two different wavelengths of 1275nm and 1312nm. Although sensitivities are improved, error floor is clearly observed in each wavelength. Therefore, it is confirmed that large amount of negative dispersion more than −750ps/nm also limits transmission distance.

(a) NDFF (λ=1275nm)

(b) Dependence of penalty on fiber length for different wavelengths
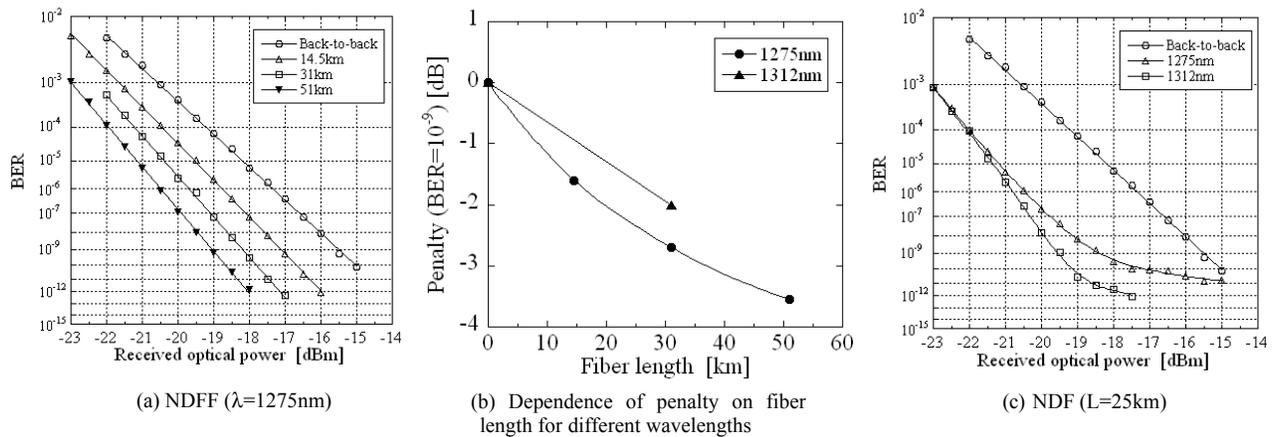
(c) NDF (L=25km)

Fig.2 Measured BER data for 1.3μm band signals.

Next, transmission performance at 1.55μm DML is examined. Figure 3 (a) shows measured BERs for NDFFs with different lengths. Error free transmission is acquired up to 80km NDFF, whose penalty is still improved as −1.9dB.

BER measurements for SMFs are also carried out. Relation between fiber lengths and penalties derived from these measured BER results is shown in figure 3 (b). Transmission more than 80km is expected for suggested NDFF, while the penalty significantly increases with only 11km SMF. As a result of these experiments, for 10Gb/s DMLs transmission, transmission distance over 51km successfully demonstrated at both O-band and C-band is the record length without dispersion compensation.
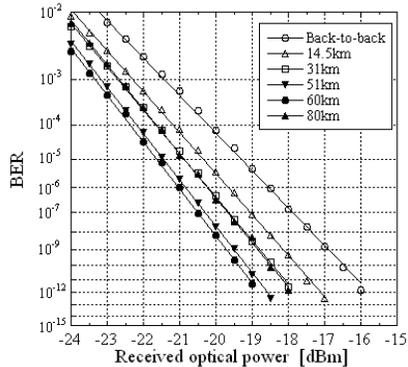
(a) NDFF
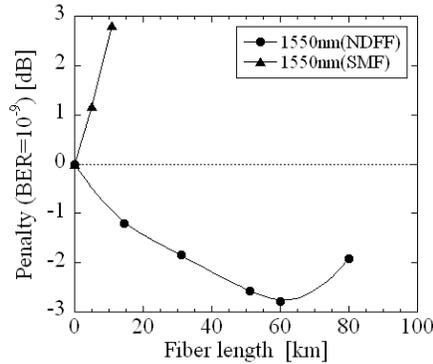
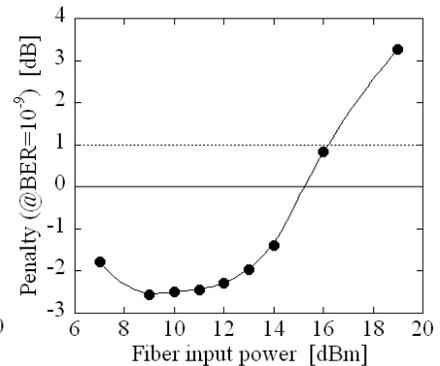(b) Dependence of penalty on fiber length

Fig.4 Fiber input power vs. penalty for NDFF with 80km length.

Fig.3 Measured transmission performance for 1.55μm signals.

Finally, in order to evaluate effect of nonlinearity, input power dependence of NDFFs is investigated at 1.55μm. A booster EDFA is simply inserted in front of 80km NDFFs. Figure 4 shows fiber input power versus penalty. In spite of about 2.5times larger nonlinearity of a NDFF than that of a SMF, it is verified that input power up to 16dBm is allowable with less than 1dB penalty. These results indicate that loss budget in CWDM systems can be increased without significant signal distortion by utilizing an optical amplifier, such as a discrete Raman amplifier[8].

4. Conclusion

We develop new types of negative dispersion flattened fibers for metropolitan networks, which has almost constant negative dispersion around −8ps/nm/km in whole telecommunication band from 1250nm to 1650nm. 10Gb/s signal transmission both 1.3μm and 1.55μm with directly modulated LDs is successfully demonstrated over 51km distance without dispersion compensation, which is the record length reported to date. Especially, transmission distance of more than 80km is also possible at around low loss wavelength band, such as C-band. Input power of up to 16dBm is allowed without significant signal distortion. These results support the validity of this fiber to full-spectrum metropolitan networks.

References

[1] L. Nelson, I. Woods, and J. K. White, "Transmission over 560km at 2.5Gb/s using a directly modulated buried heterostructure gain-coupled DFB semiconductor laser", Proc. OFC2002, ThF7 (2002).

[2] P. A. Morton, G. E. Shtengel, L. D. Tzeng, R. D. Yadvish, T. Tanbun-Ek, and R. A. Logan, "38.5km error free transmission at 10Gbit/s in standard fiber using a low chirp, spectrally filtered, directly modulated 1.55μm DFB laser", Electron. Lett., vol.33, pp.310-311 (1997).

[3] M. C. Tatham, X. Gu, L. D. Westbrook, G. Sherlock, and D. M. Spirit, "Transmission of 10Gbit/s directly modulated DFB signals over 200km standard fiber using mid-span spectral inversion", Electron. Lett., vol.30, pp.1335-1336 (1994).

[4] D. A. Atlas, A. F. Elrefaie, M. B. Romeiser, and D. G. Daut, "Chromatic dispersion limitations due to semiconductor laser chirping in conventional and dispersion-shifted single-mode fiber systems", Opt. Lett., vol.13, pp.1035-1037 (1988).

[5] I. Tomkos, B. Hallock, I. Roudas, R. Hesse, A. Boskovic, J. Nakano, and R. Vodhanel, "10-Gb/s transmission of 1.55-μm directly modulated signal over 100km of negative dispersion fiber", IEEE Photon. Technol. Lett., vol.13, pp.735-737 (2001).

[6] M. Tanaka, T. Okuno, H. Ohmori, T. Kato, Y. Yokoyama, S. Takaoka, K. Kunitake, R. Uchiyama, S. Hanazuka, and M. Nishimura, "Water-peak-suppressed non-zero dispersion shifted fiber for full spectrum coarse WDM transmission in metro network", Proc. OFC2002, WA2 (2002).

[7] I. Sogawa, N. Kaida, K. Iwai, T. Takagi, T. Nakabayashi, and G. Sasaki, "Study on full spectrum directly modulated CWDM transmission of 10Gb/s per channel over water-peak-suppressed non-zero dispersion shifted fiber", Proc. ECOC2002, 8.2.1, (2002).

[8] T. Miyamoto, T. Tsuzaki, T. Okuno, M. Kakui, M. Hirano, M. Onishi, M. Shigematsu, and M. Nishimura, "Highly-nonliner-fiber-based discrete Raman amplifier for CWDM systems", Proc. OFC2003, MF19, (2003).

Polarization-Insensitive Single-Pump Optical Parametric Amplifier by Depolarization of the Pump

T. Luo[1], C. Yu[1], L.-S. Yan[1], Z. Pan[2], Y. Wang[1], Y. Song[1], A.E. Willner[1]

[1]*Department of Electrical Engineering–Systems, University of Southern California, Los Angeles, CA. 90089-2565*
[2]*Department of ECE, University of Louisiana, Lafayette, LA 70504*
Phone: (213) 740-1488, Fax: (213) 740-8729, Email: luot@usc.edu

Abstract: We demonstrate a polarization-insensitive single-pumped optical-parametric-amplifier by depolarizing the pump using a polarization controller followed by a piece of polarization-maintaining fiber with ~ 100-ps DGD. The polarization-dependent-gain is reduced from 8 dB to <1 dB.
©2004 Optical Society of America
OCIS codes: (190.4410) Nonlinear optics, parametric processes, (190.4370) Nonlinear optics, fibers

1. Introduction

Optical parametric amplifiers (OPAs) have traditionally been considered optical "mixers." As such, they can be used for a variety of applications, including wavelength conversion, signal amplification, optical sampling, OTDM switch, and 2R/3R regeneration, as well as other optical signal-processing functions [1,2].

OPAs generally require passing a signal and one or two pumps through a nonlinear material. OPAs have been demonstrated on semiconductor material [3], on quasi-phase-matched lithium niobate [4], and in different types of optical fiber [1,5]. Typically, due to the requirement of phase matching, OPAs tend to be highly sensitive to the polarization state of the incoming signal relative to the pump, with the sensitivity being nearly as high as the total gain itself.

Previously published work on polarization insensitive OPAs has taken the approach of introducing polarization diversity by launching two orthogonally-polarized pumps into the OPA. This approach has been accomplished in fiber in the following two ways: (i) using two separate pumps with orthogonal polarization states [6], and (ii) splitting one pump into two orthogonal polarization states to counter propagate in a Sagnac loop [7]. However, a recent paper has noted that using orthogonal pumps is limited in achieving polarization insensitivity due to the difficulty in maintaining polarization orthogonality, with the performance sensitivity remaining ~ 4 dB [8].

Applying pump depolarization to overcome polarization dependent gain (PDG) in optical amplifiers has been experimentally demonstrated in Raman amplifiers [9]. However, polarization-insensitive OPA using pump depolarization has never been reported so far.

We demonstrate a polarization-insensitive single-pumped OPA by depolarizing the 10 Gb/s phase modulated pump using a polarization controller followed by polarization-maintaining fiber (with 102-ps DGD) before launching into the nonlinear fiber medium. The depolarization of the pump over the entire Poincare sphere tends to produce a better average phase matching for input signals of any polarization state. The PDG of the OPA at certain wavelengths is reduced from ~ 8 dB to less than 1 dB after depolarization. Over the 20-nm signal wavelength range, the maximum PDG is still less than 2 dB. Moreover, negligible changes in the noise figure (NF) of the OPA after depolarization is observed.

2. Pump Depolarization Concept and Experimental Setup
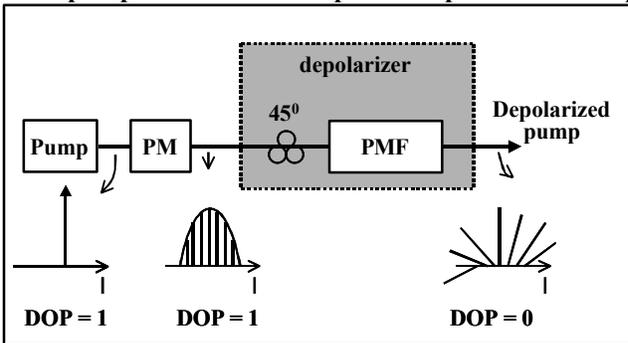

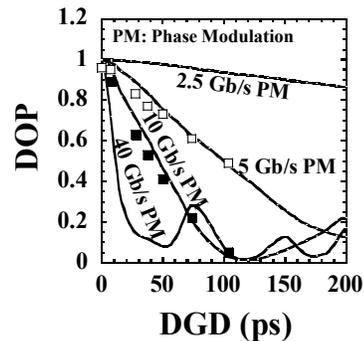Figure 1 (a): Concept of pump depolarizer using a PC followed by PMF

Figure 1 (b): Performance of the depolarizer under different phase modulation speed. Simulation: solid lines; experimental: squares

The pump depolarizer used to achieve polarization-insensitivity in the OPA is shown in Figure 1 (a). In general, pump in an OPA is phase modulated in order to broaden its bandwidth and hence to suppress the stimulated Brillouin scattering (SBS) effect. If the phase modulated pump is aligned 45^0 with respect to one of the polarization axes of polarization maintaining fiber (PMF), then each frequency component of the pump experiences different phase delay between the fax axis and the slow axis due to the differential group delay (DGD) in the PMF. At the PMF output, the polarization of each frequency component is different from each other. Thus the pump is depolarized. Since the power of completely depolarized pump is evenly distributed along all polarization states, incoming signal with any polarization state can be amplified equally. The performance of such a depolarizer is evaluated by measuring the degree of polarization (DOP) of the output pump using a polarimeter. Figure 1 (b) shows both the simulated (solid lines) and experimental (solid and hollow squares) results of the output DOP versus DGD for different phase modulation speed. We can see that at 10 G modulation speed, PMF with ~ 100-ps DGD can reduce the DOP of the pump to ~ 0, which means the pump is almost completely depolarized.
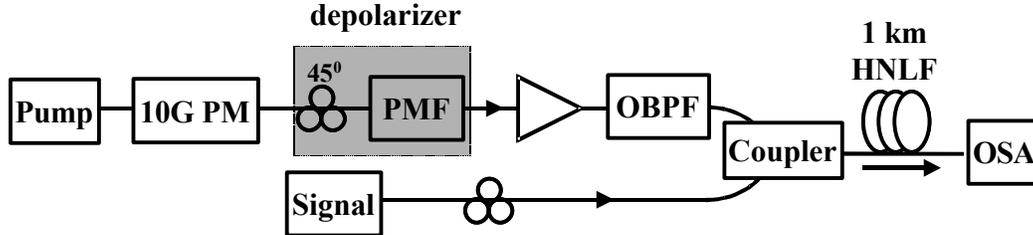

Figure 2: Experimental setup. PM: phase modulation, OBPF: optical bandpass filter, HNLF: highly nonlinear fiber

Figure 2 shows the experimental setup. The input signal and depolarized pump are launched into a 1-km highly nonlinear fiber (HNLF), which is the amplification medium. The pump wavelength is set at the HNLF's zero-dispersion wavelength λ_0, ~1552 nm. The dispersion slope and nonlinear coefficient γ of the HNLF are 0.045 ps/(nm^2·km) and 9.1/(W·km), respectively. Although PMF with different DGD values combined with different phase modulation frequencies can be selected to reduce the DOP of the pump as shown in Fig.1 (b), according to the available PMF, we use 10 Gb/s phase modulation and a piece of PMF with ~100-ps DGD in our experiment. After the depolarizer, the pump is amplified by a high power EDFA followed by a 0.25 nm bandwidth optical bandpass filter (OBPF), which filters out the amplified spontaneous emission (ASE) noise of the EDFA. The state of polarization (SOP) of the input signal is controlled by a polarization controller (PC), which is composed of one half-wave plate (HWP) and one quarter-wave plate (QWP). At the output, the optical spectrum is monitored using an optical spectrum analyzer (OSA).
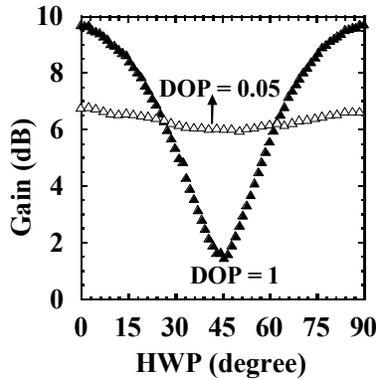
3 Results and Discussion

Figure 3: Signal power gain changes against SOP of input signal when DOP is 1 and 0.05
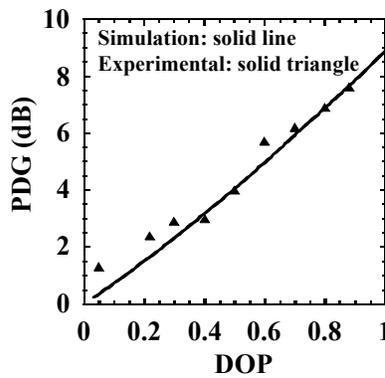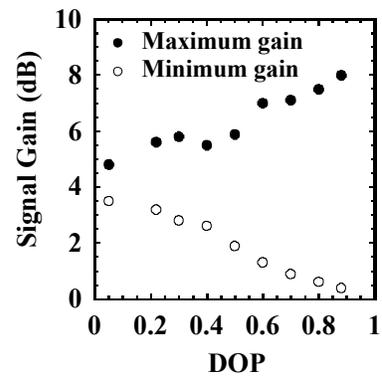
Figure 4 (a): PDG versus DOP of the pump.

Figure 4 (b): Maximum and minimum signal gain versus DOP of the pump

Figure 3 shows the comparison of the experimental results of the polarization sensitivity of the OPA when the DOP of the pump is ~ 1 and ~ 0.05. The input signal is set at a wavelength of 1547 nm and the power is ~ –16 dBm. The pump power is set to 16.5 dBm. Without pump depolarization, the signal gain is maximized when the polarization state of the signal is parallel with that of the pump and minimized when the polarization state of the signal is orthogonal with that of the pump. As shown in Figure 3, the fluctuation of the signal gain is more than 8 dB as the SOP of the input signal changes. However, with the depolarizer placed in the path of the pump, the DOP of the output pump is decreased to ~0.05, which means the pump is almost completely depolarized. As depicted in Figure 3, the fluctuation of the signal gain is reduced to less than 1 dB while changing the SOP of the input signal. The residual fluctuation may arise from polarization dependent loss (PDL) or polarization mode dispersion (PMD) in the

setup. Note that the OPA gain after depolarizing the pump is approximately 3 dB less than the maximum value when there is no depolarization of pump because the pump power is distributed evenly into different polarization states.

In addition to PDG measurement at pump DOP of 1 and 0.05 as shown in Figure 3, the relationship between the gain fluctuation of the OPA and DOP of the pump is investigated in more detail. Figure 4 (a) shows both the simulation and experimental results. PDG decreases as DOP decreases from 1 to 0. When the DOP of the pump is decreased to less than 0.2, the PDG decreases to less than 2 dB. Therefore allowable fluctuation can be chosen for different applications. Figure 4 (b) is the measurement of the maximum and minimum gain of the OPA when the DOP of the pump varies from 0 to 1. As DOP of the pump is decreasing from 1 to 0, the maximum gain of the signal decreases to ~3 dB less and the minimum gain of the signal approaches from 0 dB to the same value as well.
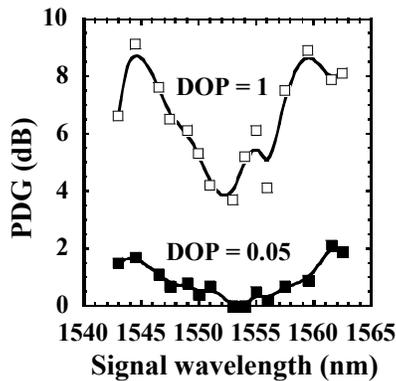

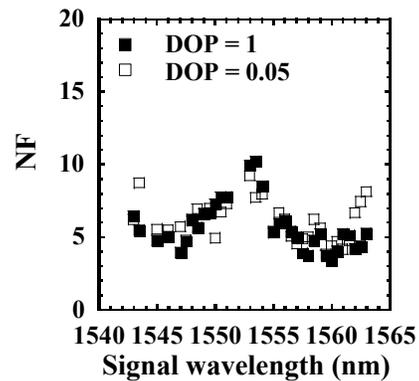Figure 5 (a): PDG spectrum when pump DOP is 1 and 0.05

Figure 5 (b): NF of the amplifier before and after pump depolarization

Figs. 3 and 4 show the gain performance at a certain signal wavelength, while Fig. 5(a) shows PDG versus the input signal wavelength when the DOP of the pump is ~1 and ~ 0.05. Here the signal wavelength is scanned from 1543 nm to 1563 nm. Without depolarization, PDG of the OPA varies from ~ 4 dB to ~ 9 dB depending on the wavelength of the input signal. After depolarization, the PDG is decreased to less than 1 dB for the signal wavelength of 1546 nm through 1560 nm. Even though it increases a little when the signal wavelength is out of this range, PDG is < 2 dB for the whole range of the signal wavelengths mentioned above. Another important figure-of-merit for optical amplifiers is the noise figure (NF). The NF of the OPA is also measured using the optical spectrum analyzer technique for the signal wavelength from 1543 nm to 1563 nm. The experimental result is shown in Figure 5 (b). After pump depolarization, the NF does not change noticeably compared with polarized pump. The peak near the pump wavelength is mainly due to the fact that when the signal is close to the pump, partial overlapping of the pump and signal increases the noise.

4. References

[1] Hansryd, J; Andrekson, P.A.; Westlund, M.; Li, J.; and Hedekvist, P., "Fiber-based optical parametric amplifiers and their applications", **JSTQE**, vol. 8, pp. 506-520, 2002

[2] Radic, S.; McKinstrie, C.J.; Jopson, R.M.; Centanni, J.C.; and Chraplyvy, A.R., "All-optical regeneration in one- and two-pump parametric amplifiers using highly nonlinear optical fiber", **PTL**, vol. 15, pp. 957 –959, 2003

[3] Ding, Y.J.; Khurgin, J.B.; and Lee, S., "Transversely-pumped counter-propagating optical parametric oscillators and amplifiers: conversion efficiencies and tuning ranges", **JQE**, Vol. 31, pp. 1648 -1658, 1995

[4] Galvanauskas, A.; Wong, K.K.; El Hadi, K.; Hofer, M.; Fermann, M.E.; Harter, D.; Chou, M.H.; and Fejer, M.M., "Amplification in 1.2-1.7 µm communication window using OPA in PPLN waveguides", **Electronics Lett.**, vol. 35, pp.731–733, 1999

[5] Tang, R.; Lasri, J.; Devgan, P.; Sharping, J.E.; and Kumar, P., "Microstructure-fibre-based optical parametric amplifier with gain slope of /spl sim/200 dB/W/km in the telecom range", **Electronics Lett.**, vol. 39, pp. 195-196, 2003

[6] Wong, K.K.Y.; Marhic, M.E.; Uesaka, K.; and Kazovsky, L.G., "Polarization-independent and flat-gain CW two-pump fiber optical parametric amplifier and wavelength converter", **OFC**, TuS 5, 2002

[7] Wong, K.K.Y.; Marhic, M.E.; Uesaka, K.; and Kazovsky, L.G., " Polarization-independent one-pump fiber-optical parametric amplifier", **PTL**, vol. 14, pp. 1506 –1508, 2002

[8] Radic, S.; Mckinstrie, C.; and Jopson, R., "Polarization dependent parametric gain in amplifiers with orthogonally multiplexed optical pumps", **OFC**, ThK3, 2003

[9] Tokura, T.; Kogure, T.; Sugihara, T.; Shimizu, K.; Mizuochi, T.; and Motoshima, K., "Pump light depolarization method for low PDG Raman amplification", **OFC**, ThGG 24, 2002

Parametric amplification in optical fibers
with random birefringence

M. E. Marhic, K. K.-Y. Wong, and L.G. Kazovsky

Department of Electrical Engineering, Stanford University, 374 Packard Bldg., Stanford, California 94305
marhic@wdm.stanford.edu

Abstract: By averaging the OPA equations for fibers with random birefringence, we show that the gain coefficient with orthogonal pumps is significantly larger than would be expected in nonbirefringent fibers. This is verified by experiments.
©2003 Optical Society of America
OCIS codes: (060.2320) Fiber optics amplifiers and oscillators, (060.4370) Nonlinear optics, fibers.

1. Introduction

Recent work with fiber OPAs has been performed primarily with communication-type fibers, that are not non-birefringent fibers (NBFs), but are randomly-birefringent fibers (RBFs). As a result, states of polarization (SOPs) are not maintained in such fibers, but evolve randomly with distance. On the other hand, all the expressions derived to date for the gain of fiber OPAs assume perfect NBFs, and that the pump and signal SOPs do not change with distance. While theory matches well with experiments when all the waves launched with the same SOP, we have found in our work with orthogonally-polarized pumps [1] that the measured gain is substantially higher than would be expected if the pumps remained linearly polarized (LP) and orthogonal over the entire length. Since the orthogonal-pumps OPA is an important candidate for making polarization-insensitive OPAs [1], it is desirable to develop a better understanding of its performance with real fibers, which are RBFs.

For this reason, and also to advance our understanding of all other types of OPAs, we have developed a formalism which allows us to calculate OPA gain in RBFs, for the first time to our knowledge. We write the basic OPA equations for arbitrary SOPs for all the waves, involving the appropriate elements of the susceptibility tensor. The fiber is modeled as short segments of NBF, connected by waveplates which introduce random SOP changes. The equations are then averaged, assuming a uniform distribution of SOPs over the Poincare sphere. The resulting equations are then solved, yielding the maximum parametric gain coefficient g. Based on the results, we find that the gain in an RBF with orthogonal pumps should be significantly larger than in an NBF, which has important practical implications for polarization-insensitive OPAs. We have also performed experiments which support this conclusion.

2. Theory.

We consider the interaction of four waves with frequencies ω_k (k=1,2,3,4 for first pump, second pump, signal, and idler, respectively), satisfying $\omega_1 + \omega_2 = \omega_3 + \omega_4 = \omega_c / 2$. The propagation constants are $\beta_k = \beta(\omega_k)$, and $\Delta\beta = \beta_3 + \beta_4 - \beta_1 - \beta_2$ is the propagation constant mismatch. $\vec{A}_k(z) = A_k(z)\hat{e}_k(z)$ is the slowly-varying complex phasor (vector) of the field; $A_k(z)$ is its complex amplitude (scalar); $\hat{e}_k(z)$ is its unit-magnitude polarization vector; we also introduce $\hat{e}_5(z)$, which is orthogonal to $\hat{e}_1(z)$. $P_k(z) = |A_k(z)|^2$ is the power of the field at ω_k. We assume that the pumps are not depleted; hence P_1 and P_2 remain constant. The propagation equations for the A_k's are [2]

$$\frac{dA_k}{dz} + (\hat{e}_k^* \cdot \frac{d\hat{e}_k}{dz})A_k = i\gamma(a_{kk}P_k + 2a_{kl}P_l)A_k, \qquad\qquad k=1,2,\ l=3-k \qquad (1)$$

$$\frac{dA_k}{dz} + (\hat{e}_k^* \cdot \frac{d\hat{e}_k}{dz})A_k = 2i\gamma(a_{k1}P_1 + a_{k2}P_2)A_k + 2i\gamma\sqrt{P_1P_2}[\hat{e}_1,\hat{e}_2,\hat{e}_l^*,\hat{e}_k^*]A_l^* \exp(-i\Delta\beta z), \qquad k=3,4,\ l=7-k \qquad (2)$$

where: $[\vec{a},\vec{b},\vec{c}] = [(\vec{a}\cdot\vec{b})\vec{c} + (\vec{b}\cdot\vec{c})\vec{a} + (\vec{c}\cdot\vec{a})\vec{b}]/3$; $[\vec{a},\vec{b},\vec{c},\vec{d}] = [\vec{a},\vec{b},\vec{c}]\cdot\vec{d}$; $a_{kl} = [\hat{e}_k,\hat{e}_k^*,\hat{e}_l,\hat{e}_l^*]$.

We then average (1) and (2), assuming that: (i) the SOPs are uniformly distributed over the Poincare sphere; (ii) identity or orthogonality of SOPs is preserved along the fiber. By associating SOPs in pairs with opposite handedness, we can show that the second terms on the LHS's of (1) and (2) average out to zero. To perform the averaging (denoted by $\langle \bullet \rangle$), we use the standard angles χ and ψ locating SOPs on the Poincare sphere [3]. We only consider OPAs in which the input waves have identical SOPs, or some are orthogonal to others. We find that $\langle a_{kk} \rangle = 8/9$ and $\langle a_{15} \rangle = 4/9$; these numbers are then used to evaluate the averages of the first two terms on the RHS's of (1) and (2), which correspond to pump-induced SPM and XPM. To average the last term in (2), which corresponds to FWM, we need to consider several possibilities for the SOPs, which lead to $\langle [\hat{e}_1, \hat{e}_1, \hat{e}_5^*, \hat{e}_5^*] \rangle = 2/9$, $\langle [\hat{e}_1, \hat{e}_5, \hat{e}_1^*, \hat{e}_5^*] \rangle = 4/9$, $\langle [\hat{e}_1, \hat{e}_1, \hat{e}_1^*, \hat{e}_1^*] \rangle = \langle a_{11} \rangle = 8/9$. The averaged (1) and (2) then take on a form similar to the OPA equations in an NBF, but with different coefficients. The solution proceeds as usual, providing expressions for the parametric gain g (for simplicity, we consider here only the maximum gain, obtained under optimum phase matching).

By choosing different combinations of initial SOPs, several types of OPA can be modeled. In particular, we have shown that if the gain g of an NBF OPA with all parallel LP waves is $g_1 = 1$, then if the same waves are launched into an RBF, the resulting g_2 is 8/9. The small difference between the two explains why there is good agreement between experiments with RBFs and theory for NBFs. For an NBF OPA with orthogonal LP states, we have shown that $g_3 = 1/3$ [1]. However, with an RBF, this becomes $g_4 = 4/9$, which is *larger* than g_3 (this is because now the pumps will at times be circularly polarized, in which case g has the large value 2/3 [4]). Stated differently, if we had an NBF, going from parallel to orthogonal pumps would reduce g by $\rho_n = g_1/g_3 = 3$, but with an RBF, the reduction would only be by $\rho_r = g_2/g_4 = 2$. This is a significant difference, which should be experimentally verifiable.

3. Experiments.

We have performed experiments to verify these predictions. The experimental configuration is shown in Fig. 1. The parametric gain medium consists of 500 km of HNL-DSF (Sumitomo Electric Industries, Ltd.) with a nominal zero-dispersion wavelength $\lambda_0 = 1561.5$ nm, and a dispersion slope of 0.03 ps/nm^{2}km. γ is
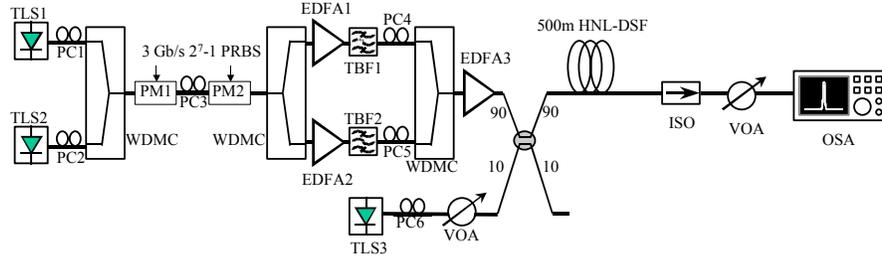

Fig. 1. Experimental setup

17 W^{-1}km^{-1}. Two tunable laser sources, TLS1 and TLS2, set at 1545.9 nm (λ_{p1}) and 1574.4 nm (λ_{p2}), respectively, serve as the pump sources, with the average wavelength approximately equal to λ_0. The CW pumps are phase-modulated by a 3 Gb/s 2^7-1 pseudo-random bit sequence (PRBS) to suppress SBS. Two phase modulators, PM1 and PM2, are cascaded to obtain a high Brillouin threshold. The polarization controllers, PC1 and PC2, align the pump SOP's with PM1, while PC3 aligns them with PM2, which helps to reduce the insertion loss. The two pumps are combined and separated by WDM couplers, followed by optical tunable bandpass filters (TBF1 and TBF2) with 0.35 nm bandwidth, and amplified by a C-band EDFA (EDFA1) and an L-band EDFA (EDFA2), respectively. They are then recombined by another WDM coupler, and amplified by EDFA3, with a maximum output power of 27 dBm. A CW signal provided by TLS3 is used to measure the OPA signal gain. It is combined with the output of EDFA3 by a 90/10 coupler. Polarization controllers (PC4 and PC5) are used to ensure that the two pumps incident on the HNL-DSF are either parallel or orthogonal. The former is achieved by maximizing the OPA gain, by monitoring it with the optical spectrum analyzer (OSA); the latter by minimizing OPA gain. The powers of the two pumps at the input of HNL-DSF are 22.5 dBm (λ_{p1}) and 21.9 dBm (λ_{p2}), respectively, while the signal power is –16 dBm. (The slight imbalance between the pumps is due to the SRS effect, because λ_{p1} serves as a Raman pump for λ_{p2}.) The output spectrum of HNL-DSF, followed by an isolator which prevents any reflection

from the variable optical attenuator (VOA), is observed at the OSA.

Fig. 2 shows the gain spectra obtained when the pumps have either identical or orthogonal SOPs. It can be seen that maximum gain occurs at the same wavelength for the two cases (1561 nm), in agreement with other results of the preceding theory. Since the maximum power gain of an OPA is given by $G_{max} = \cosh^2(gL)$, we can extract the experimental values of g_2L and g_4L from Fig. 2, and calculate the experimental value of their ratio, $\rho_r = g_2L/g_4L = g_2/g_4$, which is to be compared to the theoretical value $\rho_r = 2$. We find that $\rho_r = 1.7$, in good agreement with the theoretical value (within 15%), and very far from $\rho_n = 3$, the ratio for NBF. The difference with theory may be explained in part by: Raman interaction between the pumps; longitudinal fluctuations of λ_0; limited validity of the basic assumptions.
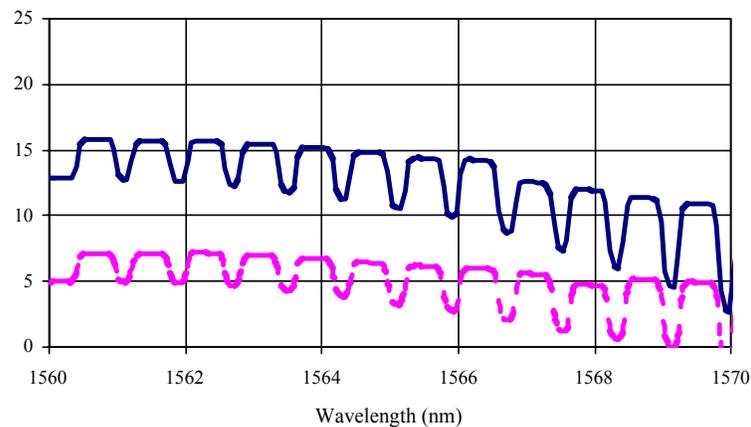

Fig. 2. OPA gain spectra for: identical (solid line) and orthogonal (dashed line) pump SOPs
in randomly-birefringent fiber.

4. Discussion

An important practical consequence of $\rho_r = 2$ is that the gain penalty associated with achieving polarization independence by using two orthogonal pumps is not as severe as was originally anticipated on the basis of the theory for NBFs [1]. In fact, this phenomenon renders the gain for this scheme identical to that of the polarization diversity scheme that we have also investigated [5]. Another consequence is that using RBFs with randomly varying SOPs should yield higher gain than in RBFs in which the input SOPs are aligned with the principal states of polarizations (PSPs), which behave essentially as NBFs, as long as the fiber is not too long [6].

5. Conclusion.

We have derived the fiber OPA equations for waves having arbitrary SOPs. We then averaged them by assuming a uniform distribution of SOPs on the Poincare sphere, in the cases where the waves have either identical or orthogonal SOPs. We solved the averaged equations, and calculated the parametric gain coefficient g. We found that going from identical to orthogonal pump SOPs in RBFs reduces g only by a factor of 2, and we have experimentally verified this fact; this has important implications for the design of polarization-insensitive OPAs. The general formalism introduced here is very general, and should help improve the understanding of the performance of OPAs using fibers with random birefringence, which are used in most practical systems.

References

[1] K. K.-Y. Wong, M. E. Marhic, K. Uesaka,, and L. G. Kazovsky, IEEE Photon. Technol. Lett., **14**, 911-913 (2002).
[2] M. E. Marhic, K. K.-Y. Wong, and L. G. Kazovsky, J. Opt. Soc. Amer., in press.
[3] M. Born and E. Wolf, *Principles of Optics* (Pergamon, New York, 1970), p. 31.
[4] M. E. Marhic, K. K.-Y. Wong, and L. G. Kazovsky, IEE Electron. Lett., **39**, 350-351 (2003).
[5] K. K.-Y. Wong, M. E. Marhic, K. Uesaka, and L. G. Kazovsky, IEEE Photon. Technol. Lett., **14**, 1506-1508 (2002).
[6] S. Radic, C. Mckinstrie, and R. Jopson, OFC 2003 Technical Digest, p. 508.

New nonlinear fibers with application to amplifiers

Masashi Onishi

Optical Communications R&D Laboratories, Sumitomo Electric Ind., Ltd., 1, Taya-cho, Sakae-ku, Yokohama 244-8588 Japan
Tel.: +81-45-853-7172, Fax: +81-45-851-1565, e-mail: onishim@yklab.sei.co.jp

Abstract: Highly nonlinear fibers (HNLFs) have been explored as candidates for the media of Raman amplification and optical parametric amplification with broad gain bandwidths. This paper reviews state-of-the-art HNLFs and the application to discrete Raman amplification.
©2003 Optical Society of America
OCIS codes: (060,2280) Fiber design and fabrication, (060,4370) Nonlinear optics, fibers

1. Introduction

Silica-based optical fibers with enhancing the 3rd-order optical nonlinearity have various attractive applications such as discrete Raman amplification [1], optical parametric amplification (OPA) [2], wavelength conversion [3], supercontinuum (SC) generation [4], optical-3R regeneration [5], soliton pulse compression [6] and so on for future high-capacity systems and photonic networks. Although the optical nonlinearity of silica glass is relatively small in comparison with those of other glass materials such as Tellurite glass and Chalcogenide glass, the silica-based fibers are attractive because of their low transmission loss (long effective length), chromatic dispersion, single-mode operation and easy connection to transmission fibers.

In this paper, recent development of highly nonlinear fibers (HNLFs) especially for the optical amplification is reviewed, and their application to the discrete Raman amplifier for CWDM systems is demonstrated.

2. Highly nonlinear fibers

In order to enhance the optical nonlinearity of the fiber, the relative refractive index difference (Δn) between the core and the cladding must be increased. In general, GeO$_2$ and fluorine are doped to the core and the cladding, respectively. The maximum Δn around 3% was realized with an attenuation less than 1dB/km at 1.55μm-band employing the vapor-phase axial deposition (VAD) method [7]. Under the single-mode operation condition, the small core diameter with a few microns confines the optical power, and it enhances the optical nonlinearity of the fiber. The nonlinear coefficients ($\gamma = k*n2/Aeff$) around 20 [1/W/km] have been reported [7]. In order to apply the HNLFs to the various applications, the chromatic dispersion is critical issue. Figure 1 shows the schematic chromatic dispersion spectra of various types of HNLFs. In the case of FWM or XPM-based applications, the dispersion should be zero around the operation wavelength for satisfying the phase matching condition. On the other hand, for the Raman amplification, the zero dispersion should be shifted in order to prevent FWM generation among signal channels. Furthermore, the zero dispersion slope around the operation window is required especially for the SC generation. Table 1 summarizes the performance of the available HNLFs
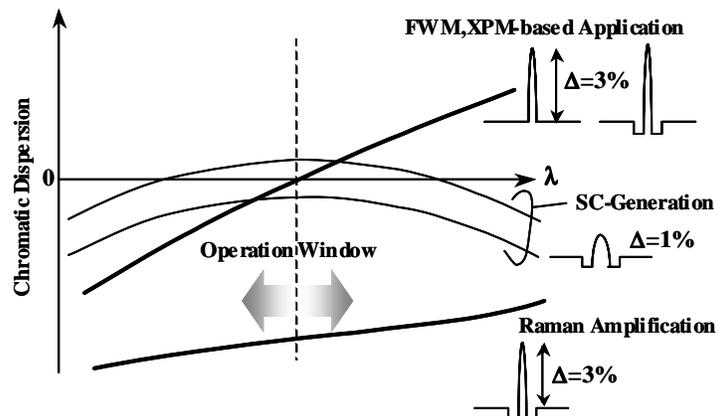

Fig. 1 Schematic chromatic dispersion spectra of HNLFs for various applications

Table 1 Fiber performances of various HNLFs (at 1550nm)

HNLF	γ [1Wkm]	Aeff [μm^2]	Dispersion [ps/km/nm]	Dispersion Slope [ps/km/nm^2]	Attenuation [dB/km]	PMD [ps/√km]	(Applications)
A	20	11	~0	+0.03	0.52	<0.1	**FWM, XPM-based OPA, Wavelength Conversion**
B	21	10	<-10	+0.01	0.46	<0.1	**Raman Amplification**
C	10	16	+0.1	~0.00	0.50	<0.1	**SC-generation**

with examples of possible application. In the fiber design, it is difficult to obtain the small dispersion slope less than +0.02ps/km/nm^2 at the zero dispersion wavelength (λ_0) around the 1.55μm-band with realizing the large Δn. Therefore, the γ of the HNLF with the flattened dispersion performance should be compromised in this case. Furthermore, the HNLF can be coupled with the SMF by the fusion splice with a splice loss around 0.2dB/splice.

3. Chromatic dispersion control

By enhancing the Δn of the core, the control of the λ_0 of the fiber becomes difficult. The calculated λ_0 as a function of the relative core diameter of the HNLFs with a Δn of 3% is shown in Fig. 2. As shown in this figure, the fluctuation of the core diameter with +/-0.5% results in the λ_0 shift of about 30nm. This requires the quite precise tuning of the fiber parameters in comparison with the conventional SMF or NZ-DSFs. Furthermore, the λ_0 must be stabilized in the longitudinal direction in order to realize the long effective length in the HNLF. This is the most crucial issue, when the HNLFs are applied to the practical applications such as OPA and wavelength conversion. The technologies for precise control of the fiber parameters have been improved at both stages of perform synthesizing and fiber drawing. Furthermore, the evaluation method for measuring the dispersion fluctuation in the longitudinal direction by using the OTDR has also been developed. The recent results have shown the λ_0 fluctuation within +/-0.3nm in 1 km in length, and they have contributed to the fantastic demonstration in OPA or wavelength conversion experiments.
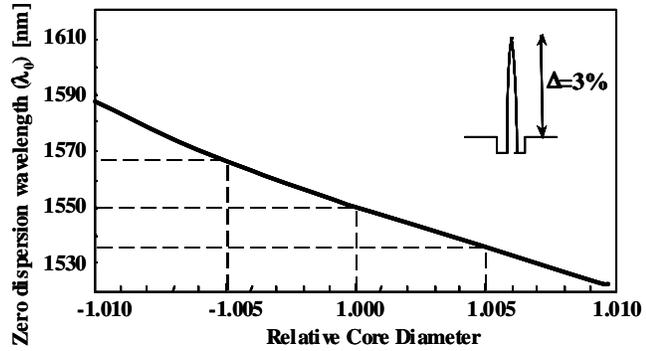
Fig. 2 Calculated relationship between
zero dispersion wavelength and core diameter

4. Attenuation of HNLFs

With increasing the optical nonlinearity, required fiber length can be shortened, and the attenuation of the HNLFs does not seriously affect to the nonlinear effects generation. However, in Raman amplification, it requires a few km of the HNLFs because of its small gain coefficient, and the pumping wavelengths or amplification bandwidth are overlapped with OH absorption peak of the HNLF in some cases. Therefore, the OH absorption should be eliminated even in the HNLFs. Generally, it is difficult to eliminate the OH species 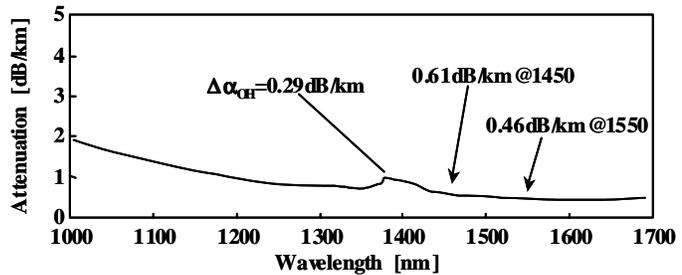from silica glasses doped with a high concentration of GeO2. Figure 3 shows the attenuation spectrum of the HNLFs for the discrete Raman amplification. By considering the dehydration process of the preform, the OH absorption peak ($\Delta\alpha_{OH}$) has been reduced to be around 0.29dB/km. Furthermore, the attenuation at 1550nm and 1450nm were also improved to be 0.46dB/km and 0.61dB/km, respectively.

Fig. 3 Attenuation spectrum of the HNLF for Raman Amplification

5. Discrete Raman Amplifier using HNLF

By using the HNLF, discrete Raman amplification experiment was demonstrated [8]. The experimental setup of HNLF-based fiber Raman amplifier (FRA) for 4-channel CWDM system is illustrated in Fig. 4. The wavelengths of 4-channels CWDM signals were arranged from 1511nm to 1571nm with 20nm spacing, and their bit rates were 2.5Gb/s. In order to realize flattened gain over 60nm, only two pumping sources oscillating at 1423nm and 1465nm were employed. In the FRA, a 3km of HNLF with a γ of 21 [1/W/km] was used. The dispersion of the HNLF was set at -13.6ps/km/nm at 1550nm in order to avoid the FWM and XPM generations in the HNLF. The multiplexed signals were transmitted over a conventional SMF. Figure 5 shows the input and output spectra of the FRA, when the total pumping power was 415mw at the fiber input. The net gain of each signal was 10dB, and its variance was as small as 1.5dB. The noise figure was 5.8dB in this case.   No FWM spectra were observed because of the large channel spacing of 20nm and the dispersion of -13.6ps/km/nm in the HNLF. Table 2 summarizes the power penalties of the transmission experiment. In the case of the transmission over 100km of SMF with FRA, the power
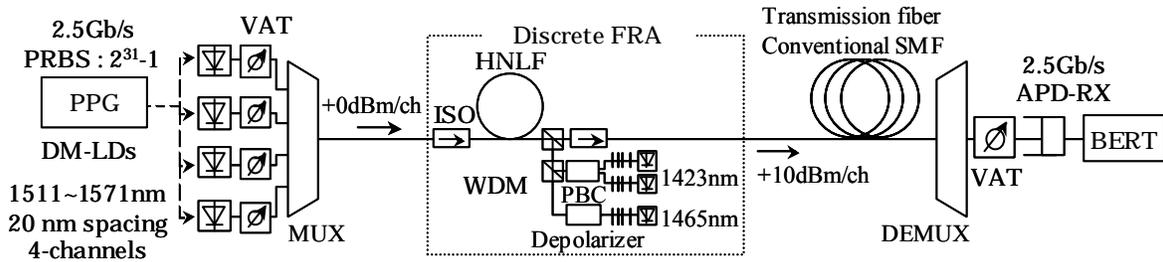
Fig.4 Experimental setup of fiber Raman amplifier for 4-channles CWDM systems

penalties of 4 signals were much improved in comparison with the result from the transmission without FRA. Furthermore, 4-channels of CWDM transmission over 150km of SMF was successfully realized by employing the FRA, and their power penalties were less than 1.8dB in all channels.

6. Summary

Silica-based highly nonlinear fibers and their recent situations were reviewed. For the Raman amplification, further effort against the OH-free performance is expected in order to improve the pumping efficiency. On the other hand, for the XPM or FWM-based applications, the precise chromatic dispersion control and its uniformity in the longitudinal direction are indispensable for the practical applications. Recently, they have been improved, and several optical parametric amplification experiments with a quite broad bandwidth over 30nm have been demonstrated [2].
Furthermore, the holey fiber is another option. It is considered that the holey fiber with a quite small spot size around $1\mu m^2$ will be the very strong candidates for future application, if the breakthroughs for tailoring the fiber structure and low-loss coupling with the conventional fibers were realized.
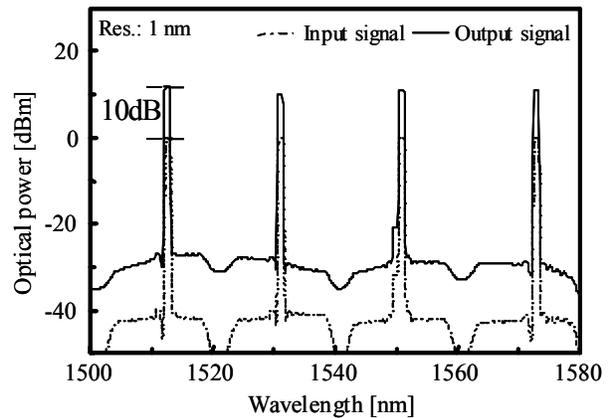

Fig. 5 CWDM signals observed at the input and the output of FRA

Table 2 Power penalty of CWDM system experiment with FRA

SMF		Signal Wavelength [nm]	Power Penalty [dB]	
Length[km]	Loss[dB]		with FRA	without FRA
100	20	1511	0.8	1.2
		1531	0.4	0.6
		1551	1.2	1.8
		1571	1.0	1.5
150	30	1511	1.6	——
		1531	0.9	——
		1551	1.8	——
		1571	1.8	——

Output signal power of FRA: +10dBm/ch

7. References

[1] K. Kakui, "Highly nonlinear fibers and their application to discrete Raman Amplification", Tech. Digest OAA2003, MC1(2003).
[2] S. Radic and C. J. Mckinstrie, "Recent progress in optical parametric amplifiers", Tech. Digest OAA2003, WD1(2003).
[3] S. Watanabe, S. Takeda and T. Chikama, "Interband wavelength conversion of 320Gb/s(32*10Gb/s) WDM signal using a polarization-insensitive fiber four-wave mixer", Technical Digest ECOC '98, pp.85-87(1998).
[4] T. Okuno, M. Onishi, and M. Nishimura, "Generation of ultra-broad-band supercontinuum by dispersion-flattened and decreasing fiber", IEEE Photon. Technol. Lett., vol.10, pp.72-74 (1998).
[5] S. Watanabe and F. Futami, "Optical signal processing with nonlinear fibers", Tech. Digest OFC2003, TuQ1(2003).
[6] K. Igarashi, H. Tobioka, S. Takasaka, S. Matsushita, S. Namiki, "Duration-tunable 100-GHz sub-picosecond soliton train generation through adiabatic Raman amplification in conjunction with soliton reshaping", Tech. Digest OFC2003, TuB6(2003).
[7] M. Onishi, T. Okuno, T. Kashiwada, S. Ishikawa, N. Akasaka and M. Nishimura, "Highly nonlinear dispersion-shifted fibers and their application to broadband wavelength converter", Optical Fiber Technology, vol.4, pp.204-214(1998).
[8] T. Miyamoto, M. Tanaka, J. Kobayashi, T. Tsuzaki, T. Okuno, M. Kakui and M. Shigematsu, "Transmission characteristics of highly-nonlinear-fiber-based Raman amplifier for CWDM systems", Technical digest OAA2003, TuAa5(2003).

Continuous Wave Fiber Parametric Amplifier with 41.5nm of Flat Gain

S. Radic, C. J. McKinstrie, R. M. Jopson and J. C. Centanni

Bell Laboratories, Lucent Technologies
791 Holmdel-Keyport Rd. R-231, Holmdel, NJ 07733
tel: 732-888-7115, fax: 732-888-7074, radic@lucent.com

Abstract:

Record performance of parametric fiber amplifier is reported. Continuous-wave, optical gain was measured over 41.5nm. Equalized gain was achieved in two-pump architecture without gain flattening elements. Maximal operating bandwidth was limited by fiber dispersion fluctuations.

OCIS Codes: 060.0060, 060.2320, 060.4370

1. Introduction:

Low-dispersion, high-confinement optical fiber is characterized by nonlinear parameter (γ) in excess of $10\text{km}^{-1}\text{W}^{-1}$. Continuous wave (CW) parametric gain exceeding[1] 40dB and 20nm bandwidth[2] has been reported recently. Strong parametric interaction was also used for all-optical processing operations, including regeneration[3] and optical demultiplexing[4]. High-confinement optical fiber is also referred to as highly nonlinear fiber (HNLF), a somewhat misleading appellation since the waveguide only provides high confinement with moderate enhancement of the material nonlinearity. Typical parameters include an effective area, $A_{eff} \sim 10\mu\text{m}^2$, that is almost an order of magnitude smaller than that of a standard single mode fiber (SMF) and considerably lower dispersion slope ($0.02\text{ps/nm}^2\text{km}$). An efficient parametric amplifier (PA) can be constructed using hundreds of meters of HNLF and optical powers compatible with commercially available semiconductor pumps. A PA potentially offers wideband amplification anywhere within the optical transmission window and provides means for highly efficient wavelength conversion and optical regeneration as well. The introduction of two-pump[6] PA's offers the possibility of wide-band, equalized, polarization independent gain. CW operation of a two-pump PA recently provided[2] a 22-nm bandwidth of equalized gain using a combined pump power of 600 mW. Both one- and two-pump PA bandwidth is critically limited by the HNLF properties. An ideal HNLF combines a high confinement factor ($1/A_{eff}$) with a small higher-order chromatic dispersion and low polarization-mode dispersion (PMD). Both the small effective area and the high-index profile, required to achieve high optical confinement, typically lead to considerable dispersion fluctuation along the fiber length. This remains one of the most difficult impairments to overcome in wideband PA design.

Here, we report on record CW parametric gain achieved using a two-pump parametric design. Described results exceed recently reported PA performance[5], and represent, to the best of our knowledge, first equalized performance exceeding 40nm.
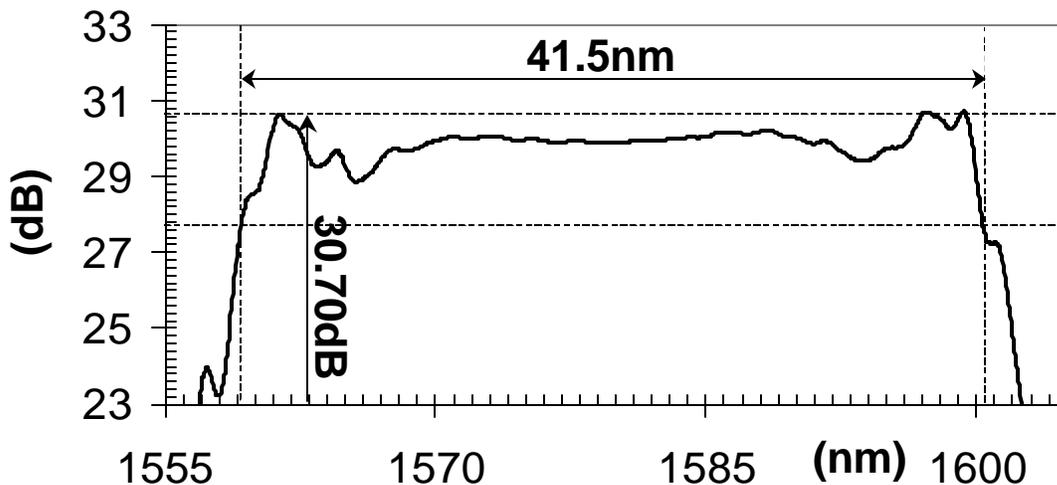

Figure 1: Equalized (3-dB bandwidth) parametric gain using 500m-long HNLF section and two-pump PA design.

2. Experiment:

The two-pump PA was constructed using C-Band (1553.5nm) and L-Band (1607nm) pumps, originating in tunable external cavity lasers. The initially narrowband pump light was broadened using phase modulators (PM) driven by 2^{31}-1 pseudorandom bit sequences at 10Gb/s in order to suppress stimulated Brillouin scattering (SBS) in dedicated high-power optical amplifiers and the HNLF. Optical filters having a 0.6nm bandwidth were used to reject amplified spontaneous emission (ASE) generated by booster amplifiers and provided a pump/ASE spectral contrast of 80 dB (measured within 0.1nm) prior to insertion into the HNLF. The pumps were combined in a L/C bandsplitter with maximal 0.8dB insertion loss. External-cavity laser provided a tunable signal that was combined with the pumps through the higher-loss input of a 10/90 coupler. Polarization controllers were used to adjust the pump polarization states at the input of the HNLF. The polarization of the pumps was monitored by tapping off 10% of the light prior to entry into the HNLF. Additional polarization splitters and a polarization beam splitter (PBS) were used to monitor relative pump-pump and pump-signal polarization states with two optical spectrum analyzers. Polarization controller at the input oh HNLF was used to investigate polarization dependent loss of the PA by changing both pump polarization states simultaneously while maintaining their relative polarization. Third optical spectrum analyzer monitored the onset of the SBS threshold. Significant SBS was not observed for the maximal pump power (480mW) used in the experiments described here. Figure 1 illustrates record bandwidth achieved by dual-pump operation of 500m-long HNLF segment characterized by the effective area of $11\mu m^2$, PMD parameter 0.04ps/km$^{-1/2}$ and zero-dispersion wavelength of 1579nm. Dispersion slope was 0.02ps/nm^2 and zero-dispersion wavelength was 1579nm. Pumps were copolarized and operated at 480mW (C-Band) and 275mW (L-Band).
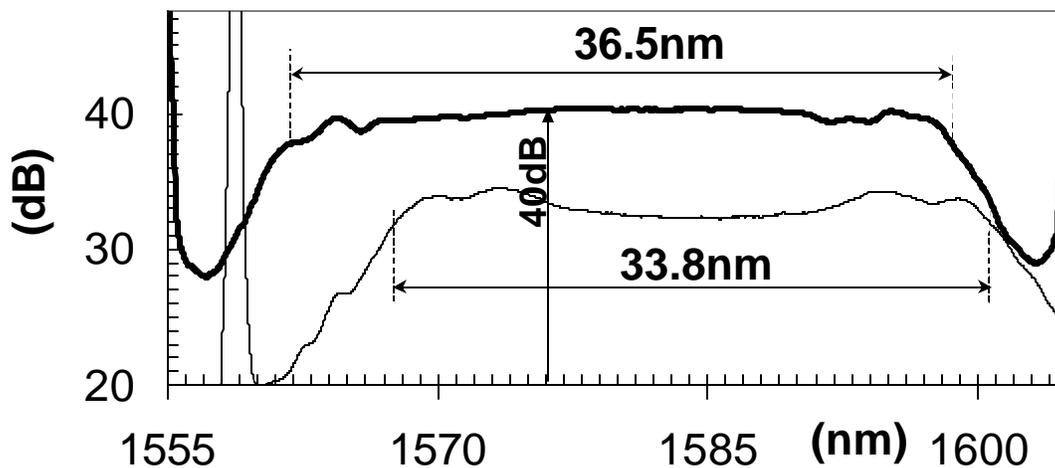

Figure 2: CW performance achieved using nearly identical 1km-long HNLF sections. Heavy curve corresponds to HNLF section with λ_0 = 1578nm, while thin curve indicates HNLF with λ_0 = 1583.5nm. Latter curve downshifted for 5dB for clarity.

Fig. 2 illustrates performance of longer (1km) HNLF segments characterized by nearly identical parameters: A_{eff} = $11\mu m^2$, PMD of 0.02ps/km$^{-1/2}$ and dispersion slope 0.02ps/nm^2. Zero-dispersion wavelengths were measured at 1578 and 1583.5nm, representing the only varying parameter between the two coils. Both HNLF sections were pumped using C-Band pump power of 200 and L-Band pump power of 600mW, respectively. Pumps were tuned for equalized performance at 1553.3/1607nm (λ_0 = 1578nm) and 1559/1610.7nm (λ_0 =1583.5nm). While average gain associated with 1km-long HNLF designs proves to be higher that that of a 500m-long PA, their 3-dB bandwidth falls considerably short of 40nm.

Parametric gain was also measured in case of cross-polarized pumps for all-three HNLF segments. Orthogonally pumped PAs have similar equalized gain, with the absolute gain decrease of approximately 10-14 dB, with respect to that of the copolarized launch state. PA gain was measured for a low-power input signal (Pin = -27dBm) over the spectral band lying between the pumps (1553-1610nm). All three PA exhibited high wavelength conversion efficiency, with measured idler power in the corresponding bandwidth within +/-1.4dB of the amplified signal power.
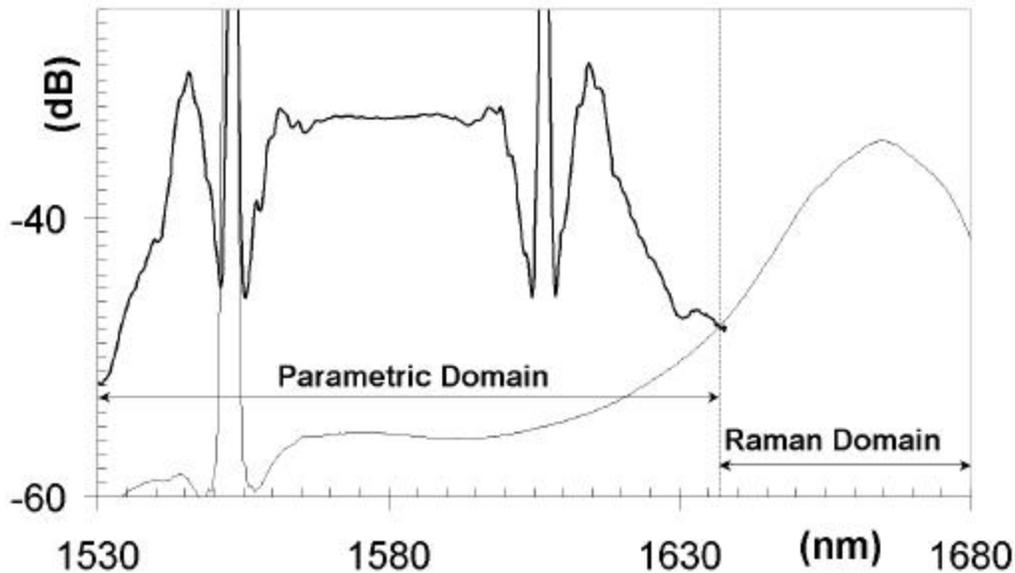
Figure 3: Domains of significant parametric (heavy curve) and Raman (thin curve) are well separated.

Finally, a new set of measurements was performed in order to separate contributions of Raman and parametric interactions, illustrated in Fig. 3. C-Band pump (1553.5nm) was operated in absence of L-Band higher (900mW) than in two-pump operating regime. Raman-shifted gain, indicated by the thin curve, peaked at 1667nm, approximately 113.5nm away from the pump wavelength. It is important to note that observed ASE generation, and, consequently, the small-signal Raman gain, is artificially high, and is not expected to be reached for any of the considered PA operating regimes. Simultaneous C/L-Band pump operation guarantees a significant (1.6-3dB in measured cases) pump-to-pump power transfer, significantly reducing Raman ASE generation in regions close to any of the four parametric bands.

3. Conclusion:

In conclusion, we have demonstrated record equalized fiber parametric amplifier performance characterized by a 41.5 nm bandwidth and 30 dB of CW gain and wavelength conversion efficiency by using short HNLF section and dual-pumping architecture. The measured performance represents the first report on a flat CW parametric gain exceeding the bandwidth of both C-Band (32nm) and L-Band (39nm) EDFA. Higher CW gain (40dB) was demonstrated at reduced bandwidth (36.5nm) using longer (1km) HNLF segment. The bandwidth was limited by the fluctuations in HNLF dispersion, as demonstrated by measurements in long HNLF segments with otherwise identical global characteristics. We believe that the highly nonlinear fiber offers the promise of even wider parametric gain, provided optimal combination of pumping power, HNLF interaction length and sufficient control of its dispersion parameters.

References:
1) J. Hansryd and P. Andrekson, "Broad-Band Continous-Wave-Pumped Fiber Optical PA with 49-dB Gain and Wavelength Conversion Efficiency," IEEE Photon. Technol. Lett. Vol. 13, p.194, 2001.
2) S. Radic, C. J. McKinstrie, A. R. Chraplyvy, G. Raybon, J. C. Centanni, C. G. Jorgensen, K. Brar and C. Headley, "Continuous Wave Parametric Gain Synthesis Using Nondegenerate-Pump Four-Wave Mixing," IEEE Photonics Technol. Lett., Vol. 14. p. 1406., 2002.
3) S. Radic, C. J. McKinstrie, R. M. Jopson, J. C. Centanni, A. R. Chraplyvy, "All-Optical Regeneration in One- and Two-Pump PA Using HNLF," IEEE Photon. Technol. Lett., Vol. 15, pp. 957, 2003.
4) J. Hansryd and P. Andrekson, "O-TDM Demultiplexer with 40-dB Gain Based on a Fiber Optical Parametric Amplifier," IEEE Photon. Technol. Lett. Vol. 13, p.732, 2001.
5) S. Radic, C. J. McKinstrie, R. M. Jopson, J. C. Centanni, Q. Lin and G. P. Agrawal, "Record Performance of a Parametric Amplifier Constructed with HNLF," IEE Electron. Lett., V. 39, p. 838, 2003.
6) C. J. McKinstrie, S. Radic and A. Chraplyvy, "Parametric amplifiers driven by two pump waves", IEEE Sel. Top. Quantum Electron. 8, p. 538, 2002.

Loss-induced parametric amplification in optical fiber

Takuo Tanemura, Yasuyuki Ozeki, and Kazuro Kikuchi

Research Center for Advanced Science and Technology, University of Tokyo, 4-6-1 Komaba, Meguro-Ku, Tokyo 153-8904, Japan
tanemura@ginjo.rcast.u-tokyo.ac.jp

Abstract: We find both experimentally and theoretically that when the idler wave experiences large distributed loss relative to the signal wave, parametric gain arises in the normal dispersion regime of an optical fiber.
OCIS codes: (190.4970) Parametric oscillators and amplifiers; (060.4370) Nonlinear optics, fibers; (190.4410) Nonlinear optics, parametric processes;

1. Introduction

Fiber-based optical parametric amplification (OPA) is a promising candidate for realizing potentially broadband and noiseless amplifiers [1,2]. The single-pump OPA process is explained alternatively as modulational instability (MI) [1,3], in which small perturbation of the pump wave grows exponentially along the fiber. When a CW pump propagates with a weak perturbation, AM component of the perturbation converts to the PM component through the optical Kerr effect. At the same time, the PM component is transferred back to the AM component by the group-velocity dispersion (GVD) of the fiber. When GVD is negative, these effects provide positive feedback, resulting in MI. In the normal dispersion regime, therefore, pump remains modulationally stable and OPA is strictly inhibited.

Generally speaking, PM-to-AM conversion occurs also when there is wavelength-dependent loss in the fiber. It is, therefore, not surprising if there exists a novel type of MI that arises through the loss dispersion instead of GVD. As a specific case of interest, we consider a single-pump OPA process where the idler wave experiences large distributed loss compared to the signal wave as illustrated in Fig. 1. For the first time to our knowledge, we show both experimentally and theoretically that large OPA gain is induced in the normal GVD regime of the fiber when appropriate loss is applied to the idler wave.
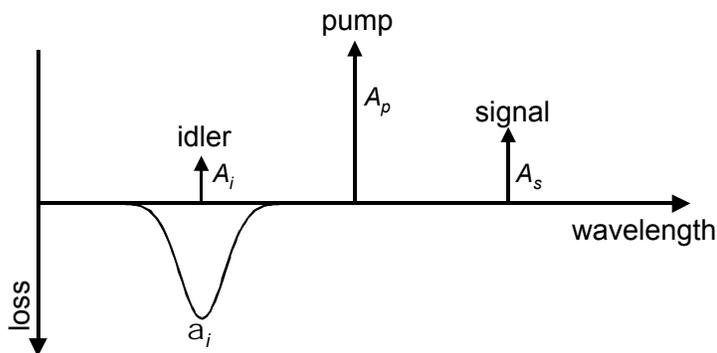

Fig. 1. Single-pump OPA configuration considered in this paper, where the fiber has large distributed loss at the idler wavelength.

2. Experiment

Fig. 2 shows our experimental setup to demonstrate the loss-induced OPA. We exploited stimulated Brillouin scattering (SBS) to realize wavelength-selective loss at the idler wavelength [4]. The OPA pump and signal waves were generated by two external cavity lasers, ECL1 and ECL2, tuned at 1544.7 and 1546.7 nm, respectively. After combined by a 1:9 directional coupler (DC), they were modulated with square pulses using an electro-absorptive modulator (EAM). The modulated pulses had a flat top of 0.81 ns, the full width at the half maximum (FWHM) of 1.7 ns, and the repetition rate of 5 MHz. The waves were then amplified by an erbium-doped fiber amplifier

(EDFA) and launched on a 1-km-long highly nonlinear dispersion-shifted fiber (HNL-DSF) with the zero-dispersion wavelength at 1561.2 nm, dispersion slope of 0.027 ps/km/nm^2, nonlinear coefficient γ of 20 /km/W, and the total loss of 1.4 dB. The peak powers of the pump and signal pulses were 770 mW and 0.1 mW at the input of HNL-DSF, respectively. Note that the pump wave was located in the normal GVD regime (–0.45 ps/km/nm), so that standard OPA was inhibited due to the large phase mismatch.

We then injected a SBS pump wave from the opposite side of HNL-DSF. The wavelength of the SBS pump was set longer than the idler wave by the Brillouin frequency (9.5 GHz), so that it induced narrowband anti-Stokes absorption at the idler wavelength. Note that the SBS pump wave was phase-modulated with a specially coded binary pattern at 3.5 Gb/s [4], which broadened the absorption spectrum uniformly to approximately 2.5 GHz, covering the entire idler bandwidth (< 1 GHz).
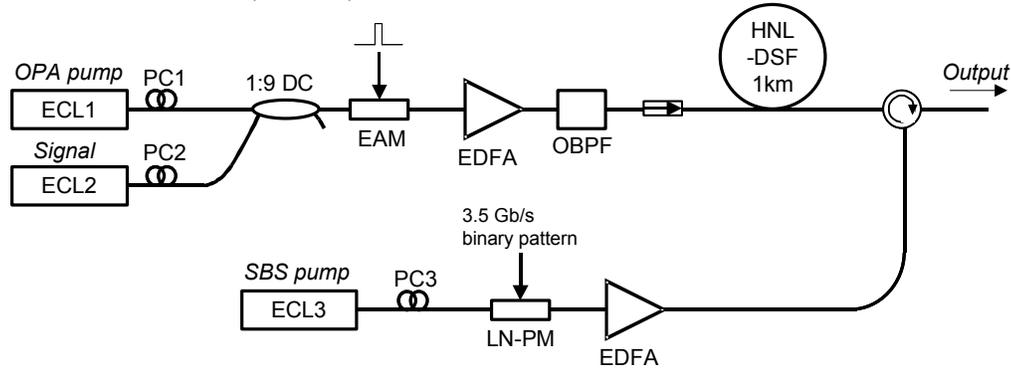

Fig. 2. Experimental setup to demonstrate the loss-induced OPA. PC: polarization controller, OBPF: optical bandpass filter, LN-PM: LiNbO$_3$ phase modulator

The dots in Fig. 3 show the on-off signal gain measured as a function of the idler loss. The on-off signal gain is defined as the output signal power when the OPA pump is turned on relative to that without the pump. The idler loss was varied by changing the incident power of the SBS pump. From Fig. 3, we see clearly that the signal gain increases as we increase the idler loss.
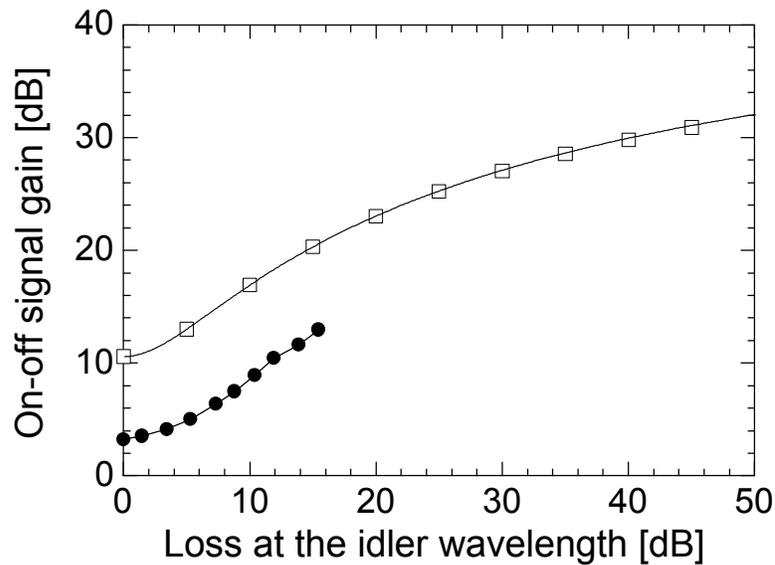

Fig. 3. On-off signal gain measured as a function of the idler loss (dots). The results of analytical calculation (Eq. (3)) (solid line) and the split-step Fourier simulation (squares) are also shown.

3. Theory and Discussion

To examine the validity of the above results, we calculate the signal gain analytically. Under the undepleted pump

approximation, the coupled mode equations of the signal and idler waves are written as

$$\frac{dA_s}{dz} = i g P \left(2A_s + A_i^* e^{-i(\Delta k - 2gP)z} \right) \ , \tag{1}$$

$$\frac{dA_i}{dz} = i g P \left(2A_i + A_s^* e^{-i(\Delta k - 2gP)z} \right) - \frac{1}{2}a_i A_i \ , \tag{2}$$

where A_s and A_i are the slowly varying envelopes of the signal and idler waves, P is the pump power, and $\Delta k \equiv k_s + k_i - 2k_p$ is the linear phase-mismatching factor [1]. The term $a_i A_i / 2$ represents the idler absorption, whereas the background fiber loss is neglected. Assuming the boundary condition of $A_s(0) = \sqrt{P_{s0}}$ and $A_i(0) = 0$, Eqs. (1) and (2) can be solved rigorously and the signal power $P_s(z)$ is expressed as

$$P_s(z) = P_{s0} e^{-a_i z / 2} \left[(g^2 + f^2 + a_i^2/4 + k^2) \cosh(gz) + (ga_i + 2fk)\sinh(gz) \right.$$

$$\left. + (g^2 + f^2 - a_i^2/4 - k^2)\cos(fz) + (fa_i - 2gk)\sin(fz) \right], \tag{3}$$

where

$$g = \frac{1}{\sqrt{2}} \left\{ \left[a_i^4/16 + \left(k^2 + 4g^2 P^2 \right) a_i^2/2 + \left(k^2 - 4g^2 P^2 \right)^2 \right]^{1/2} + a_i^2/4 - \left(k^2 - 4g^2 P^2 \right) \right\}^{1/2}, \tag{4}$$

$$f = \frac{\operatorname{sgn}(a_i k)}{\sqrt{2}} \left\{ \left[a_i^4/16 + \left(k^2 + 4g^2 P^2 \right) a_i^2/2 + \left(k^2 - 4g^2 P^2 \right)^2 \right]^{1/2} - a_i^2/4 + \left(k^2 - 4g^2 P^2 \right) \right\}^{1/2}, \tag{5}$$

$$k = \Delta k + 2gP. \tag{6}$$

We calculate Eq. (3) with the parameters describing the above experiment. The result is shown in Fig. 3 by the solid line. Although we see some differences in the absolute values of the gain, the theory indicates the same qualitative property; the signal gain increases with the idler loss. The gain difference between the theory and experiment may be attributed to the longitudinal fluctuation of GVD along the fiber. We also calculate the signal gain by solving the nonlinear Schrödinger equation numerically using the split-step Fourier method [1], which shows an excellent agreement with the theory (squares in Fig. 3).

The underlying physics of the loss-induced OPA can be understood clearly if we perform the analysis in terms of MI. By transforming the variables A_s and A_i in Eqs. (1) and (2) to $a \equiv (A_s + A_i^*)$ and $p \equiv -i(A_s + A_i^*)$, we obtain coupled equations similar to those in [3], describing the power conversion between the AM (a) and PM (p) components of the perturbation. These equations directly reveal that the PM-to-AM conversion occurs through the loss dispersion in addition to the GVD. This may, in some cases, cooperate with the Kerr-induced AM-to-PM conversion to provide a positive feedback process, which is responsible for the exponential OPA gain observed in the above experiment. The detailed analysis will be presented elsewhere.

4. Conclusion

For the first time to our knowledge, we have demonstrated both experimentally and theoretically that by applying distributed loss to the idler wave, OPA gain is induced in a largely phase-mismatched regime of a fiber, where OPA is strictly inhibited otherwise. The underlying physics of this phenomenon is that the loss dispersion induces PM-to-AM conversion of the pump perturbation, which cooperates with the Kerr-induced AM-to-PM conversion to provide a positive feedback process, resulting in MI. Our results indicate a possibility of designing a new kind of OPA device which has a gain bandwidth beyond the standard "phase-matching regime". For example, broadband OPA may be realized by employing an unpumped EDFA or a long period fiber Bragg grating.

References
[1] G. P. Agrawal, *Nonlinear Fiber Optics* 2nd ed. (Academic, New York, 1995).
[2] J. Hansryd, P. A. Andrekson, M. Westlund, J. Li, and P. O. Hedekvist, "Fiber-based optical parametric amplifiers and their applications," IEEE JSTQE **8,** 506-520 (2002).
[3] A. Hasegawa and W. F. Brinkman, "Tunable coherent IR and FIR sources utilizing modulational instability," IEEE JQE **QE-16,** 694-697 (1980).
[4] T. Tanemura, Y. Takushima, and K. Kikuchi, "Narrowband optical filter, with a variable transmission spectrum, using stimulated Brillouin scattering in optical fiber," OL **27,** 1552-1554 (2002).

Wavelength conversion characteristics of highly efficient fiberoptic four-wave mixer for 160 GHz picosecond pulse train

K. Igarashi, H. Tobioka, S. Takasaka, R. Miyabe, J. Hiroishi, T. Yagi, O. Aso and S. Namiki

Fitel Photonics Laboratory, Furukawa Electric Co., Ltd.
6 Yawata-Kaigandori, Ichihara, Chiba 290-8555, Japan
TEL: +81-436-42-1724, FAX: +81-436-42-9340, e-mail: igarashi.koji@furukawa.co.jp

Abstract: We investigated wavelength conversion characteristics of 160 GHz pulse train in a wavelength converter based on four-wave mixing using highly nonlinear fiber. We observed modulation instability causes OSNR to degrade while conversion efficiency rapidly increases.

1. Introduction

All-optical signal processing based on fiber-optic four-wave mixing (FWM) is one of main techniques for ultra-high speed transmission system.[1,2] Desirable features of optical fiber as a nonlinear optical signal processing material are femtosecond response time of the Kerr effect and low loss over a wide band. In fact, it has been reported that FWM scheme is effective for the demultiplexing[3] and wavelength conversion[4] of ultra-high speed signal pulse over 100 Gbit/s. In addition, some have reported that the use of the optical parametric amplification in modulation instability regime is effective to improve the conversion efficiency and/or its flatness in such fiber-optic FWM.[5,6]

On the other hand, pulse shape could be distorted through nonlinear fiber propagation such as self- and/or cross-phase modulation (SPM/XPM) and group-velocity dispersion (GVD) effects. Especially, one should pay attention to the degradation of pulse train coherence due to anomalous dispersion fiber propagation.[7-9] For the fiber-optic-based signal processing, the above-mentioned superfluous effects should be suppressed whereas power conversion efficiency should be as high as possible. Even though a FWM-based wavelength converter is attractive because FWM can be generated without generating other adverse effects such as SPM, XPM and GVD,[4] the conversion efficiency was low (-16 dB) and detailed studies on wavelength conversion characteristics with respect to various launched powers have not been reported for ultra-fast pulse trains such as over 100 Gbit/s.

From such a viewpoint, we focus on pulse train characteristics in wavelength conversion based on fiber-optic FWM over a wide input power range up to 26 dBm at which the conversion efficiency becomes as high as -5 dB. We also experimentally investigate the relationship between the optical signal-to-noise ratio (OSNR) degradation and the conversion efficiency.

2. Experiment and results

Figure 1 shows an experimental setup of FWM-based wavelength conversion of 160 GHz picosecond pulse train. Low-noise 160 GHz 1.7 ps pump pulse train with 1556 nm[10] was coupled with a CW light with a wavelength of 1535 nm by WDM coupler and jointly launched into 0.2 km-long low-slope highly nonlinear fiber (LS-HNLF).[11] The converted pulse train was extracted from the LS-HNLF output light through a combination of a WDM coupler and a band-pass filter with a center wavelength and bandwidth of 1578 nm and 4.5 nm, respectively. The average power of the input pulse P_{pump} was adjusted by an
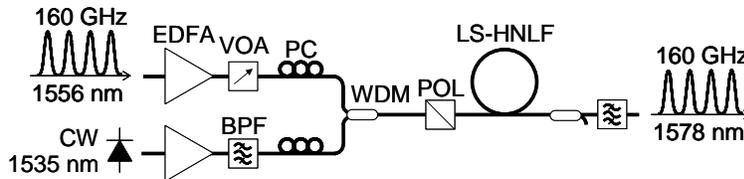

Fig. 1. Experimental setup of wavelength conversion of 160 GHz ps pulse train.

optical variable attenuator (VOA), and the CW power P_{CW} is fixed to 23 dBm. The LS-HNLF has a nonlinearity and dispersion slope of 24 1/W/km and 0.013 ps/nm^2/km, respectively.[11] Its zero dispersion wavelength is approximately 1546 nm, and its dispersion at the input pump pulse wavelength is anomalous.

The LS-HNLF input and output spectra were measured by a spectrum analyzer with a resolution bandwidth of 0.05 nm, as shown in Fig. 2. While the output pulse spectrum at P_{pump} = 19 dBm was not significantly distorted as indicated in Ref. 4, the spectral distortion in the case of P_{pump} of 26 dBm was remarkable and so was the spectral broadening. In addition, one should pay attention to an increase of noise component in 1.58 µm. Figure 3 shows the autocorrelation traces of the converted pulse trains after the BPF at P_{pump} of 19 dBm and 26 dBm. One can see that the converted pulse is simultaneously compressed during wavelength conversion.

The upper part of Fig. 4 plots an average power of the converted pulse train P_{conv} as function of P_{pump}. The dashed line and the dotted-dashed line indicate the quadratic and cubic curves of P_{pump}. P_{conv} grows up with the increase of P_{pump}, and its maximum reached 18 dBm corresponding to the conversion efficiency η of −5 dB at P_{pump} = 26 dBm. It is notable that experimental data is well plotted along the dotted-dashed
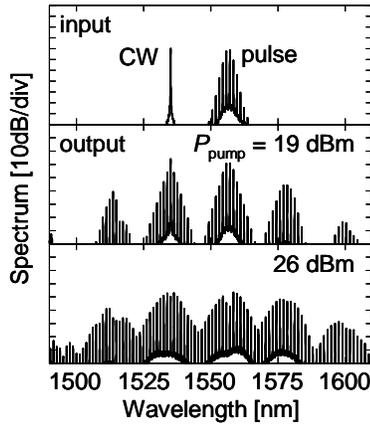

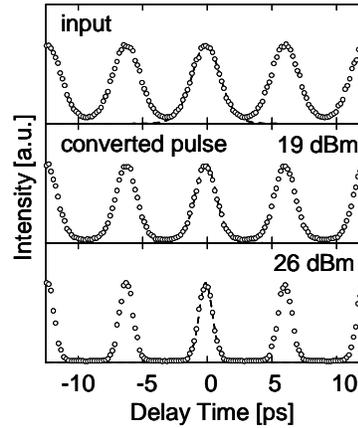Fig. 2. Optical Spectra of LS-HNLF input and output. P_{pump} is input pulse power.

Fig. 3. Autocorrelation traces of input and converted pulse trains. Number in upper right indicates input pulse power P_{pump}. Dashed lines are Gaussian shapes.
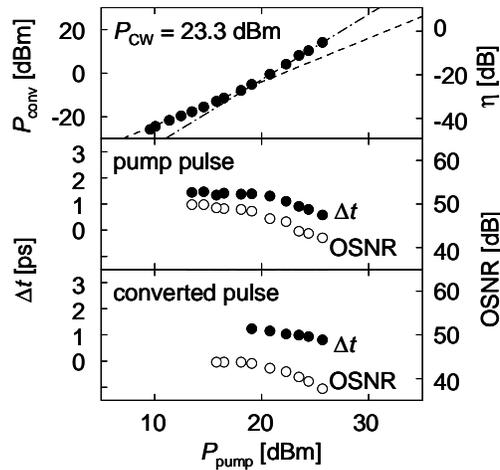

Fig. 4. Converted pulse power P_{conv} v.s. input pump pulse power P_{pump}, and dependence of temporal duration Δt and OSNR of converted pulse train on P_{pump}. η is conversion efficiency. P_{CW} is assisted CW power. Dashed line and dotted-dashed line in upper part indicate square and cubic, respectively.

line in the range that $P_{\mathrm{pump}} > 20$ dBm while the agreement with experimental data and the dashed line is good in the range that $P_{\mathrm{pump}} \leq 20$ dBm.

The center and lower parts of Fig. 4 plot the dependence of the characteristics of the pump pulse train and converted pulse train on P_{pump}, respectively. The closed and open dots are the temporal duration Δt and optical signal-to-noise ratio (OSNR), respectively. Here, the former was calculated based on the autocorrelated pulse shape, and the latter was measured from the ratio of the spectral peak of the signal to that of the noise using an optical spectrum analyzer. As for the pump pulse, the OSNR degradation is remarkable for $P_{\mathrm{pump}} > 20$ dBm as well as Δt reduces steeply. This is attributable to the pulse compression and the noise amplification originated from the higher-order soliton propagation because the pump pulse train with a high peak power was launched into the anomalous dispersion fiber.[7-9] Similarly, Δt of the converted pulse was reduced and its OSNR was improved for $P_{\mathrm{pump}} > 20$ dBm. It is suggested that the characteristics of the converted pulse train depends strongly on the nonlinear fiber propagation of the pump pulse train. However, in case of 26 dBm input at which OSNR is worst in the plot, the temporal shape of the converted pulse train is well maintained as shown in the bottom plot of Fig. 3, and the OSNR is still larger than 38 dB.

3. Conclusion

We achieved a conversion efficiency as high as −5dB in FWM-based wavelength converter of a 160 GHz picosecond pulse train using a LS-HNLF. We also investigated the relationship between the OSNR degradation and the wavelength conversion efficiency of the FWM scheme in the LS-HNLF. We observed that modulation instability causes the conversion efficiency to rapidly increase, converted pulse to be temporally compressed, and OSNR to degrade. These results suggest that there may be an optimum operating condition in which sufficient conversion efficiency is achieved while a good pulse quality such as OSNR and pulse shape is maintained.

References

[1] S. Watanabe *et al.*, *OFC2003*, PD16-1 (2003).
[2] F. Futami *et al.*, *OAA2003*, MD07, 82 (2003).
[3] T. Morioka et al., Electron. Lett., 32, 833 (1996).
[4] H. Tobioka *et al.*, *to be presented in ECOC2003*, We.3.7.1 (2003).
[5] T. Yamamoto and M. Nakazawa, *Photon. Technol. Lett.*, 9, 327 (1997).
[6] O. Aso *et al.*, *OFC2000*, ThL6 (2000).
[7] H. Kubota *et al.*, *J. Opt. Soc. Amer. B*, 16, 2223 (1999).
[8] K. Igarashi *et al.*, *OAA2003*, MD02, 67 (2003).
[9] T. Inoue and S. Namiki, *to be presented in ECOC2003*, We.4.P.14 (2003).
[10] K. Igarashi *et al.*, *CLEO2003*, CMH7 (2003).
[11] J. Hiroishi *et al*, *ECOC2002*, PD-1.5 (2002).

All Optical Shutter Based on Raman-Assisted Four-wave Mixing in dispersion shifted fiber

Lixin Xu,[1] P. K. A. Wai,[1] H. Y. Tam,[3] L. F. K. Lui,[1] and M. S. Demokan[3]

[1]Photonics Research Centre and Department of Electronic and Information Engineering,

The Hong Kong Polytechnic University, Hung Hom, Hong Kong

Phone: +852 2766-6231, fax: +852 2362-8439, email: enwai@polyu.edu.hk

[2]Department of Physics, University of Science and Technology of China, Hefei, 230026, China

[3]Photonics Research Centre and Department of Electrical Engineering,

The Hong Kong Polytechnic University, Hung Hom, Hong Kong

Abstract: We demonstrated a 10 Gb/s all-optical shutter based on Raman-assisted four-wave-mixing in dispersion-shifted fiber. Improvement of more than 65 dB in the conversion efficiency and 26 dB in the signal-to-background ratio are obtained.

©2003 Optical Society of America

OCIS codes: (230.1150) All-optical devices; (190.4380) Nonlinear optics, four-wave mixing

1. Introduction

Optical networks utilizing fast packet switching are expected to provide the required capacities and flexibility in the next-generation high-speed networks [1-2]. Ultra fast demultiplexing based on four-wave mixing (FWM) have been demonstrated in optical fibers [3]. Low efficiency and relatively narrow parametric bandwidth, however, limit its usefulness. A number of methods, including spectral spreading technique and combination of both parametric and Raman amplifications have been proposed to address this problem [2, 4].

In this paper, we propose an all optical shutter based on Raman-assisted four-wave mixing, which uses Raman amplifiers to assist degenerate four-wave mixing in dispersion-shifted fiber to enhance the conversion efficiency and parametric bandwidth. There is no need to increase the input pump power or to spread the pump spectrum. Our results show that the conversion efficiency is improved by more than 65 dB and the signal-to-background ratio (SBR) by more than 26 dB when compared that to that of four-wave mixing without the Raman amplifiers. We observed that the shutter has an extra fast response time and high ON/OFF switching ratio.

2. Results and discussion

Figure 1 shows the experimental setup of the all optical shutter based on Raman-assisted four-wave mixing. The 10 Gbits/s non-return-to-zero data signal at 1551.72 nm was generated by external modulation (Mod1) of a DFB laser with the power (measured at the port 1 of the circulator) of –6.7 dBm. The shutter signal was generated from a tunable laser (wavelength set at 1552.52 nm) by another modulator (Mod 2). The power of the shutter signal, measured at the port 1 of the circulator, was –6.4 dBm. The maximum

efficiency of degenerate FWM signal occurs at a wavelength detune of 0.4 nm for a Raman pump power of 1.1 W. In order to test the application of this method in DWDM system, the wavelength separation between data signal and shutter signal was set at the 0.8 nm wavelength grid specified by International Telecommunication Union (ITU) Recommendations. Therefore, the new generated wavelengths were also spaced at multiple of ITU grid spacing of 0.8 nm. The data signal and shutter signal were combined with the 8-channel DWDM multiplexer of 0.8 nm wavelength grid after passing through polarization controllers PC3 and PC4 respectively. The combined signals were then launched into a 12-km dispersion-shifted fiber (DSF) (zero dispersion wavelength is 1547.5nm) through a circulator. The Raman pump at 1455 nm is coupled into the DSF through the 1455/1550nm WDM coupler in the counter-propagating direction. The available maximum Raman pump power at the input port of the DSF is about 1.3 W. The new generated signals were obtained from the 1550 nm output port of the 1455/1550nm WDM coupler and sent to the optical spectrum analyzer and the 50 GHz oscilloscope for spectrum and time domain analysis, respectively.

  Figure 2 shows the output spectra of the FWM signals when the Raman pump powers are 0 W and 1.1 W respectively. More than two new wavelengths are generated by Raman-assisted degenerate FWM because the powers of the newly generated wavelengths are sufficiently high (can be higher than 10 dBm in some cases) to produce additional FWM signals with the input wavelengths or with each other. That is to say, more than two wavelengths carry the same switched out data simultaneously. These wavelengths were spaced at multiples of ITU grid spacing of 0.8 nm. From Fig. 2, the use of Raman pump improved the conversion efficiency at the generating wavelength 1553.32 nm by 65.55 dB and the signal-to-background ratio (SBR) by 26.6 dB when compared to that without Raman pump.

  Figures 3(a) and (b) depict the timing diagrams of the data signal and the control signal. The data is 10 Gb/s NRZ signal with a data length 1280 bits. Both the ON and OFF states of the control signal have a duration of 130 ns. Only those data signals located within the ON state of the control signal will be wavelength-converted by FWM, otherwise the data signal will not be wavelength-converted. Figure 3(c) shows the timing diagram of the switched data signal at 1553.32 nm. The noise level is relatively low showing a high extinction ratio for the switched data. Figure 4a – c show the details of the switching action by the proposed shutters. Figure 4c shows no pattern dependent effect on the switched data. We observed that there is no significantly delay effect in switching by comparing the falling edges of the switched signal in Fig.4c and that of the control signal in Fig. 4b. Therefore, the proposed all-optical switching scheme may operate at bit rates beyond 10 Gbits/s. Figure 4(d) shows the eye diagrams of the input data signal (on the left side) and switched data signal (on the right side) at 1553.32 nm. Clear eye opening of is observed.

3. Conclusion

  We proposed and demonstrated an all-optical shutter which uses a Raman amplifier to enhance the conversion efficiency and parametric bandwidth of degenerate four-wave mixing in dispersion-shifted fiber. Our results show that the conversion efficiency and the signal-to-background ratio (SBR) were improved by more than 65 dB and 26 dB, respectively, when compared to the case of four-wave mixing without Raman assist. The shutter demonstrates an ultra fast response time and high ON/OFF switching ratio. The shutter may operate at bit rate beyond 10 Gbits/s in a more efficient way than conventional methods.

4. Acknowledgment

5. References

[1] L. Y. Chan, P. K. A. Wai, L. F. K. Lui, et al., "*Demonstration of an all-optical switch by use of a multiwavelength mutual injection-locked laser diod*", Opt. Lett., **28**, 837-839 (2003).

[2] P.O. Hedekvist and P.A. Andrekson, " *Demonstration of fibre four-wave mixing optical demultiplexing with 19dB parametric amplification*", Electron. Lett., **32**, 830-831 (1996).

[3] T. Morioka, S. Kawanishi, K.Uchiyama, et al., "*Polarisation-independent 100 Gbit/s all-optical demultiplexer using four-wave mixing in a polarisation-maintaining fibre loop"*, Electron. Lett., **30**, 591-592 (1994).

[4] K. Kikuchi and C. Lorattanasane, "*Design of highly efficient four-wave mixing devices using optical fibers",* Photon. Technol. Lett.,. **6**, 992 (1994).
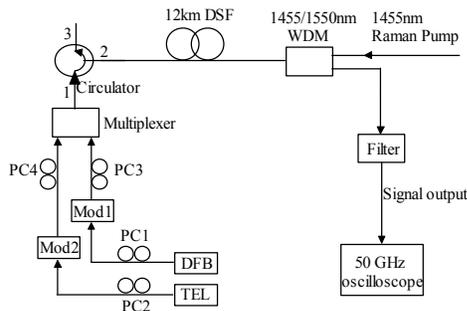
Fig. 1. The experimental setup of Raman-assisted FWM.

Fig. 3. Timing diagrams for (a) the 10 Gb/s NRZ data signal, (b) the synchronized control signal with pulse duration of 130 ns period, (c) the switched 10 Gbits/s data signal at 1553.32 nm The time scale is 50 ns/div.
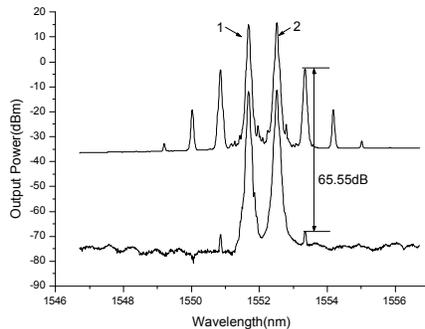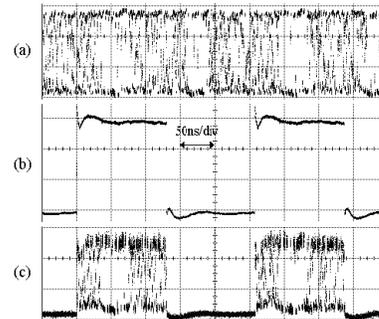

Fig. 2. The output spectra of the FWM signals with (top curve) and without (bottom curve) the Raman pump. The Raman power for the top curve is 1.1 W. The input data signal and the control signal are labeled '1' and '2', respectively.
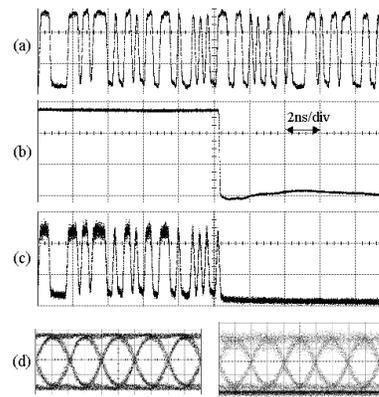

Fig. 4. (a) – (c) Same as Figure 3 but the time scale is 2 ns/div, (d) eye diagrams of the input data signal (left) and switched data signal at 1553.32 nm (right). The time scale is 50 ps/div.

A novel electrically tuned all-fiber comb filter

Qun Li, Chien-Hung Lin and Henry P. Lee

Dept. of EECS, Henry Samueli School of Engineering, University of California, Irvine CA 92697
qli@ece.uci.edu

Abstract: We demonstrated an all-fiber comb filter having an extinction ratio of ~20dB using a two-mode fiber. Full free spectral range wavelength tuning is achieved using a thin film micro-heater directly deposited on the fiber.
©2003 Optical Society of America

1. Introduction

Optical comb filters can be used as multi-channel isolation filters for wavelength-division-multiplexing (WDM) systems or as wavelength selective filters for multi-wavelength laser sources. Optical comb filters have been previously realized using Fabry-Perot etalons [1], Mach-Zehnder interferometers [2], Sagnac birefringence filter [3] and long-period fiber gratings [4]. In this paper, we present a new, easy-to-fabricate all-fiber electrically tuned optical comb filter based on the interference effect in a two-mode fiber (TMF). The comb filter exhibits an overall insertion loss of 2dB, an extinction ratio of ~20dB, negligible polarization dependent loss (PDL), < -40dB back reflection and full free spectral range (FSR) wavelength tunability using a thin film micro-heater with a tuning efficiency of ~7.5nm/W.

2. Operation Principle

The interference between fundamental and higher order modes (HOM) has been previously used to characterize the performance of a HOM fiber based dispersion compensator [5]. However, when a SMF is spliced with conventional step-index TMF, most of the optical power (about 90%) is coupled to the fundamental mode of the TMF, resulting in a low extinction ratio for the interference effect. In this paper, we use a dispersion compensating fiber (DCF) with a large dispersion parameter (-300ps/nm/km) from Sumitomo as the TMF [6]. The fiber has a small core size and exhibits a single-mode cutoff wavelength near 1550nm. When fusion spliced to standard SMF under optimized conditions, it was found that near equal coupling is obtained to each of the two modes.

The comb filter has a simple design and operates like a fiber Mach-Zehnder interferometer. A section of TMF is spliced between two SMF pigtails. Owing to the modal mismatch between the two fibers, the LP_{01} mode of the SMF is converted into LP_{01}, LP_{02} and radiation modes of the TMF at the first splicing point: $\left| LP_{01} \right\rangle \Rightarrow a \left| LP_{01} \right\rangle + b \left| LP_{02} \right\rangle + c \left| \Lambda \right\rangle$, where $a^2 + b^2 + c^2 = 1$. The ratio between LP_{01} and LP_{02} modes (a: b) can be partially controlled by the splicing parameters. When the arc time is sufficiently long, a more tapered transition of index profile can be formed between the two fibers, and the coupling ratio can be made almost 1:1. This is verified by the measured filtering spectrum. At the second splicing point, the radiation modes disappear due to propagation loss. The modes in the TMF can be represented as $ae^{-j\beta_{01}L} \left| LP_{01} \right\rangle + be^{-j\beta_{02}L} \left| LP_{02} \right\rangle$, where L is the length of the TMF, $\beta_{01} = \frac{2\pi}{\lambda} n_{01}$ and $\beta_{02} = \frac{2\pi}{\lambda} n_{02}$ are the propagation constants of LP_{01} and LP_{02} modes, respectively, and n_{01} and n_{02} are the effective indices of the corresponding modes. After these two modes are converted back into the SMF at the second splicing point, the optical power becomes:

$$a^4 + b^4 + 2a^2b^2 \cos((\beta_{01} - \beta_{02})L) = a^4 + b^4 + 2a^2b^2 \cos(\frac{2\pi}{\lambda}(n_{01} - n_{02})L) \cdot$$

We can see that the transmitted optical power is a periodic function of wavelength. Neglecting the dispersion of n_{01} and n_{02}, the period of the filter is determined by $\Delta\lambda = \frac{L_B}{L}\lambda$, where L_B is the beat length and is equal to $\frac{2\pi}{\beta_{01} - \beta_{02}}$.

3. Experimental Results and Discussions

We first study the characteristics of the comb filter by varying the length of the TMF and the arc time used for splicing between the SMF and the TMF. The spectrum of the comb filter is measured using a broadband LED light source and optical spectrum analyzer.
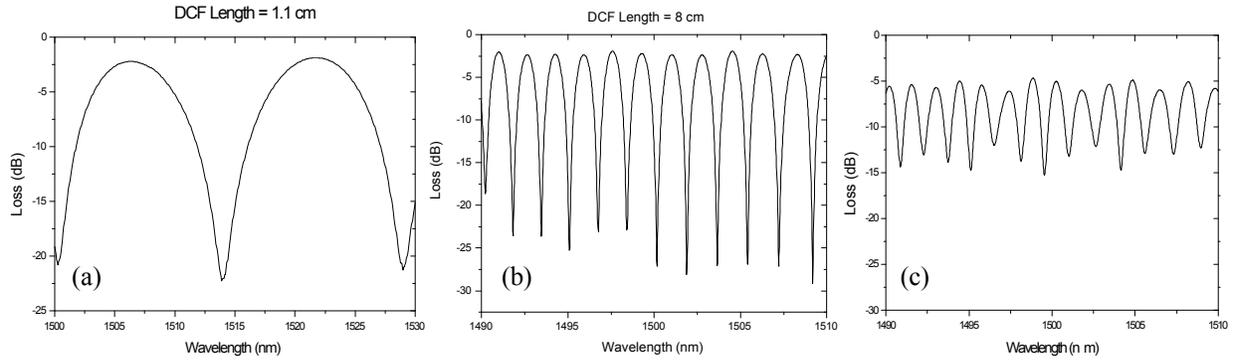
Fig. 1: (a) and (b) Filtering spectra of the comb filter with different TMF lengths; (c) Filter response when a non-optimized shorter arc time is used.

Fig. 1 (a) and (b) show the filtering spectra of the comb filter for L of 11mm and 80mm, respectively. The measured periods of the combs are 13.8nm and 1.72nm, respectively. From these data, L_B of the TMF is estimated to be about 100μm. The high extinction ratio of the comb filter (~20dB) indicates that the coupling to LP_{01} and LP_{02} modes are nearly identical. We attribute this high extinction ratio to the large modal mismatch between the SMF and the DCF, since they have significantly different index profiles and modal sizes. The insertion loss of the device is around 2dB due to excitation of radiation modes at both spliced spots. The back reflection of the device is measured to be less than –40dB using a circulator. The PDL of the filter is also measured by cascading the LED with a broadband fiber polarizer and a polarization controller (PC). The device shows nearly zero PDL since only symmetrical modes are involved in the mode conversion. The spectrum shown in **Fig. 1** (a) and (b) was obtained using a relatively long arc time for the splicing process. When the arc time is reduced, coupling to the two modes become unequal, as indicated in the filtering spectrum (**Fig. 1** (c)) that shows larger irregularity and a reduced extinction ratio. In addition, the insertion loss is increased, which indicates a stronger coupling to the radiation modes in the TMF.

The demonstrated comb filter has a working wavelength range from 1450nm to 1540nm. Note that the period of the comb filter becomes larger as the wavelength approaches the cutoff wavelength of the fiber, which is likely due to the dispersion of n_{02} near the cutoff wavelength. By optimizing the index profile of the TMF, it should be possible to adjust the working wavelength of the comb filter, improve its spectral uniformity, and reduce its insertion loss.
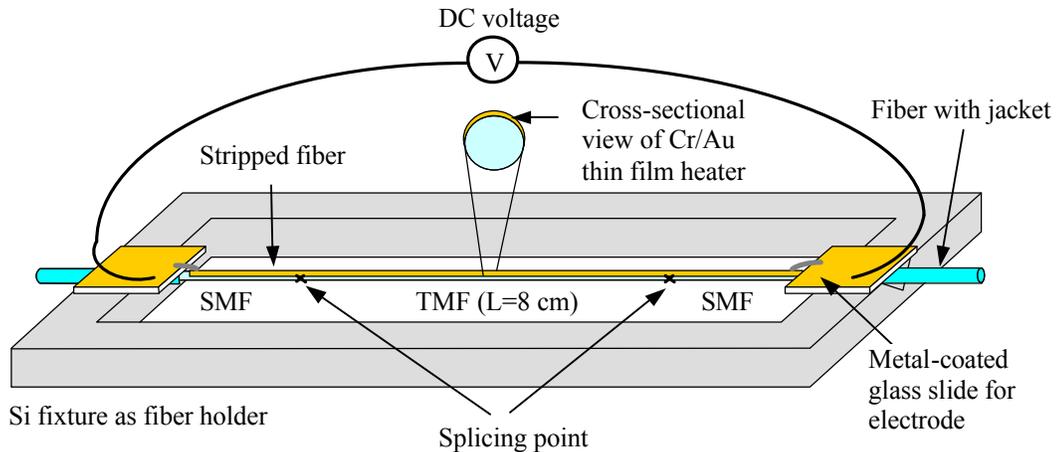

Fig. 2: Schematic of the electrically tuned all-fiber comb filter

To make the comb filter wavelength tunable, we suspend the filter at two ends using Si V-grooves and deposited a thin film micro-heater (Ti/Au 12nm/120nm) on the TMF from the top. **Fig. 2** shows a schematic of the finished device. The measured resistance of the micro-heater is 240Ω. **Fig. 3** (a) and (b) show the tuning spectra of the comb filter having a TMF length of 80 mm and the corresponding tuning efficiency. Electrical power as low as 115mW is used to tune the comb filter by half of its FSR (~0.85nm), thus covering the entire wavelength range. This corresponds to a tuning efficiency of 7.45nm/W, which is similar to our previous tunable FBG fabricated using a similar process [7]. It should be noted that the micro-heater which also functions as a temperature sensor can be used for active temperature stabilization [8]. Compared to previously reported fiber comb filters [2-4], the TMF-based comb filter has comparable performance but is considerably more compact and is thus expected to be more insensitive against temperature drift. The tunable comb filter can in principle be concatenated to realize more complicated filtering functions.
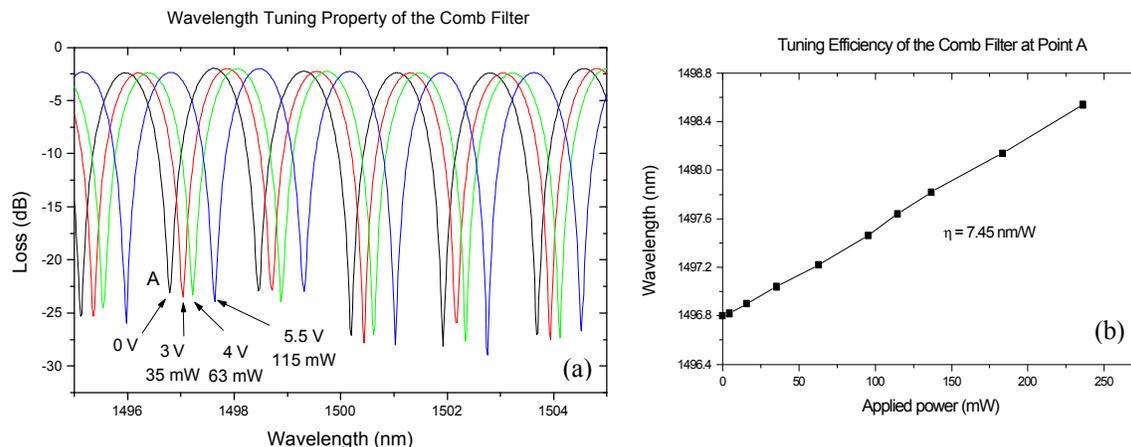

Fig. 3: (a) Wavelength tuning of the comb filter with a thin film micro-heater, (b) Tuning efficiency of the comb filter.

4. Conclusion

In summary, we demonstrated an all-fiber tunable comb filter. Compared with the existing comb filters, this device is ultra simple and compact, which make it an ideal low-cost solution for WDM multi-channel filtering applications.

Acknowledgement

References

1. A. Bellemare, M. Karasek, M. Rochette, S. LaRochelle, and M. Tetu, "Room temperature multifrequency erbium-doped fiber laser anchored on the ITU frequency grid," J. Lightwave Technol., **18**, 825–831 (2000).
2. H. L. An, X. Z. Lin, E. Y. B. Pun, and H. D. Liu, "Multi-wavelength operation of an erbium-doped fiber ring laser using a novel dual-pass Mach–Zehnder comb filter," Opt. Commun., **169**, 159–165 (1999).
3. X. Fang and R. O. Claus, "Polarization-independent fiber wavelength division multiplexer based on a Sagnac interferometer," Opt. Lett., **20**, 2146–2148 (1995).
4. X. J. Gu, "Wavelength-division multiplexing isolation fiber filter and light source using cascaded long-period fiber grating," Opt. Lett., **23**, 509–510 (1998).
5. D. Menashe, M. Tur, and Y. Danziger, "Interferometric technique for measuring dispersion of high order modes in optical fibers," Electron. Lett., **37**, 1439–1440 (2001).
6. T. Yokokawa, T. Kato, T. Fujii, Y. Yamamoto, N. Honma, A. Kataoka, M. Onishi, E. Sasaoka, K. Okamoto, "Dispersion compensating fiber with large negative dispersion around -300 ps/km/nm and its application to compact module for dispersion adjustment," OFC 2004 Technical Digest, FK5, 717-718 (2004).
7. E. R. Lyons and H. P. Lee, "An efficient electrically tunable etched cladding fiber Bragg grating filter tested under vacuum," IEEE Photonic Tech. Lett. **13**, 484-486 (2001).
8. B. J. Eggleton, J. A. Rogers, P. Kuo, "Temperature stabilized tunable fiber grating devices with integrated on-fiber thin film heaters," OFC 2000 Technical Digest, TuH2, 115-117 (2000).

High-channel-count comb filter with a simple structure

Xiangfei Chen, Jin Mao, Xuhui Li, Zhongqiang Lin, Shizhong Xie and Chongcheng Fan

Broadband Optical Network Research Laboratories, Department of Electronics Engineering, Tsinghua University, 100084, Beijing, P. R. China.

Fax: +86-10-62770317. E-mail: chenxf@tsinghua.edu.cn

Abstract: Based on the analysis of comb filter formed by highly chirped sampled Bragg grating, a 36-channel comb filter is fabricated with 28nm bandwidth, 0.31nm channel bandwidth (0.5dB), >22dB adjacent channel isolation and <0.4dB insertion loss.

I. Introduction:

Multi-wavelength sources and multi-channel isolation filters are essential in dense wavelength-division-multiplexed (DWDM) networks. Among them, broadband comb filters with high channel count, deep isolation between adjacent channels, flat-top filtering, and low and uniform insertion loss have been investigated [1-3] while a number of technologies, such as Sagnac interferometer [4] and dual-pass Mach-Zehnder interferometer [5], are reported. Although fiber Bragg grating (FBG) devices are playing increasingly important roles in filtering and dispersion compensation, it is difficult to manufacture high channel-count devices based on such gratings. One solution to this problem is to provide a sinc-sampled superstructure in the FBG, whose multi-channel reflection spectrum can be predicted by the Fourier transform of the sampling function [6]. This approach needs a lot of phase shift and precise apodizing along the grating. An improved approach has been proposed in Ref. [7] where only phase sampling was implemented, and the effective Bragg reflection area is greatly increased. However, the fabrication of both the phase mask and fiber grating is quite complicated and difficult.

A novel high channel-count comb filter employing a highly-chirped sampled Bragg grating (SBG) has been proposed recently [8]. This kind of comb filter features in high performance and can be fabricated by conventional (low-cost) technology. In this paper, an analytical expression of such kind of comb filters is provided and a comb filter is experimentally demonstrated for the first time. The comb filter has a bandwidth of 28nm, channel spacing of 100GHz, inter-channel isolation >22dB, in-band insertion loss <(0.4±0.1)dB with low ripple(<±0.05dB).

II. Description of all-fiber distributed comb technology

In terms of Fourier transformation, a SBG can be regarded as a special grating with multiple superimposed sub-gratings (ghost gratings), leading to multi-channel operation. At the same time, the highly chirped underlying grating can provide enough Bragg response in the whole working bandwidth. When the contribution of every sub-grating is in-phase with each other, the transmission resonance occurs, and the flat-top response can be obtained [8]. This kind of comb filter is based on the principle of distributed feedback (DFB). In the following, a relation inside the principle will be exposed simply and with the relation, a comb filter is fabricated.

The frequency spacing between neighboring superimposed gratings is

$$\delta f_1 = \frac{v_l}{2nP} \tag{1}$$

When P is the sampling period, v_l is the light velocity in vacuum and n is the average refractive index of the grating. When the SBG has a (relatively) large chirp, the frequency difference between neighboring samples

(induced by the chirp) is then

$$\delta f_2 = \frac{cPv_l}{\lambda_{Bragg}} \qquad (2)$$

where c is the chirp coefficient. If δf_1 and δf_2 are "matching" or "in-phase", namely $\delta f_1 = m\delta f_2$ or $\delta f_2 = m\delta f_1$ and m is an integer, we have

$$\delta f^2 = \frac{cv_l^2}{2|m|n\lambda_{Bragg}} \quad (m=\pm 1, \pm 2,...) \qquad (3)$$

where δf is the minimum of δf_1 and δf_2, and the sampling period P can be determined by:

$$P = \begin{cases} \dfrac{v_l}{2|m|n\delta f} & \delta f_2 = m\delta f_1 \\ \dfrac{|m|v_l}{2n\delta f} & \delta f_1 = m\delta f_2 \end{cases} \quad (m=\pm 1,\pm 2,...) \qquad (4)$$

Eqs. (3) and (4) show the basic principle for a large-bandwidth comb filter based on highly chirp SBG.
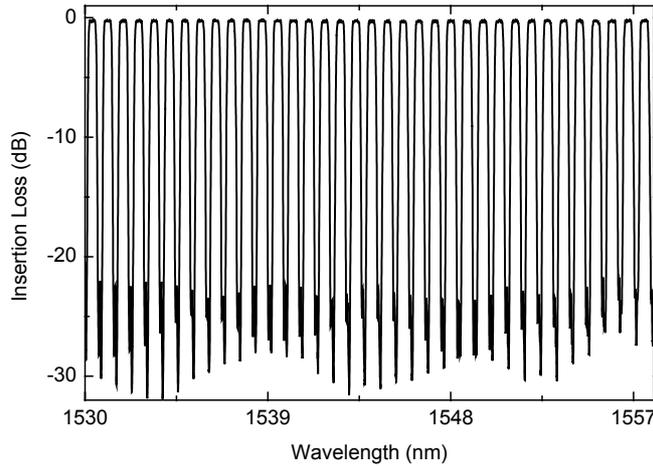

Fig. 1: Transmission spectrum of a single comb filter with 36 channels spacing by 100GHz

III. Experimental results and discussion:

A comb filter was fabricated simply through the standard scan-writing technology. The phase mask we used is 4.4cm long and its chirp rate is equal to 5.19nm/cm. In this experiment, m was selected to be equal to 1, and the center Bragg wavelength is 1545nm. The sampling period P is then 1.043cm and the channel spacing is almost 100GHz (=99GHz) according Eqs. (3)-(4). The optical response of the transmission filter fabricated by us is shown in Fig. 1. The bandwidth of the broadband comb filter is 28nm, or 36 channels (close to full C-band). The isolation depth between adjacent channels is larger than 22dB. The enlarged show of the top of the transmission spectrum of the filter is plotted in Fig. 2, where the excess loss of the grating is below 0.4dB, and the uniform of the insertion loss is less than ± 0.1dB within 28nm bandwidth, the ripple within each band is less than $\pm .0.05$dB and the 0.5dB bandwidth is about 0.31nm. We had fabricated a few comb filter through the conventional

scan-writing technology. The experiment results is proved to be stable and the filtering performance is very similar for most comb filters (>85%). Moreover, method by using an amplitude mask to form the samples, which is widely used, should be more effective. With the method, mass production of the comb filter may be available.
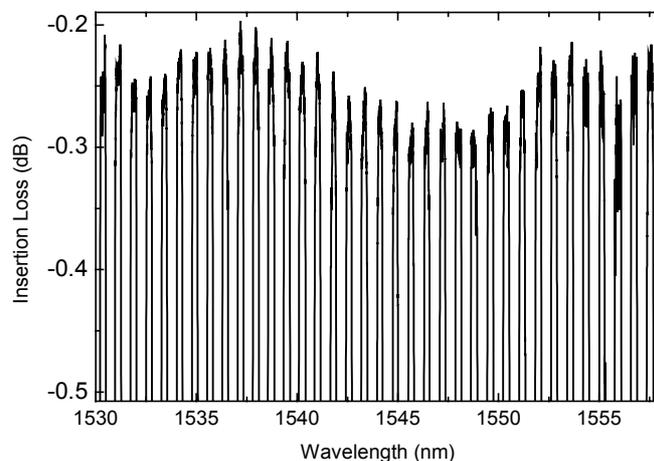

Fig. 2: Detail show of the top of the transmission spectrum in Fig. 1. The variation channel to channel is less than ±0.1dB

IV. Conclusion:

In this paper, we present an analytical expression for a comb filter based on lager-chirp SBG and reported such a comb filter for the first time. The expression is ultra useful for designing high-perform, high-count comb filter. This filter can be fabricated with a simple setup and process and thus meets the demand of mass production and low cost. Moreover, the fabrication of the filter is stable and has good repetition. The dimension of the filter is same as the conventional fiber-Bragg-grating based filter, which is widely used in fiber systems, such as pump stable filter and gain flatten filter. Thus the proposed filter may has good potential for the applications of the next-generation high-count-channel systems.

References

[1] J. Chow et al., IEEE Photon. Technol. Lett., 8 (1996), 60

[2] In Kag Hwang et al., IEEE Photon. Technol. Lett., 10 (1998), 1437

[3] Junqiang Sun et. al., IEEE Photon. Technol. Lett., 14 (2002), 750

[4] X. Shu et al., IEEE Photon. Technol. Lett., 12 (2000), 980.

[5] H.L. An, et al., APCC/OECC'99 2 (1999), 1495.

[6] M. Ibsen et al., IEEE Photon. Technol. Lett., 10 (1998), 842

[7] J.E. Rothenberg, et al., OFC'2002, ThAA1.

[8] Xiangfei Chen et al., IEEE Photon. Technol. Lett., 12 (2000), 1501

Interference-Based Optical MEMS Filters

Olav Solgaard, Ruslan Belikov, Kyoungsik Yu
Department of Electrical Engineering, Stanford University, 450 Via Palou, Stanford, California 94305
solgaard@stanford.edu

Abstract: In this paper we describe tunable interference filters based on arrays of MEMS micromirrors. A simple analytical description of the height distribution of micromirrors needed to create a desired spectral response is presented, and the implications on the design and utility of MEMS interference filters are discussed. Finally we describe two practical filter implementations. The first enables continuous spectral control over relatively broad bands, and the second is designed for Wavelength-Division-Multiplexed fiber optic communication systems.
© 2003 Optical Society of America
OCIS codes: 050.1970 Diffractive optics, 350.3950 Micro-optics, 350.2460 Filters, interference

1. Introduction

Spatial Light Modulators (SLMs) based on micromirror arrays are among the most successful applications of MicroElectroMechanical Systems (MEMS) technology. The development of projection systems based on MEMS mirrors started in the early 1970's [1,2] and the technology are now being used in a variety of fields including video projection, high-definition television, maskless lithography, and fiber switches [3,4]. Traditionally such systems created optical contrast in the image plane by rotating the micromirror that defined a pixel and thereby throwing the light from that pixel outside the optical aperture of the imaging system. Alternatively, the contrast can be achieved by taking advantage of the diffractive properties of MEMS structures by creating microgratings [5]. Such SLMS are now starting to emerge as competitors to micromirror-based SLMs in several applications including projection displays [6], and voltage controlled optical attenuators for fiber optics [7], while more complex diffractive MEMS SLMs are being developed for demanding applications like maskless lithography [8].

Light valves based on diffractive optical effects are inherently dispersive, and can therefore be used as optical filters and spectrometers. Early demonstrations of such filters [9,10] were based on microgratings, in which the individual grating elements can be actuated separately to create a tunable diffractive surface. The surface can then be programmed to diffract part of the spectrum into a certain direction, thereby creating a spectral filter. This is a compelling technology because the large number of degrees of freedom in MEMS SLMs can be used to create filters and spectrometers with much more flexible and high-resolution control of the spectral response than is possible with other tunable optical filter technologies.

2. Impulse Response Description of Diffractive Optical Filters

It is relatively straight forward to analyze the diffraction from an array of MEMS mirrors once the state of the mirrors are known, but the inverse problem of synthesizing a diffracting state that will produce a specified spectral response is more complex. The common approach is to use suitably modified versions of iterative numerical procedures originally developed for synthesis of diffractive optics meant to create monochromatic two-dimensional patterns [9,10,11]. The synthesis problem can, however, be significantly simplified by utilizing the fact the height distribution of a diffractive surface is given by the Fourier Transform of its spectral response.

The Fourier relationship between the spectral response and the height distribution of a diffractive surface can be visualized by considering the impulse response of the simplified filter setup of Fig. 1. In this filter the input light is coming from the right on the single mode fiber and is collimated onto the diffractive surface. The desired part of the optical spectrum is diffracted back onto the single mode fiber, which also acts as the output. If the input is an impulse, the output will be a train of impulses with relative amplitudes given by the surface areas of the different height levels of the diffractive optics. The consequence is that the required height distribution is given by the impulse response, which is the Fourier Transform of the desired spectral response.

If for simplicity we assume that the diffractive surface has a discreet set of N height levels with uniform separation between levels, the impulse response $h(t)$ can be expressed as

$$h(t) = \frac{1}{N} \sum_{n=1}^{N} h[n] \delta(t - n\tau)$$ (1)

where $h[n]$ is the fraction of the illuminated surface that gives a relative time delay of $n\tau$. Here $h[n]$ is arbitrary within the constraint $0 \le h[n] \le 1$, but it can be shown that any arbitrary complex-valued filter can be synthesized to a multiplicative constant under certain bandwidth and resolution constraints that depend on N and τ [12]. This is remarkable because it shows that by doing only phase modulation (moving the MEMS reflectors vertically to create new height distributions, $h(n)$) we can control both the spectral amplitude and the spectral phase of the response of the filter. Control of the spectral phase is important even if the primary objective is to control amplitude, because if the phase is not controlled, the filter will have phase shifts where the amplitude response will go through a zero.
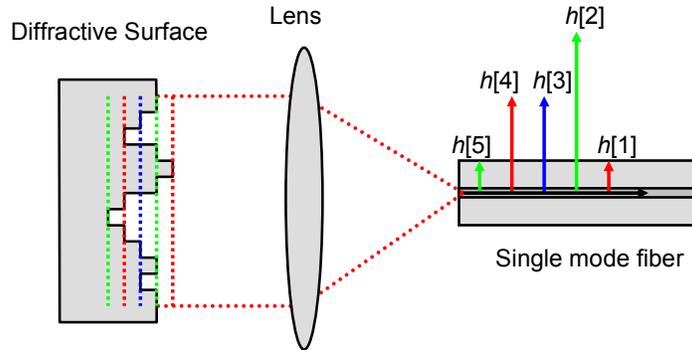

Fig. 1. Schematic drawing of diffractive optical filter.

3. Implementation of interference-based MEMS filters:

Practical filters will be more complex than the setup in Fig. 1, but any interference based filter can be described by a suitably modified version of Eq. 1. In particular, any interference based filter that is based on interference between N channels will suffer an average loss of $1/N$ on average over the Free-Spectral-Range (FSR) as indicated in Eq. 1. This shows that for interference based filters there is a tradeoff between loss and coverage of the FSR, and consequently, the implementation of such filters depend strongly on the requirements of the specific applications.

The filter shown in Fig. 2 enables synthesis of arbitrary spectra over half the FSR, but the losses increase linearly with the number of individually controllable points of the spectral response. The spectrum can only be controlled over half the FSR because the filter is Hermitian. This type of filter can be implemented with commercial MEMS SLMs, and has been demonstrated for both spectral filtering [13] and femto-second laser pulse shaping [14].
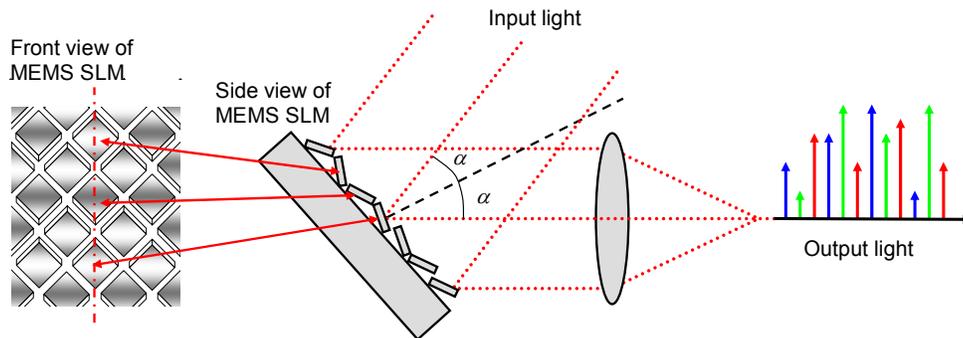

Figure 2. Implementation of interference based MEMS filter using commercial MEMS SLMs. The input light is normal to the SLM surface, and only the parts of the input that illuminates micromirrors that are rotated to the right interfere to create the output. Each row of the SLM corresponds to a certain time delay or height, and the height distribution required to create a desired filter is therefore created by rotating to the right the correct number of mirrors in each row.

An alternative implementation based on a Gires-Tournois interferometer is shown in Fig. 3. In this filter, the FSR is small due to the relatively large distance between the micromirror array and the beam splitter. In practice the FSR is

set up to match the channel spacing of a WDM system such that the filter performs the same function on each channel. The number of mirrors in the filter must be kept relatively small to limit the optical losses to acceptable levels. A number of filter functions has been demonstrated using this type of device, including tunable center wavelength and channel (de)interleaving [15], tunable dispersion compensation [16], and tunable bandwidth [17].
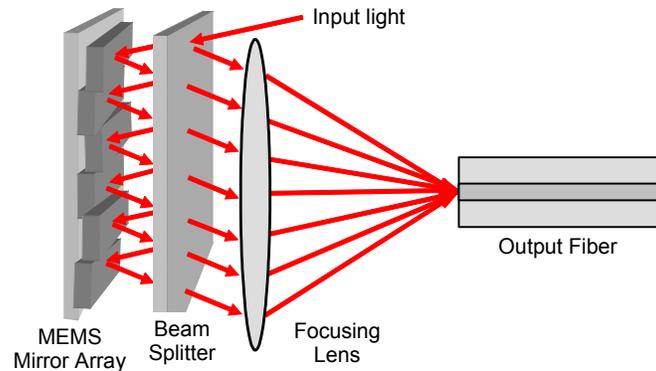

Figure 3. Schematic structure of the MEMS Gires-Tournois interferometer/filter. The phase shifts controlled by the micromirrors determine the transfer function of the filter.

4. Conclusion:

Diffractive micromirror arrays can act as tunable interference optical filters with large numbers of degrees of freedom. A simple impulse-response picture can be used to derive an analytical expression for the height distribution that is needed to synthesize a desired filter. The analytical theory shows that micromirrors with only phase modulation can be used to control of both spectral amplitude and phase of the optical filters, and that there is a tradeoff between filter complexity and average loss over the FSR, suggesting different implementations for different applications.

5. References:

1. R.N. Thomas, J. Guldberg, H.C. Nathanson, P.R. Malmberg, "The mirror matrix tube, A novel light valve matrix for projection displays", IEEE transactions on Electron Devices **ED-22**, 765 (1975).
2. K.E. Peterson, "Micromechanical light modulator array fabricated on silicon", Applied Physics Letters **31**, 521 (1977).
3. L.J. Hornbeck, Deformable-mirror spatial-light modulators", Proceedings of the SPIE **1150**, 86-102 (August 1989).
4. D. Dudley, W. Duncan, J. Slaughter, "Emerging Digital Micromirror Device (DMD) Applications", Proceedings of the SPIE **4985**, 14-25 (2003).
5. O. Solgaard, F.S.A. Sandejas, D.M. Bloom, "A deformable grating optical modulator", Optics Letters **17**, 688-690 (1 May 1992).
6. S.R. Kubota, "The Grating Light Valve Projector", Optics & Photonics News **13**, 50-53, (September 2002).
7. A. Godil, "Diffractive MEMS technology Offers a New Platform for Optical Networks", Laser Focus World, 181-185, (May 2002).
8. P. Durr, U. Dauderstadt, D. Kunze, M. Auvert, T. Bakke, "Characterization of Spatial Light Modulators for Micro Lithography", Proceedings of the SPIE, **4985**, 211-229 (2003).
9. M. B. Sinclair, M. A. Butler, A. J. Ricco, and S. D. Senturia, "Synthetic spectra: a tool for correlation spectroscopy," Applied Optics **36**, 3342-3348 (1997).
10. G. B. Hocker, D. Youngner, M. Butler, M. Sinclair, T. Plowman, E. Deutsch, A. Volpicelli, S. Senturia, A. J. Ricco, "The polychromator: a programmable MEMS diffraction grating for synthetic spectra", Solid State Sensor and Actuator Workshop, Hilton Head Island, SC, 89-91 (June 4-8, 2000).
11. G. Zhou, F.E.H. Tay, F.S. Chau, "Design of the diffractive optical elements for synthetic spectra", Optics Express **11**, 1392-1399, (2003).
12. R. Belikov, O. Solgaard, "Optical Wavelength Filtering by Diffraction from a Surface Relief", Opt. Lett., **28**, 447-449 (March 2003).
13. R. Belikov, X. Li, O. Solgaard, "Programmable Optical Wavelength Filter Based on Diffraction from a 2-D MEMS Micromirror Array," Proceedings of CLEO, Baltimore, MD (June 1-6, 2003).
14. R. Belikov, C. Antoine-Snowden, O. Solgaard, "Femtosecond Direct Space-to-Time Pulse Shaping with MEMS Micromirror Arrays", Proceedings of the 2003 IEEE/LEOS International Conference on Optical MEMS, Waikoloa, Hawaii (18-21 August 2003).
15 K. Yu, O. Solgaard, "MEMS optical wavelength deinterleaver with continuously variable channel spacing and center wavelength", IEEE Photonics Technology Letters **15**, 425-427 (March 2003).
16. K. Yu, O. Solgaard, "Tunable Chromatic Dispersion Compensators Using MEMS Gires-Tournois Interferometers", Proceedings of the 2002 IEEE/LEOS International Conference on Optical MEMS, Lugano, Switzerland, 181-182 (20-23 August 2002).
17. K. Yu, O. Solgaard, "Tunable Bandwidth optical filter based on MEMS Gires-Tournois interferometer", Proceedings of the 2003 IEEE/LEOS International Conference on Optical MEMS, Waikoloa, Hawaii (18-21 August 2003).

Apodization of 25 and 50 GHz low dispersion FBG WDM filters by phase modulation coding of a phase mask

Michel Poulin, Aidan Doyle, François Trépanier, Alain Mailloux, Martin Guy, Michel Morin, Josh Rothenberg*

Teraxion, 20-360 Franquet
Québec, Qc, G1P 4N3, Canada
Phone : 418-658-9500 x 349, Fax : 418-263-0253, email : mpoulin@teraxion.com
*Northrop Grumman Space Technology, Bldg R1 - Rm 1144B One Space Park
Redondo Beach, CA 90278

Abstract: Low dispersion FBG grating WDM filters are written in a simple and efficient way using a complex phase mask. High frequency phase modulation and $\pi/2$ phase shifts encoded into the mask provide the required apodization profile.
©2003 Optical Society of America
OCIS codes: (060.2340) Fiber optics components, (050.1950) Diffraction gratings

1. Introduction
High performance low dispersion fiber Bragg grating (FBG) WDM filters require complex apodization functions (variation of the fringe visibility and phase). Different techniques have been proposed for apodizing and incorporating phase shifts in fiber Bragg gratings [1-5]. A commonly used technique uses a dithering of the mask for varying the fringe contrast [2]. However, the piezo-element calibration requirement of this technique impairs the yield in the fabrication process. For a cost-efficient manufacturing process, the complex apodization function may be included in an amplitude modulated phase mask [4-5]. On the other hand, phase modulated phase masks have been used for the fabrication of high channel count dispersion compensators [6]. As shown here, phase modulated phase masks can also be used to generate apodized Bragg gratings, thus considerably facilitating the recording of low dispersion WDM filters.

2. Apodization technique
The apodization technique consists in adding a short period phase modulation to the fringe pattern of a FBG. The phase modulation of an optical signal generates sidebands at multiples of $\pm f_m$ from the carrier frequency, where f_m is the modulation frequency. Similarly, a phase modulation of period P applied to the fringe pattern of an FBG induces sidebands in the reflectivity spectrum at multiples of $\pm c/2nP$ from the Bragg optical center frequency, where c is the speed of light in vacuum and n is the group index of the optical fiber mode. The creation of sidebands occurs at the expense of the reflectivity at the Bragg frequency. By changing the local strength of the phase modulation, it is therefore possible to change the local reflectivity of the center channel and thus generate an apodization profile. The phase modulation period must be short enough that sidebands are created outside of the frequency band of interest. The short period phase modulation is preferably encoded into the phase mask. In this way, fully apodized Bragg gratings can be written using a simple exposure technique (small beam scanning or large uniform beam illumination).

3. 25 GHz and 50 GHz low dispersion FBG WDM filters
The complex apodization profiles for the 25 and 50 GHz filters are shown in fig. 1. A complex phase mask has been lithographically fabricated using these apodization profiles. $\pi/2$ phase shifts are required in the phase mask at every null of the apodization function. The apodizing phase modulation has a period of 25 μm on the phase mask. It produces sidebands in the reflectivity spectrum at ± 4 THz (~32 nm) from the center frequency of the FBG filter. The theoretical group delay ripple (GDR) of these filters is around 5 ps.

4. Experimental results
The filters were written with a single pass of a scanning 244 nm UV beam lasting about 60 seconds. The experimental spectral response and group delay ripple of both filters are shown in figure 2. Reflection sidebands created by the phase modulation at multiples of 4 THz on the red side of the Bragg wavelength can be seen in figure 3. Similar reflection peaks are also expected on the blue side of the Bragg wavelength but were not observed because of the limited spectral range of the measurement system.
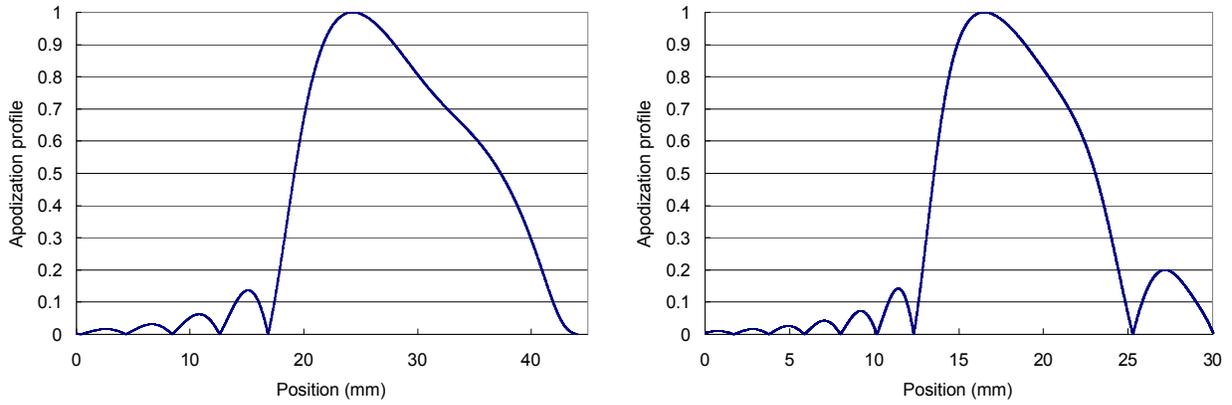
Fig. 1 : Apodization profiles for 25 GHz (left) and 50 GHz (right) low dispersion WDM filters.
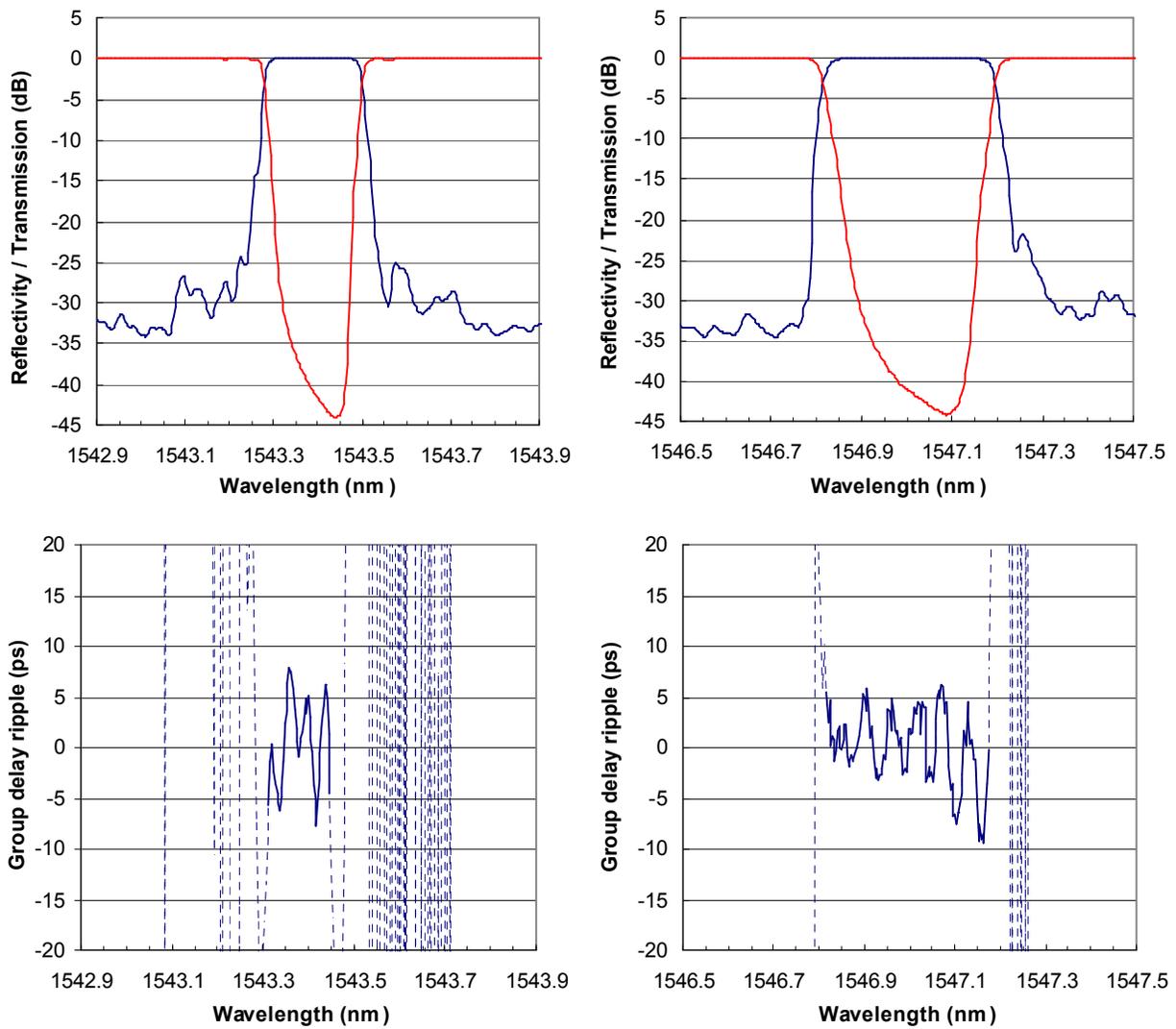

Fig. 2: Top: Measured reflectivity/transmission spectra for the 25 GHz (left) and 50 GHz (right) WDM filters. Bottom: Measured group delay ripples for the corresponding filters.
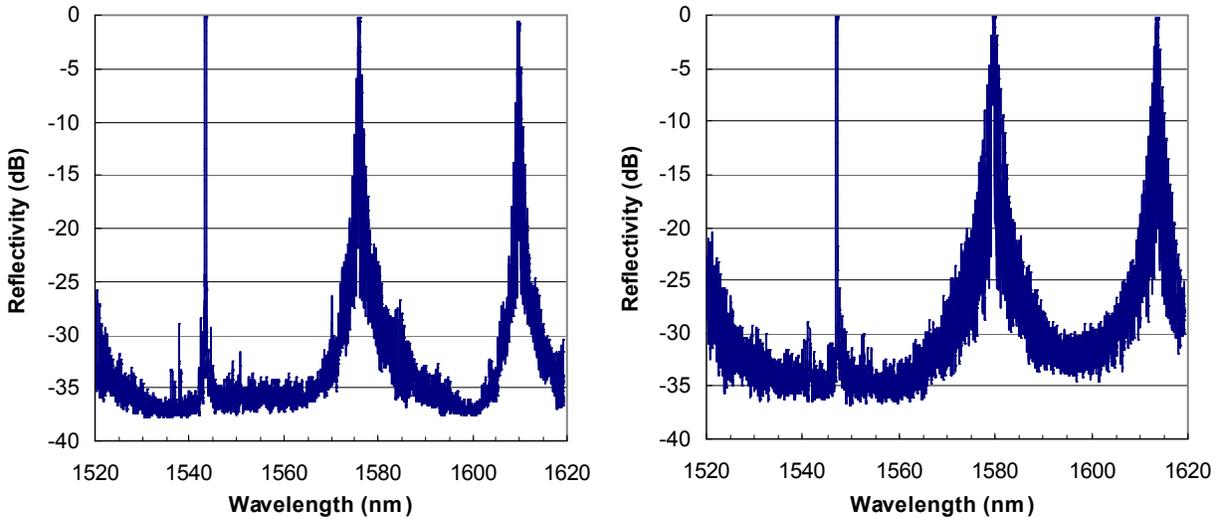
Fig. 3: Extended spectral measurements showing sidebands induced by the phase modulation used for the apodization of a 25 GHz (left) and 50 GHz (right) WDM filter.

The WDM filters display very good optical characteristics. Their filling factors (ratio of spectral bandwidths at −0.5 and −25 dB) are between 0.65 and 0.7. It compares to that of filters produced with a continuous grating writing technique [7]. The GDR of our filters is somewhat higher (< 13 ps) due to the practical length of the gratings which puts some limits on the design. The isolation is rather good, exceeding 25 dB everywhere and, apart from little spikes, being larger than 30 dB at non-adjacent channels. For filters written at band edges (near 1530 or 1560 nm), the reflected power around +/-32 nm can be reduced by using a higher modulation frequency in order to guarantee a good isolation over the whole C-band.

5. Conclusion

Low dispersion 25 and 50 GHz WDM filters have been realized using a lithogaphically prepared complex phase mask containing all the phase information required to generate both the phase shifts and the apodization profile in the fiber. Using this phase mask, complex dynamic recording techniques are thus avoided. Low dispersion WDM filters with a narrower bandwidth could be obtained with the same technique. Bragg gratings of any type can be apodized with this technique. This complex phase mask approach could also be used to record complex FBG filters in other optical devices such as planar lightwave circuits.

6. References

[1] B. Malo, S. Thériault, D. C. Johnson, F. Bilodeau, J. Albert, K. O. Hill, "Apodised in-fibre Bragg grating reflectors photoimprinted using a phase mask", *Electron. Lett.*, Vol. 31, pp. 223-225 (1995).

[2] M. J. Cole, W. H. Loh, R. I. Laming, M. N. Zervas, S. Barcelos, "Moving fibre/phase mask-scanning beam technique for enhanced flexibility in producing fibre gratings with uniform phase mask", *Electron. Lett.*, Vol. 31, No. 17, pp. 1488-1490 (1995).

[3] R. Kashyap, A. Swanton, D. J. Armes, "Simple technique for apodising chirped and unchirped fibre Bragg gratings", *Electron. Lett.*, Vol. 32, pp. 1226-1227 (1996).

[4] J. Albert, K. O. Hill, B. Malo, S. T. Thériault, F. Bilodeau, D. C. Johnson, L. E. Erickson, "Apodisation of the spectral response of fibre Bragg gratings using a phase mask with variable diffraction efficiency", *Electron. Lett.*, Vol. 31, pp. 222-223, (1995).

[5] F. Trépanier, M. Poulin, Ghislain Bilodeau, "Complex apodized holographic phase mask for FBG writing", Bragg gratings, photosensitivity and poling in glass waveguides Conference, Paper WC5, Monterey, CA, USA, 2003.

[6] J. E. Rothenberg, H. Li, Y. Li, J. Popelek, Y. Sheng, Y. Wang, R. B. Wilcox, J. Zweiback, "Dammann fiber Bragg gratings and phase-only sampling for high channel counts", *IEEE Photon. Technol. Lett.*, Vol. 14, No. 9, pp. 1309-1311, 2002.

[7] M. Ibsen, P. Petropoulos, M. N. Zervas, R. Feced, "Dispersion-free fibre Bragg gratings", Optical Fiber Communication Conference, Technical digest, paper MC1, Anaheim, USA, 2001.

Spectral anomalies due to coupling-induced frequency shifts in dielectric coupled-resonator filters

Christina Manolatou[†], Miloš A. Popović[‡], Peter T. Rakich, Tymon Barwicz, Hermann A. Haus and Erich P. Ippen

Research Laboratory of Electronics, Massachusetts Institute of Technology, 77 Massachusetts Ave, Cambridge, Massachusetts 02139
[†]krist@alum.mit.edu, [‡]milos@mit.edu

Abstract: Coupling-induced frequency shift is identified as a source of spectral response degradation in higher-order coupled-resonator add/drop filters that must be compensated in design. The theoretical basis and experimental verification are presented, and generic solutions proposed.
©2003 Optical Society of America
OCIS codes: (130.3120) Integrated optics devices; (230.5750) Resonators; (230.7370) Waveguides.

1. Introduction

Coupled dielectric resonator filters are candidates for integrated WDM channel add/drop applications, with well-developed synthesis techniques [1-3]. In response synthesis, precise control of the resonance frequencies and mutual couplings is required. In series-coupled add/drop filters, for example, the uncoupled resonance frequencies must be identical [1]. Herein, a coupling-induced frequency shift (CIFS) in resonators is identified as an effect that may hinder the realization of the desired response if left uncompensated. The frequency shift can be explained as the self-excitation of a resonant mode, via the index perturbation of a second structure, with a temporal phase shift such that its frequency is modified. The shift may be negative or positive depending on the dominant of two contributing effects to be described. In what follows, the CIFS is theoretically explained within coupled mode theory formalism, and corroborated by FDTD simulations. Degradation of higher-order filter responses due to the CIFS is investigated by way of a third-order series-coupled microring filter model, with comparison to experimental results from such a filter. A modification of filter synthesis is suggested to recover ideal responses. Generic solutions for compensation of the relevant resonators are proposed.

2. Theoretical basis for negative and positive coupling-induced frequency shifts

Coupling of modes in time (CMT) [4] provides a treatment of the interaction of arbitrary coupled dielectric resonators. Evolution of the amplitudes $\vec{a}(t)$ of uncoupled modes in the coupled system can be described by

$$\frac{d}{dt}\vec{a} = j\boldsymbol{\omega} \cdot \vec{a} - j\mathbf{W}^{-1} \cdot \mathbf{M} \cdot \vec{a} = j\boldsymbol{\omega} \cdot \vec{a} - j\boldsymbol{\mu} \cdot \vec{a} \qquad (1)$$

where $\boldsymbol{\omega}$ is a diagonal matrix of uncoupled resonance frequencies, $\mathbf{W}$ is the energy non-orthogonality matrix, and $\mathbf{M}$ is a coupling overlap matrix. $\boldsymbol{\mu}$ represents a total effective coupling matrix with respect to mode amplitudes taking energy non-orthogonality into account. The coupling-induced frequency shift (CIFS) results from self-coupling terms on the diagonal of $\boldsymbol{\mu}$. For the resonator associated with amplitude a_1 of a total of two modes, the shift is

$$\delta\omega_1 = -\mu_{11} = -\frac{M_{11} - \frac{W_{12}}{W_{22}}M_{21}}{W_{11} - \frac{W_{12}}{W_{22}}W_{21}}. \qquad (2)$$

In absence of coupling $\delta\omega_1 = 0$, and resonators oscillate at natural frequencies in $\boldsymbol{\omega}$. Under coupling, the CIFS in (2) is generally non-zero. It can be critical in filter design and can seriously degrade performance if left uncompensated.

We briefly consider the physical origin of the CIFS. For orthogonal modes (e.g. a resonator perturbed by a nearby dielectric object with no relevant modes of its own) $W_{12} = W_{21} = 0$, and from (2) the frequency shift is negative since M_{ii}/W_{ii} is positive definite in the lossless case. This is an intuitive result if one considers the wave equation, or its stationary integral for frequency: a positive refractive index perturbation is introduced, so the frequency must decrease. In the case of adjacent evanescently-coupled resonators (e.g. [1,2]), the basis is normally not orthogonal. A second, positive CIFS contribution then arises due to the shared cross-energy of the modes. Since cross-coupling M_{21} (source of power exchange) is a large term relative to self-coupling M_{11}, the net CIFS could be found positive. This initially unintuitive result is easily understood in the spatial picture that follows.
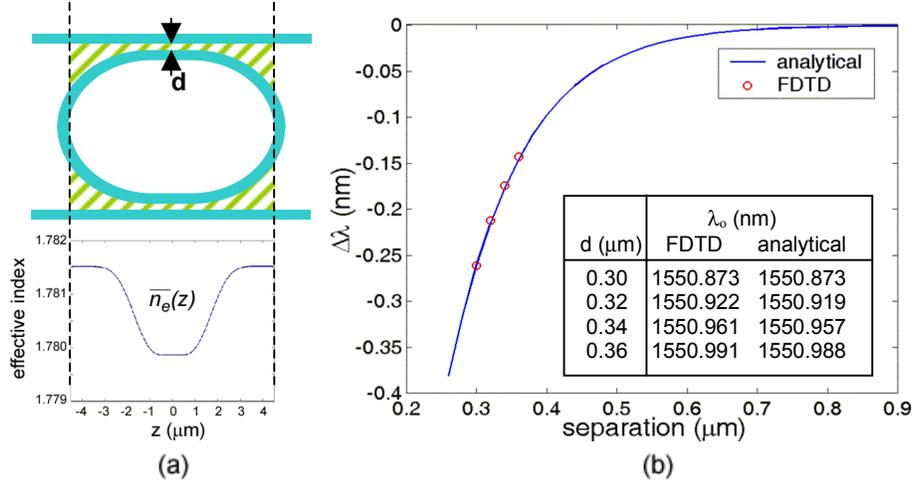
Fig. 1. Coupled-mode theory prediction and FDTD simulation of coupling-induced frequency shift. (a) geometry of CMT integration of the self-phase shift and effective index vs. position; (b) CIFS from coupled mode theory and FDTD.

Coupling of modes in time provides a framework for numerical evaluation of CIFS in standing or traveling wave resonators of arbitrary shapes. The shift may also be obtained using a resonant-mode solver or FDTD.

3. Coupling of modes-in-space picture for microrings and racetracks and FDTD verification of the CIFS

For traveling wave resonators including rings and racetracks, the CIFS is simply understood by using a coupling of modes in space [4] picture to consider the self-phase-shift accumulated in directional couplers. The propagation constant β_i of a waveguide is modified by the diagonal terms $\delta\beta_i$ of a coupling matrix analogous to that in (1). To translate the accumulated phase shift into a frequency shift for a ring/racetrack resonator, an approximate formula may be used that integrates the perturbation-induced $\delta\beta_i$ along the couplers to find a total phase shift and CIFS:

$$\delta\beta_1 = \frac{K_{11} - \frac{P_{12}}{P_{22}}K_{21}}{P_{11} - \frac{P_{12}}{P_{22}}P_{21}}; \quad \delta\omega_1 = -\frac{\int_{L_c} \delta\beta_1(\omega_o,z)dz}{\frac{L-L_c}{v_g} + \int_{L_c}\frac{dz}{v_{g,c}(z)}} \quad (3a,b)$$

where $\delta\beta_1$ is given for mode 1 of two modes, **K** is the coupling overlap matrix and **P** is the non-orthogonality matrix [4]. For (3b), L is total cavity length, L_c is the length of coupler regions, $\delta\beta_1(\omega_o, z)$ is a spatially varying $\delta\beta_1$ from (3a) at the free-running frequency ω_o, and v_g and $v_{g,c}(z)$ are mode group velocities in uncoupled and coupler regions.

This picture confirms that the CIFS can be of either sign. K_{11} is the usual positive effective index (negative CIFS) contribution due to the presence of the high index adjacent bus waveguide or resonator. The second term in (3) that gives a positive CIFS contribution can be understood by considering two weakly guided TE coupled slabs of half the width necessary to cut off the second guided mode. At zero wall-to-wall spacing (strong coupling regime), the two guides merge and the antisymmetric mode becomes cut off, while the symmetric morphs into the fundamental guided mode. In approaching this situation, clearly the antisymmetric mode's effective index drops much faster than that of the symmetric mode rises. Thus there is a negative contribution to the average effective index of the two supermodes, which for identical coupled waveguides corresponds to a $\delta\beta < 0$ in (3), or a CIFS > 0.

A 2D FDTD simulation of a single TE racetrack resonator ($L = 34.6\mu m$) add/drop filter in which the anomalous positive CIFS was first observed is shown in Figure 1a. The free-running frequency was found as 1551.134nm, but under coupling to two bus waveguides it shifted to values given in the table in Fig. 1b, resulting in a positive CIFS of over -0.25nm or +30GHz. Figure 1b shows the results of a coupling-of-modes prediction of the frequency shift, using (3a) and (3b) integrated over the couplers (shaded region in Fig. 1a) of varying waveguide spacing. The close match of the exact CIFS and the coupling of modes prediction supports the given explanation of the effect.

4. CIFS impact on higher-order filter spectra and proposed correction to filter synthesis and design

While the impact on a single-resonator filter is a simple frequency shift in the response spectrum, the impact of the CIFS on higher-order filters is more serious. In synthesizing a prototype filter response, a set of desired resonant frequencies (identical for series-coupled add-drop filters) and normally different ring-ring and ring-bus couplings is
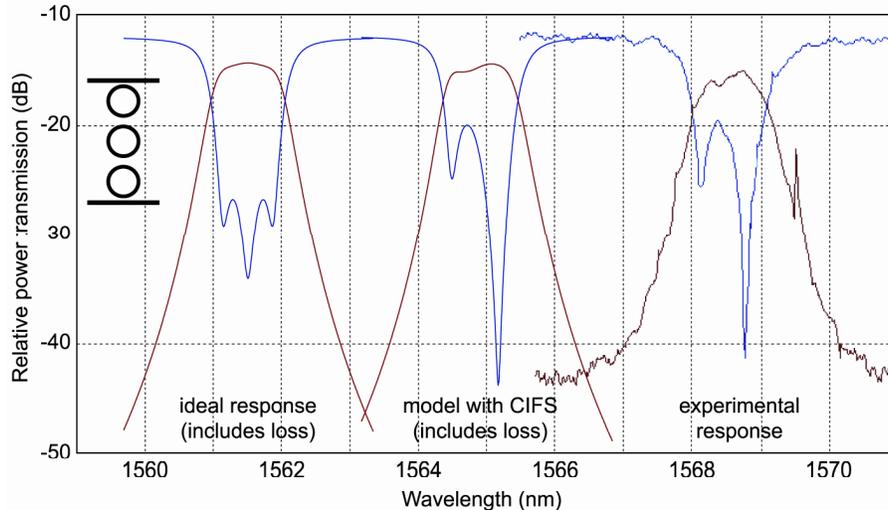
Fig. 2. Drop and thru port frequency responses of a 3rd-order filter using identical microrings (inset diagram): ideal theoretical response (left plot); theoretical model incorporating the expected net CIFS in the middle ring of +20GHz from CMT (middle plot); experimental measurement of the response of fabricated filter based on three identical rings (right plot). Loss is fit into the models to match experiment. Theoretical spectra are displaced horizontally for clarity in the plot.

to be achieved [1-3]. The CIFS due to different coupler gaps will be different, and will cause resonators to have different effective resonant frequencies within the same filter. In practical add/drop filters of [1], resonator-bus coupling is stronger than inter-resonator coupling, so the most significant frequency shift is normally seen to be due to the bus waveguide. Thus, the first and last resonator in the 'series' can be expected to suffer from the largest shift.

The effect of non-degenerate resonant frequencies is shown for a 100GHz-wide third-order Chebyshev (0.2dB ripple) add/drop filter model in Fig. 2 (left and center). The plot shows an ideal response with ring loss included, but no CIFS (left); and the same filter with a +20GHz CIFS in the middle microring (middle plot). A significant degradation of the thru-port rejection is seen. In addition, the drop spectrum acquires a slight asymmetry and ripple.

On the right in Fig. 2 is the measured spectral response of a third-order add/drop filter fabricated in SiN by electron-beam lithography [5]. Based on the dimensions and materials of this filter, an expected CIFS of {-24GHz, -2GHz, -24GHz} was computed for the three rings, respectively using a vectorial CMT. This corresponds to a +22 GHz net shift for the middle ring, used above in the model for comparison. The loss in the model above (Q = 12,000) was chosen to match the experimental insertion loss, though the ring Q's were assumed equal. This assumption makes for some discrepancy as the middle ring is expected to have lower loss than its more strongly coupled neighbours, but the experimental spectrum confirms a frequency difference among microrings of ~20GHz. While this difference could be caused by slight size differences between the resonators due to fabrication, a measurement of dimensions in [5] suggests that the primary contribution to the spectrum asymmetry is due to the CIFS. Neither an asymmetric coupling nor ring loss distribution can account for an asymmetric spectrum.

Naturally, the solution is to design each resonator such that its effective frequency including CIFS in the final configuration is the design frequency. In practice, this means pre-distorting the isolated resonator frequency by the negative of the CIFS computed, by slightly redesigning each resonator to alter the frequency but maintain coupling.

In general, CIFS pre-distortion is accomplished by slightly changing the size, shape or refractive index of a resonator, or by loading it with additional dielectric structures. In the case of microrings and racetracks, this can be accomplished most simply by a change in the radius (i.e. effective path length), waveguide width or core index. Thus, the final design of a series-coupled microring add/drop filter as in [1] calls for slightly non-identical resonators with non-degenerate resonance frequencies prior to coupling.

References

1. B.E. Little, S. Chu, H. Haus, J. Foresi, J. Laine, "Microring resonator channel dropping filters," J. Lightwave Technol. **15**, 998-1005 (1997).
2. M.J. Khan, C. Manolatou, S. Fan, P.R. Villeneuve, H.A. Haus and J.D. Joannopoulos, "Mode coupling analysis of multipole symmetric resonant add/drop filters," IEEE J. Quant. Electron., **35**, 1451-1460 (1999).
3. C.K. Madsen and J.H. Zhao, *Optical Filter Design and Analysis: A Signal Processing Approach* (Wiley, 1999).
4. H.A. Haus and W.P. Huang, "Coupled-Mode Theory," Proceedings of the IEEE, (Institute of Electrical and Electronics Engineers, New York, 1991), pp. 1505-1518.
5. T. Barwicz, M.A. Popović, P.T. Rakich, M.R. Watts, H.A. Haus, E.P. Ippen and H.I. Smith, "Fabrication and analysis of add/drop filters based on microring resonators in SiN", *submitted concurrently to OFC 2004*.

Recent Advances in Thin Film Filters

Robert B. Sargent

JDS Uniphase, 2789 Northpoint Parkway, Santa Rosa, CA 95407
Email: rsargent@ocli.com

Abstract: Optical thin film filters are widely employed in optical communications systems. Important applications include narrowband filters for DWDM and gain flattening filters for EDFAs. Applications and recent advances in the technology are reviewed.

OCIS codes: (060.2340) Fiber optics components; (310.0310) Thin films.

1. Introduction

The recent rapid growth of the optical communications infrastructure has fueled significant developments in passive optical component technologies such as arrayed waveguide gratings (AWG), fiber bragg gratings (FBG), and thin film filters (TFF). In the mid-1990's TFF technology was considered mature relative to other relevant technologies, and it was not obvious to workers in the field that the technology could advance quickly enough to meet the cost and performance targets required for dense wavelength division multiplexing (DWDM) systems [1]. In the late 1990's performance improvements in TFF technology were dramatic, and the technology is presently employed in a wide range of fiberoptic network applications.

TFF is a well understood, proven technology. Design synthesis approaches for TFFs have been extensively developed [2], and design software tools are widely available. Deposition processes for fabricating TFFs have been under intensive development for decades, and energetic processes capable of producing fully dense layers are widely deployed [3, 4]. Packaging technology for TFFs has advanced significantly during the past few years. For example, JDS Uniphase has developed a laser-welded coupler package that exceeds the requirements of Telcordia GR-1221 [5].

Important performance advantages have led to the wide deployment of TFFs in optical networks. TFFs and the devices built from them can be made to have very low temperature dependence, with filter spectral responses shifting less than 0.001 nm / degree C [1, 3, 6]. Excellent spectral filtering performance can be achieved with the technology. TFFs are readily produced in high volume with high yield. The polarization dependence of TFFs is typically low (with polarization dependent loss well below 0.1 dB for many device types). When designed and fabricated appropriately, TFF-based devices have been demonstrated to be highly reliable. TFF-based modules can be designed to be upgradeable, allowing system implementers to install a modest number of channels on a fiber at a modest cost, and then add channels through upgrade ports later.

This paper reviews important recent advances in TFF technology. To illustrate the advances, several important applications are reviewed, and technology improvements that have led to improved performance for these applications are described.

2. Narrowband Filters for DWDM

TFFs were developed for DWDM applications during the mid-1990s, and have been commercially deployed in systems with channel spacings such as 200 and 100 GHz. The demonstration of filters targeted for channel spacings of 50 GHz and 25 GHz [7-9] suggest that impressive spectral profiles are possible with the technology. As DWDM networks move to narrower channel spacing and faster data transmission rates, the dispersive characteristics of TFFs become a limiting factor [10, 11]. A practical result is that narrowband TFFs designed for a square amplitude characteristic exhibit high chromatic dispersion (CD) in transmission. In the past few years several methods of mitigating this effect have been explored. One method is to employ a CD-compensating element in series with the transmitted channel of the narrowband DWDM filter [12, 13]. Tilsch et al. [8] demonstrated that the CD within the 30 GHz passband of a 50 GHz channel separation filter could be reduced from +/- 170 ps/nm to below +/- 50 ps/nm through the use of such a technique, with further improvements to +/- 5 ps/nm possible. A second method employed to mitigate CD effects is to compromise the performance of the passband, that is, to make the amplitude response of the filter less square in a controlled way, so as to achieve acceptable CD performance in the filter transmission band [11, 12, 14].

During the past few years, this second technique has been applied to commercially available filters for 100 GHz channel spacing. Figure 1 compares the measured performance of two filters, an earlier type designed with a square passband and a relatively new type designed with a slightly rounded passband to mitigate CD effects; an improvement of roughly a factor of two in CD performance is realized in this example. This new generation of filter maintains or improves on other important filter characteristics such as adjacent channel isolation and insertion loss.
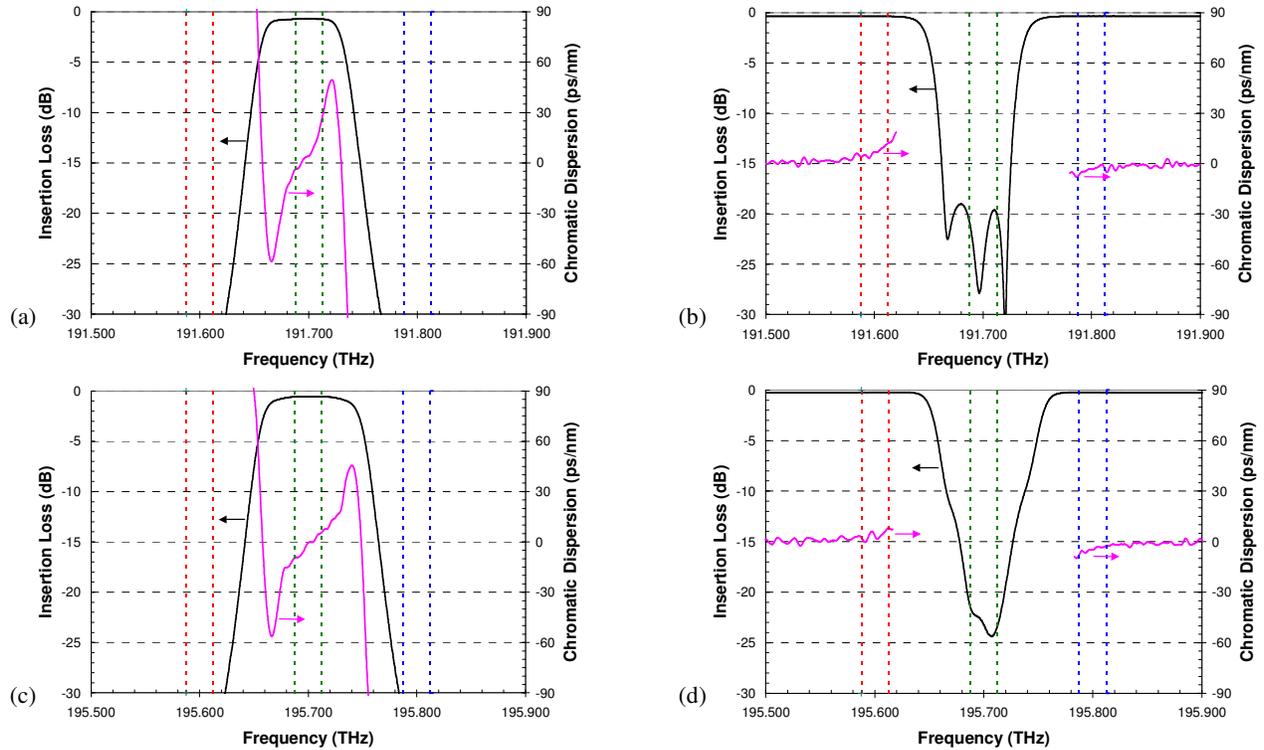
Fig. 1. (a) Measured transmission amplitude and CD of a packaged 100 GHz thin film bandpass filter with square passband; (b) Measured reflection amplitude and CD for square passband filter; (c) Measured transmission amplitude and CD of a packaged 100 GHz thin film bandpass filter developed for low CD; (d) Measured reflection amplitude and CD for low CD filter. Vertical dotted lines represent 25 GHz passbands for three adjacent channels.

3. Bandsplitting Filters

Optical network architectures often utilize bands of channels to facilitate multiplexing and demultiplexing and add/drop multiplexing. Filters that separate multiple channels from a fiberoptic stream are often called bandsplitting or "skip" filters. An example of a bandsplitting filter is the 8-skip-2 filter for 100 GHz-spaced channels, which transmits 8 channels and achieves isolation between the transmitted and reflected channels by skipping two channels. Skipping channels is undesirable, as it has the effect of reducing the available communication bandwidth. This has driven the development of filters with steeper slopes such as the 8-skip-1 filter, which skips only one channel. A convenient way to gauge the difficulty of realizing a bandsplitting filter is to determine the shape factor, which is the ratio of the isolation bandwidth to the pass bandwidth. Filters having smaller shape factors have steeper transitions between passbands and stopbands, require more cavities in the filter design, and as a result have greater physical thickness. Table 1 lists the shape factors for a number of 100 GHz bandsplitting filters; the table assumes each communication channel requires a 25 GHz passband.

Table 1: Characteristics and evolution of the availability of important 100 GHz bandsplitting filters. The pass bandwidth (PBW) is often taken as the bandwidth of the filter measured at -0.3 dB relative to the filter peak transmission, and the isolation bandwidth (IBW) often taken at –20 dB relative to the filter peak transmission.

Type	Pass BW (GHz)	Isolation BW (GHz)	Shape Factor IBW / PBW	Availability 2000 – 2001	Availability 2002 - 2003
8 skip 2	725	1275	1.76	Standard Product	Standard / Commodity
8 skip 1	725	1075	1.48		Custom Product
8 skip 0	725	875	1.21		Demonstrated [15]
4 skip 1	325	675	2.08	Standard Product	Standard / Commodity
4 skip 0	325	475	1.46		Standard Product

One recognized property of TFFs that can limit the performance of bandsplitting filters is film stress. The effects of stress become more pronounced with increasing film thickness. A typical manifestation of stress is a variation in

center passband wavelength across the filter, which leads to degraded filter performance. This effect is especially important in bandsplitting coatings owing to the large number of cavities used to achieve the required square spectral response profile. Ockenfuss et al. [15] demonstrated that film stress reduction can yield significant filter performance benefits. An 8-skip-0 filter for 100 GHz channel spacing that required 17 cavities and a total physical thickness of 94 micrometers was demonstrated. The filter was fabricated using a special low-stress process, and was shown to exceed the requirements of the 8-skip-0 application. While such filters are not yet available commercially, stress reduction and other process improvements are enhancing the performance of bandsplitting filters. Progress in the development of 4-skip-0 filters has been recently reported [16], and 8-skip-1 and 4-skip-0 filters have recently become available commercially.

4. Gain Flattening Filters

The wavelength-dependent gain intrinsic to optical amplifiers may be equalized through the use of TFFs. Early work approached the problem through the use of 2 or 3 cascaded gain flattening filter (GFF) components that together provided the correct filter function [17]. Subsequently, single element GFFs were demonstrated [18], and methods for designing single element GFFs have been described [12, 19]. The performance of a GFF is measured by its error function, defined as the difference between the measured realized filter spectrum and the intended function. For a given requirement, the error function achievable depends largely on the maximum excursion in the loss profile, but also on the precise shape profile requirement of the filter. By 2000, thin film based GFFs of the single filter type were commercially available which had error functions of typically 10% to 15% of the maximum excursion of the required filter. At present, deposition process improvements combined with the refinement and further application of modeling tools described by Tilsch et al. [18] have made possible the achievement of error functions which are often less than 5% of the maximum excursion of the GFF shape.

5. Other Applications and New Developments

Beyond the applications described thus far, TFFs have been employed in a variety of network applications including pump WDMs for EDFAs and optical supervisory channel add/drop filters. Network requirements drive the need to combine multiple functions into a single component; for example, the filtering function of a GFF for the C band may need to include a blocking or transmission requirement in the S or L band. TFFs and related technologies such as single and multiple cavity etalons have also been explored as tools for compensating fiber dispersion [20, 21, 22].

Several new developments extend TFF functionality. Recently methods for fabricating tunable filters with no moving parts using piezoelectric and thermal mechanisms have been proposed [23], and thermally tuned filters have been demonstrated [24]. TFFs have been recognized as one-dimensional photonic crystals, and recently it has been reported that certain filter designs exhibit spatial dispersion related to the superprism effect [25].

6. References

1. H. Macleod, "Advances in Thin Films," OFC 2003 Technical Digest, ThM1, pp. 520-521 (2003).
2. H. A. Macleod*, Thin Film Optical Filters*, Third Ed. (Institute of Physics Publishing, Bristol, 2001).
3. N. A. O'Brien, M. J. Cumbo, K. D. Hendrix, R. B. Sargent, and M. K. Tilsch, "Recent Advances in Thin Film Interference Filters for Telecommunications," in Proceedings of 44th Society of Vacuum Coaters Annual Conference, pp. 255-261 (2001).
4. R. B. Sargent and N. A. O'Brien, "Dielectric Materials for Thin-Film-Based Optical Communications Filters," MRS Bulletin Vol. 28, pp. 372-375 (May 2003).
5. GR-1221-CORE, Generic Reliability Assurance Requirements for Passive Optical Components, Issue 2 (Telcordia Technologies, 1999).
6. H. Takahashi, "Temperature stability of thin film narrow bandpass filters produced by ion assisted deposition," Applied Optics Vol. 34, pp. 667-675 (1995).
7. H. Hagedorn, A. Lotz, P. Pecher, and O. Treichel, "Ultra narrow band pass filters produced by plasma ion assisted deposition," Optical Interference Coatings 2001 Technical Digest, pp. WA4.1-WA4.3 (Optical Society of America, 2001).
8. M. Tilsch, C. A. Hulse, F. K. Zernik, R. A. Modavis, C. J. Addiego, R. B. Sargent, N. A. O'Brien, H. Pinkney, and A. V. Turukhin, "Experimental Demonstration of Thin-Film Dispersion Compensation for 50-GHz Filters," IEEE Photonics Technology Letters Vol. 15, pp. 66-68 (2003).
9. M. A. Scobey, R. M. Fortenberry, L. F. Stokes, W. P. Kastanis, and D. J. Derickson, "Thin film interference filters for 25 GHz channel spacing," OFC 2002 Technical Digest, ThC5, pp. 398-399 (2002).
10. G. Lenz, B. J. Eggleton, C. R. Giles, C. K. Madsen, and R. E. Slusher, "Dispersive properties of optical filters for WDM systems," IEEE Journal of Quantum Electronics Vol. 34, pp. 1390-1403 (1998).
11. K. Zhang, R. Sharps, J. Wang, E. Schwendeman, D. Dawson-Elli, and R. Faber, "Group delay and chromatic dispersion of thin-film-based, narrow bandpass filters used in dense wavelength-division-multiplexed systems," Applied Optics, Vol. 41, pp. 3172-3175 (2002).
12. A. Thelen, M. Tilsch, A. V. Tikhonravov, M. K. Trubestskov, and U. Brauneck, "Topical Meeting on Optical Interference Coatings (OIC'2001): design contest results," Applied Optics Vol. 41, pp. 3022-3038 (2002).
13. T. Noe, "Design of reflective phase compensator filters for telecommunications," Applied Optics, Vol. 41, pp. 3183-3186 (2002).
14. R. M. Fortenberry, M. E. Wescott, L. P. Ghislain, and M. A. Scobey, "Low Chromatic Dispersion Thin Film DWDM Filters for 40 Gb/s Transmission Systems," ," OFC 2002 Technical Digest, WS2, pp. 319-320 (2002).
15. G. J. Ockenfuss, N. A. O'Brien, and E. Williams, "Ultra-low stress coating process: an enabling technology for extreme performance thin film interference filters," OFC 2002 Postdeadline Papers, FA8, pp. FA8.1-FA8.3 (2002).

16. T. Ito, Y. Iida, K. Minagawa, and K. Aihara, "Optimization for CD Characteristic of Band-OADM Using 4-skip-0 100 GHz Filter," OFC 2003 Technical Digest, ThM2, pp. 521-522 (2003).

17. M. Scobey, D. E. Spock, M. E. Grasis, and J. A. Beattie, " EDFA Gain Equalization using Interference Films," NFOEC 1996 Technical Proceedings, pp. 969-972 (1996).

18. M. Tilsch, C. A. Hulse, K. D. Hendrix, and R. B. Sargent, "Design and Demonstration of a Thin-Film Based Gain Equalization Filter for C-Band EDFAs," NFOEC 2000 Technical Proceedings, pp. 390-395 (2000).

19. P. G. Verly, "Design of a robust thin-film interference filter for erbium-doped fiber amplifier gain equalization," Applied Optics Vol. 41, pp. 3092-3096 (2002).

20. M. Jablonski, Y. Takushima, K. Kikuchi, Y. Tanaka, K. Furuki, K. Sato, and N. Higashi, "Layered optical thin-film allpass dispersion equaliser for compensation of dispersion-slope of optical fibers," Electronic Letters Vol. 36, pp. 1139-1141 (2000).

21. C. K. Madsen and G. Lenz, "A Multi-channel Dispersion Slope Compensating Optical Allpass Filter," OFC 2000 Technical Digest, WF5, pp. WF5.1-WF5.4 (2000).

22. D. Moss, L. Lunardi, M. Lamont, G. Randall, P. Colbourne, S. Chandrasekhar, L. Buhl, and C. Hulse, "Tunable Dispersion Compensation at 10 Gb/s and 40 Gb/s Using Multicavity All-Pass Etalons," OFC 2003 Technical Digest, TuD1, pp. 162-163 (2003).

23. M. Lequime, R. Parmentier, F. Lemarchand, and C. Amra, "Toward tunable thin-film filters for wavelength division multiplexing applications," Applied Optics, Vol. 41, pp. 3277-3284 (2002).

24. L. Domash, E. Ma, N. Nemchuk, A. Payne, and M. Wu, "Tunable thin film filters," OFC 2003 Technical Digest, pp. 522-524 (2003).

25. M. Gerken and D. A. B. Miller, "Multilayer thin-film structures with high spatial dispersion," Applied Optics Vol. 42, pp. 1330-1345 (2003).

Beyond 80-Gbit/s-Throughput Monolithically Integrated Eight-Channel WDM Modulator module for multi-channel optical transmitter

Y. Suzaki, H. Yasaka, H. Mawatari, K. Yoshino, Y. Kawaguchi, S. Oku, R. Iga, and H. Okamoto

NTT Photonics Laboratories, NTT Corporation
3-1 Morinosato-Wakamiya, Atsugi-shi, Kanagawa Pref., 243-0198 Japan
Tel: +81-46-240-2306   Fax: +81-46-240-3186

E-mail: suzaki@aecl.ntt.co.jp

A 35-word abstract: A 10 Gbit/s x 8 ch WDM modulator module with 50-GHz channel spacing is demonstrated. The module contains only one monolithically integrated WDM modulator chip that is only 15 mm x 7 mm in size.

Introduction

Wavelength division multiplexing (WDM) systems are promising for enlarging the system throughput and functions using wavelength labels. In these systems, a large number of wavelength channels are packed into optical fibers with narrow channel spacing and each channel transports high bit rate signals. Therefore, a compact and high-speed multi-channel optical transmitter will be an indispensable component of the system. The optical transmitter can be constructed by combining a multi-wavelength light source that generates multi-channel lights simultaneously and a compact and high-speed multi-channel modulation component that can individually modulate the WDM lights from the light source. Multi-wavelength light sources have been demonstrated by using mode-locked lasers [1], [2]. The wavelength control of these light sources is easy because the wavelength (or frequency) spacing can be precisely defined by the applied electrical frequency.

The multi-channel modulation component can be fabricated in a monolithic integration. The advantages of monolithic integration are that the footprint of the module can be reduced compared with discrete modules and that optical alignment points among devices can be drastically reduced, which could potentially result in low assembly cost. Therefore, many monolithic-integrated devices have been demonstrated [3]-[6]. So far, we have demonstrated a 2.5-Gbit/s monolithically integrated multi-channel WDM modulator [7]. This WDM modulator comprised a 25-GHz-channel-spacing AWG, and electro-absorption modulator (EAM) and semiconductor optical amplifier (SOA) arrays and was fabricated by the butt-joint selective area growth and dry etching techniques. Further high throughput will be necessary in order to cope with the explosive increase of data traffic.

In this paper, for further enhancement of the total throughput, we present an eight-channel and 50-GHz-channel-spacing monolithically integrated multi-channel WDM modulator module. An 80-Gbit/s-throughput (10Gbit/s x 8 ch) operation has been successfully obtained with good eye opening and good bit error rate (BER) performance. We confirm that the electrical and optical crosstalks are negligibly small in simultaneous operation for all ports. We also show 100-Gbit/s throughput operation by evaluating 12.5-Gbit/s eye diagrams for all eight channels.

Device and module structures

Figure 1 shows the functional diagram and a photographic view of the WDM modulator chip. The circuit consists of 50-GHz channel spacing AWGs for multiplexing and demultiplexing and eight sets of EAMs and SOAs. Incident multi-wavelength CW lights multiplexed into an optical fiber are split into the corresponding WDM channels by the AWG for demultiplexing. Next, the lights travel through the SOAs, which compensate for the insertion loss of the AWG and equalize the output power, and enter the EAMs, where they are individually modulated by 10-Gbit/s signals. The modulated lights are launched into the

AWG for multiplexing, where they are combined into one output port. The details of the chip fabrication process are described in Ref. [8]. The chip size is 15 mm x 7 mm.

The optical module has a butterfly-type configuration with one optical input and one optical output port at the opposite sides as shown in Fig 2. The monolithic integration of the components, especially the AWG, reduces optical alignment points for the fiber coupling, which means the same packaging method as that of a conventional two-port optical module can be used. The package is 45 mm x 22 mm x 8.5 mm in size.

Module characteristics

Figure 3 shows the output spectra of the module when all channels are in operation. The SOA injection currents were 100 ~ 150 mA and the incident powers of the CW lights were set to +5 dBm. We obtained the maximum output power of around -17 dBm, and the control of SOA currents can easily equalize the output power. The EAM array performed at a high extinction ratio of more than 25 dB in all channels at a reverse voltage of 3 V.

Figure 4 shows the BER performances for all channels (Circles) and a typical eye diagram for 10-Gbit/s NRZ signals (PRBS: 2^{23}-1) when each channel is in operation. The DC injection current into the SOA was 150 mA and the driving voltage to the EAM was 3 V peak-to-peak with the DC reverse bias of 2.0 V. The power of the incident light was +5 dBm. Good eye opening and an averaged minimum received power of –37 dBm (@BER=10^{-10}) were achieved, and the power variation among channels is less than 1 dB. This means that the fabrication uniformity of the monolithically integrated chip is excellent.

The suppression of both optical and electrical crosstalk is an issue for such a multi-channel component. To evaluate the crosstalk, we measured the BER of the center channel (ch. 4) when the other channels into which a 10-Gbit/s NRZ data was supplied were simultaneously ON. The measurement conditions are the same as the above and the output signals with different channel signals were demultiplexed by a silica-based AWG filter to evaluate the BER. No sensitivity degradation in BER performance was observed as shown in Fig. 4 (triangles). This means that this module is promising for the multi-channel modulation component of DWDM systems.

Finally, we evaluated the 12.5 Gbit/s operation for all channels. All channels show clear eye opening (a typical eye diagram for ch. 4 is shown in Fig. 5), which indicates that the throughput can reach to 100-Gbit/s.

Conclusion

We demonstrate an eight-channel WDM modulator module comprising a monolithically integrated circuit with 50-GHz spacing AWGs, and SOA and EAM arrays. High-throughput operation of beyond 80 Gbit/s was successfully demonstrated and low crosstalk among channels was obtained. This module together with a multi-wavelength optical light source is a promising candidate for a multi-channel optical transmitter for WDM systems.

References
[1] H. Sanjoh et al., IEEE Photon. Technol. Lett., vol. 9, no. 6, pp. 818-820,1997.
[2] K. R. Tamura et al., OFC 2001, TuJ5, Anaheim, USA.
[3] M. K. Smit, et al., IEEE J. Sel. Top. Quantum Electron., vol. 2, no. 2, pp. 236-250, 1996.
[4] M. Zirngibl, et al., Electron. Lett., vol. 30, no. 9, pp.701-702, 1994.
[5] S. Khalfallah, et al., ECOC 2001, Th.B.4.PD3, Amsterdam, Holland.
[6] N. Kikuchi, et al., OFC 2002, TuF4, Anaheim, USA.
[7] Y. Suzaki et al., OFC 2003, TuG4, Atlanta, USA.
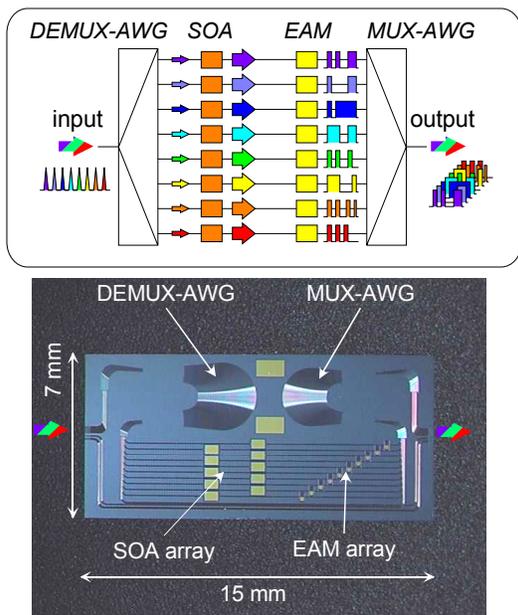[8] Y. Suzaki et al., IPRM 2002, A8-4, Stockholm, Sweden.

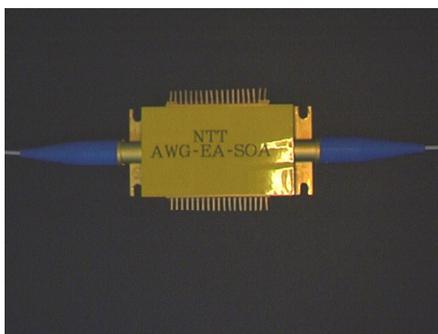Figure 1. Functional diagram (top) and photo of the chip (bottom).

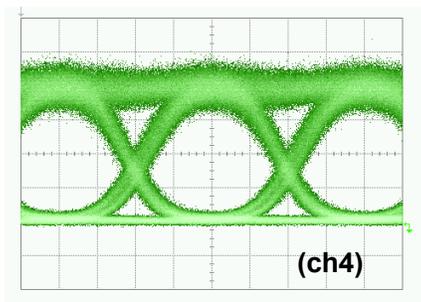Figure 2. Photo of the module.

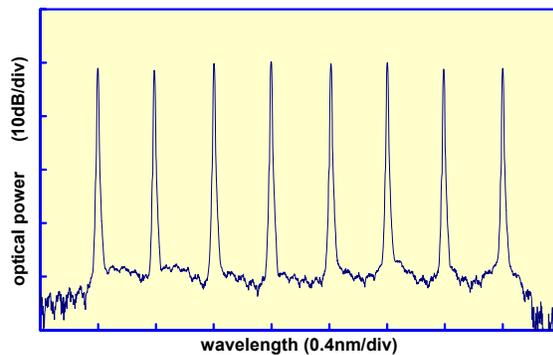Figure 5. Typical eye diagram for 12.5-Gbit/s operation.

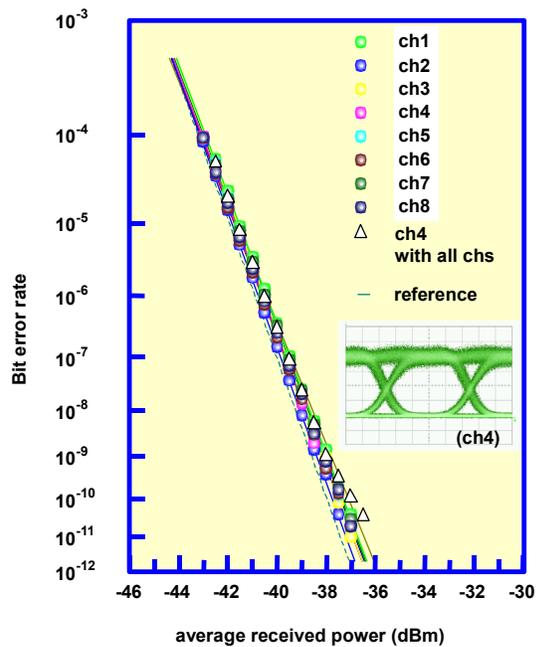Figure 3. Output spectra of the module.

Figure 4. BER performance and typical eye diagram (inset)

State-of-the-art performance of widely tunable modulated grating Y-branch lasers

Jan-Olof Wesström, Gert Sarlet, Stefan Hammerfeldt, Lennart Lundqvist, Peter Szabo, Pierre-Jean Rigole
Syntune AB, Danmarksgatan 46, S-164 40 Kista, Sweden
Tel: +46 8 750 65 24, Fax: +46 8 750 65 23, E-mail: jan-olof.wesstrom@syntune.com

Abstract: Novel monolithic tunable laser diode with wide tuning range (191.05-196.80 THz), high side-mode suppression ratio (> 40 dB), high output power (> 13 dBm) and low power variation (< 1.5 dB) without additional amplification.
©2003 Optical Society of America
OCIS codes: (140.3600) Lasers, tunable; (140.5960) Semiconductor lasers; (060.2380) Fiber optics sources and detectors

1. Introduction

Widely tunable lasers have been in the focus of the photonics industry for many years now, since they are considered key enablers for intelligent all-optical networks that provide carriers with greater flexibility, faster provisioning, and, crucial in the current economic environment, much lower costs. A wide range of solutions have been proposed, from miniaturized external cavity lasers [1], through micro-mechanically tuned vertical cavity surface emitting lasers [2], to thermally tuned DFB arrays [3]. Only one class of tunable lasers can however be monolithically integrated with a modulator, which is required to achieve a low-cost transmitter module, and provide the fast tuning (switching time ~10 ns) required for future systems based on optical burst mode switching. These are the monolithic electronically tuned distributed Bragg reflector lasers employing modulated grating reflectors with multiple reflectivity peaks to achieve wide tuning. Examples are the sampled grating DBR (SG-DBR) laser [4] and the grating coupler with rear sampled grating reflector (GCSR) laser [5]. In this paper we present the first experimental results on a new and improved tunable laser diode in this class, the modulated grating Y-branch (MG-Y) laser (Fig. 1) [6-7].
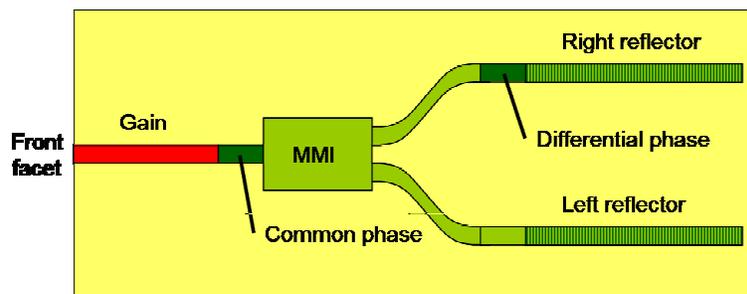

Fig. 1. Schematic lay-out of the modulated grating Y-branch (MG-Y) laser.

The MG-Y is similar to the SG-DBR in that it uses the Vernier effect to achieve wide tuning with two multi-peak reflectors. One disadvantage with the SG-DBR laser is that the output light has to pass through the front reflector, in which significant free carrier absorption occurs when current is injected. As a result, the output power of a SG-DBR laser varies significantly with tuning (> 3 dB). The MG-Y is comparable to the GCSR laser in the sense that it has all tuning sections on the same side of the gain section, such that the light can exit the cavity without absorption, enabling higher and more even output power across the tuning range. Instead of using the Vernier effect, the GCSR laser uses a widely tunable coupler transmission peak to efficiently select one reflector peak for lasing. The main disadvantage of the GCSR is that the chip is rather long, which reduces the cavity mode spacing and yields somewhat lower side-mode suppression ratio.

2. Device design and fabrication

Conceptually, one main difference between the SG-DBR laser and the MG-Y laser is that for the MG-Y the super-mode selection is performed by an addition of the complex amplitudes of the reflectivities instead of a multiplication. Since the addition is sensitive to the phase difference between the reflections, the shape of the aggregate reflection spectrum is not self-evident. At first sight, one would expect to need a differential phase control in order to match the phases of the reflections from left and right reflector. However, as described in [7], when properly designed the addition suppresses the adjacent peaks strongly although these side peaks overlap. By applying a set of design rules for the reflectors, one can ensure that the same differential phase will apply for all operation points in the main repeat mode, where reflectivity peaks of the same order are aligned, i.e. where peak n from the left reflector is aligned with peak n from the right reflector (n = -4, -3, …, +4, +5) [7]. If, on top of that, during fabrication care is taken not to introduce any significant asymmetry between the waveguides in both arms of the Y-branch, the initial differential phase will be 0 and no differential phase tuning will be required at all for operation points in the main repeat mode. The results below will show that this was successfully achieved in the first fabricated batch of MG-Y lasers.

In the current design of the MG-Y laser, the light is split by the use of a 60 µm long, 7 µm wide multi-mode interferometer (MMI). Then 115 µm long S-bends with a 255 µm radius of curvature are used to increase the separation between the waveguides. Each arm ends with a 500 µm long multi-peak reflector with an effective coupling coefficient of 30 cm^{-1}. In one arm there is an 80 µm long differential phase section that can be used to adjust the phase difference between the reflections. A common phase section of the same length is used to align the cavity mode with the reflector peaks. The device is manufactured as an InP/InGaAsP buried hetero structure laser, with a 400 µm multi-quantum-well gain section butt-joined to the passive sections made in a 0.35 µm thick InGaAsP layer with a photo-luminescence wavelength of 1.39 µm. The fabrication process is essentially the same as that of a standard DBR laser, with 5 MOVPE steps. Stitching error free gratings are fabricated in the two reflectors by electron beam lithography and wet chemical etching. In order to boost the output power, a low-reflectivity coating is applied to the front facet after cleaving, reducing the power reflectivity from 28% to a few % and thus enhancing the slope efficiency of the laser.

3. Device performance

Fig. 2 reveals a map of the output frequency as a function of the tuning currents in both reflectors for a typical device, measured at a constant gain current of 150 mA, and a common phase current of 0 mA. For a vast majority of devices from the first batch no differential phase tuning is needed to achieve in-phase addition of the reflections when reflectivity peaks of the same order from both reflectors are aligned, illustrating the robustness of the design. Consequently, the differential phase section can be eliminated in future versions, and only 4 sections need to be controlled to achieve full power and frequency control, i.e. the same number of controls as a SG-DBR or GCSR laser.

When devices are fully characterised in order to determine the reflector and phase currents required to tune the laser to the channels on the ITU-grid in the C-band, very regular patterns are obtained, as illustrated by Fig. 3. This implies that the devices have no spurious reflections at butt-joints and other interfaces. Tuning currents are low, less than 16 mA, which is important for fast switching of the lasers since this results in reduced thermal transients when changing channel. The lasers can be tuned from 191.05 THz to 196.80 THz with side-mode suppression ratios of more than 40 dB (Fig. 4). Fig. 5 shows the front facet output power at a gain current of 150 mA and a submount temperature of 25°C for the operation points in Fig. 3. The average output power is about 14 dBm, and the variation is only 1.2 dB across the depicted tuning range of 5.8 THz.

4. Conclusion

The first batch of MG-Y lasers manufactured within the EU-funded project IST-2000-2844 NEWTON sets a new standard for monolithic widely tunable laser diodes. Without additional amplification, the MG-Y lasers yield higher output power (more than 13 dB across the tuning range from 191.05 to 196.80 THz), and significantly lower output power variation (below 1.5 dB) than SG-DBR lasers. The side-mode suppression ratio is higher than that of GCSR lasers, above 40 dB for all operation points. Also, it was proven that the differential phase section can be eliminated in future versions, and only 4 sections need to be controlled to achieve full power and frequency control.
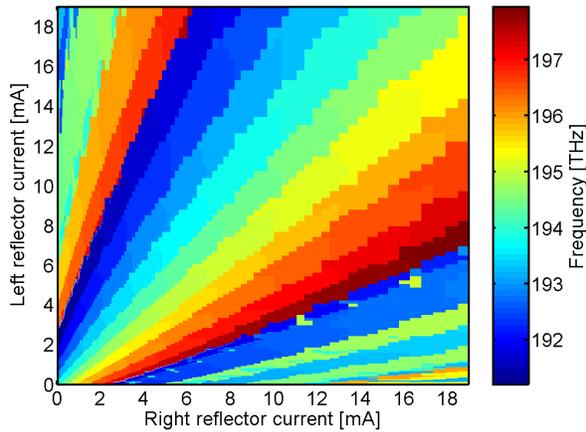
Fig. 2. Measured map of output frequency as a function of left and right reflector currents. Gain current: 150 mA, common phase current: 0 mA, differential phase current: 0 mA.
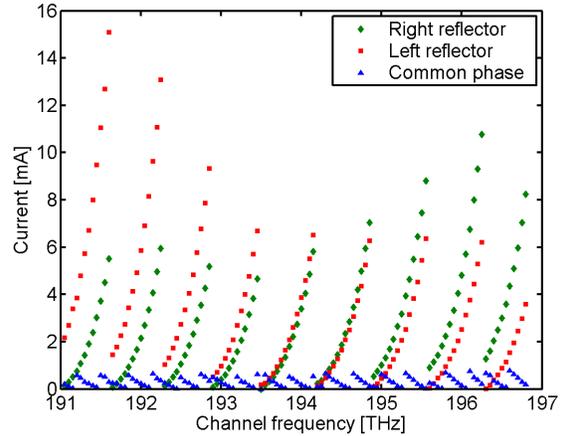

Fig. 3. Tuning currents for ITU channels from 191.05 THz to 196.80 THz. The differential phase section is not used.
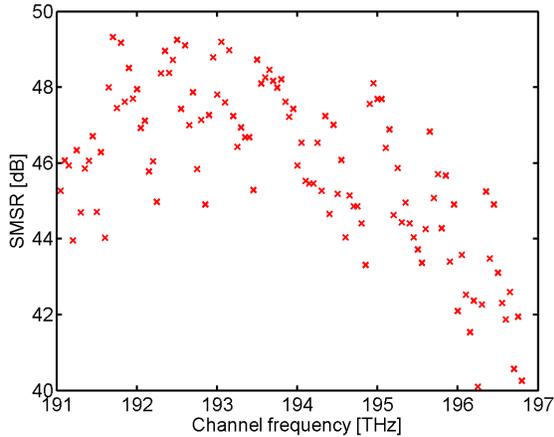

Fig. 4. Side-mode suppression ratio for ITU channels from 191.05 THz to 196.80 THz.
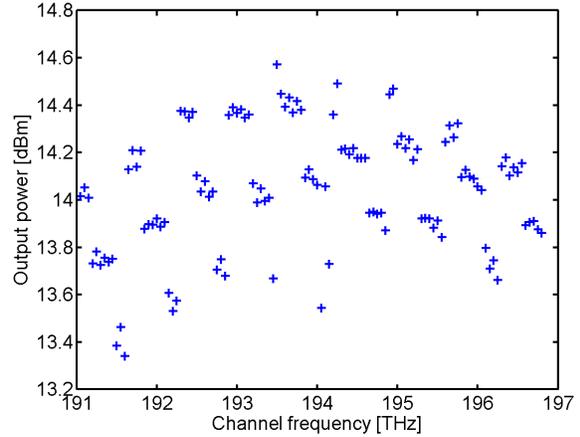

Fig. 5. Front facet output power for ITU channels from 191.05 THz to 196.80 THz at a constant gain section current of 150 mA.

5. References

[1] J.D. Berger, Y. Zhang, J.D. Grade, H. Lee, S. Hrinya, H. Jerman, "Widely tunable external cavity diode laser based on a MEMS electrostatic rotary actuator," in Proceedings Optical Fiber Communication Conference 2001, (Optical Society of America, Washington, D.C., 2001), vol. 2, paper TuJ2.

[2] C.J. Chang-Hasnain, "Tunable VCSEL," IEEE Journal of Selected Topics in Quantum Electronics **6**, 978-987 (2000).

[3] B. Pezeshki, E. Vail, J. Kubicky, G. Yoffe, S. Zou, J. Heanue, P. Epp, S. Rishton, D. Ton, B. Faraji, M. Emanuel, X. Hong, M. Sherback, V. Agrawal, C. Chipman, and T. Razazan, "20-mW widely tunable laser module using DFB array and MEMS selection," IEEE Photonics Technology Letters **14**, 1457-1459 (2002).

[4] V. Jayaraman, Z.-M. Chuang, and L.A. Coldren, "Theory, design and performance of extended tuning range semiconductor lasers with sampled gratings," IEEE Journal of Quantum Electronics **29**, 1824-1834 (1993).

[5] M. Öberg, S. Nilsson, K. Streubel, L. Bäckbom, and T. Klinga, "74 nm wavelength tuning range of an InGaAsP/InP vertical grating assisted codirectional coupler laser with rear sampled grating reflector," IEEE Photonics Technology Letters **5**, 735-738 (1993).

[6] G. Sarlet, J. Buus, and R. Baets, "Widely wavelength tunable integrated semiconductor device and method for widely wavelength tuning semiconductor devices," European Patent Application, no. EP 1094574, filed October 18, 1999, published April 25, 2001.

[7] J.-O. Wesström, S. Hammerfeldt, J. Buus, R. Siljan, R. Laroy, and H. de Vries, "Design of a widely tunable modulated grating Y-branch laser using the additive Vernier effect for improved super-mode selection," in Proceedings IEEE International Semiconductor Laser Conference 2002, (Institute of Electrical and Electronics Engineers, New York, 2002), paper TuP16, pp. 99-100.

A high power, broadband tuneable laser module based on a DS-DBR laser with integrated SOA

D J Robbins, G Busico, L Ponnampalam, J P Duck, P J Williams, R A Griffin, A J Ward, D C J Reid, N D Whitbread and E Barton

Bookham Technology plc, Caswell, Towcester, Northants, NN12 8EQ, UK

dave.robbins@bookham.com;

B Reid and K Kasunic

Bookham Technology plc, Kanata,1-10 Brewer Hunt Way Ottawa, K2K 2B5,Canada

Abstract: A high power, broadband tuneable laser module operating over the C-band is presented which is based upon a monolithically integrated DS-DBR tuneable laser and semiconductor optical amplifier. These modules have been calibrated to achieve 80 channels at 50GHz spacing with minimum channel powers of 13.5dBm and SMSR greater than 40dB. RIN and linewidth measurements confirm that feedback from the SOA has minimal effect on the tuning performance of the DS-DBR.

1. Introduction

The advantages of tuneable lasers in telecommunications systems have been discussed at length. However, to achieve the breakthrough of displacing the incumbent single frequency DFB technology equivalent performance and cost are required. With state-of-the-art epitaxy and fabrication technology, very high uniformity of device coupled to high wafer throughput can be achieved. Consequently the emphasis is on designs with uniform and predictable channel to channel performance with sufficient output power to guarantee high yield with minimal test time in module assembly.

In this paper, results from a monolithic broadband tuning device based on the Digital Supermode (DS) DBR laser with integrated semiconductor optical amplifier (SOA) are described for the first time. Module results for this new chip have been obtained, which show minimum fibre coupled channel powers of +13.5dBm.

Tuneable lasers offer significant reductions in system costs through sparing and inventory management. The tuneable laser described here is realised in a robust, monolithic semiconductor laser technology capable of covering the whole of the C-band with a single device. As described in [3], co-packaging of the laser and modulator provides a cost effective solution giving a considerably reduced footprint compared to discrete components and also eases assembly. Furthermore, a high level of functionality can be integrated into the transmitter [3] with no adverse impact to the high level of performance.

The operation of a monolithic, broadband tuning DS-DBR laser has previously been described [1,2]. Here an improved laser design has been implemented which utilises the chirped front grating structure introduced in [3], and an integrated SOA to achieve improved output powers.

2. Laser Design and Characterisation

The integrated DS-DBR - SOA laser (fig. 1) is a surface ridge device, fabricated using conventional InP processing. It has fundamentally five sections. The gain section provides the necessary optical amplification and the phase section enables continuous tuning via adjustment of the optical cavity length. The front tuning section is a linearly chirped holographic Bragg grating and the rear section has an e-beam written phase grating reflector that provides a sharp and flat comb reflectance response. The continuous linear chirp of the 250μm front grating over the bandwidth of 70nm confers improved modal discrimination. Lastly, the integrated SOA is seen at the top of the figure.

The basic DS-DBR structure is capable of in excess of 40mW ex-facet powers in the free running condition. The integrated SOA is therefore required to run at high input power and low gain (~3-6dB). The SOA section in these devices is therefore short (300μm) and running in saturation mode. Minimising facet feedback is critical to the

device design. In order to prevent significant injection of an amplified return wave into the DS-DBR, which could disrupt the tuning characteristics, an angled output facet was used in conjunction with an anti-reflective coating.
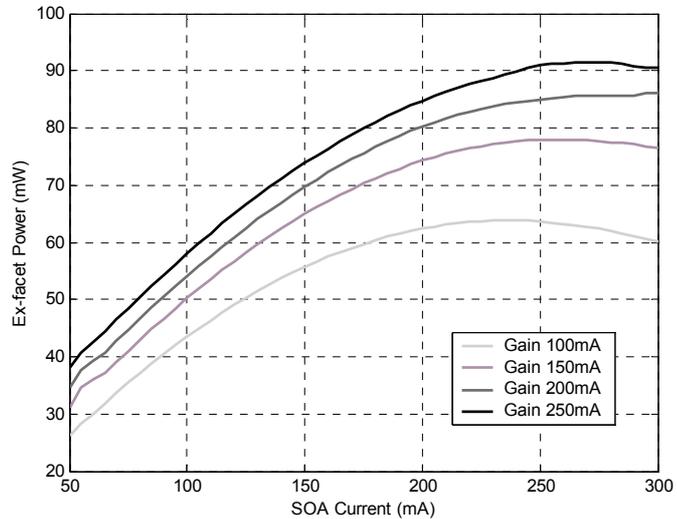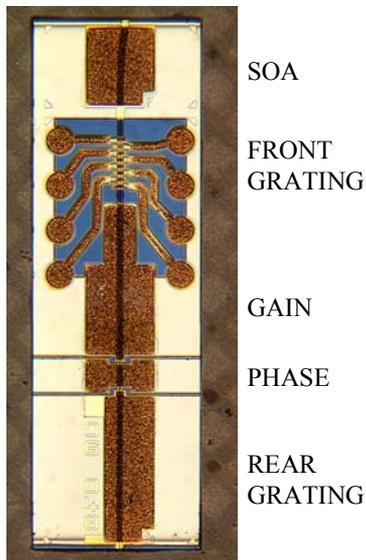

SOA

FRONT GRATING

GAIN

PHASE

REAR GRATING

Fig. 1. DS-DBR laser chip.

Fig. 2. Ex-facet chip powers in free running mode as a function of SOA current.

Free running (no tuning current) powers in excess of 100mW have been obtained from these devices. The result in fig. 2 above shows the trade-off between gain current in the DS-DBR and amplifier current. Typically, 200mA in the gain section and 150mA in the SOA provides 70mW ex-facet.

3. Tuning Characteristics

In operation the tuning of this device is equivalent to that of an integrated set of 3-section DBR lasers. Narrowband wavelength tuning is achieved by scanning the rear grating current. Continuous tuning can then be arranged by using the phase section for longitudinal mode tracking. This tuning characteristic is evident in fig. 3, which shows five supermodes. The front and rear current selections are plotted on a non-linear scale which linearises the required tuning trajectory across the supermode. An example of the 3-section like rear-phase tuning plane is plotted in fig. 4. The thick sloping line in fig. 3 corresponds to the zero phase current axis of fig. 4. The combination of non-critical front current pair selection and 3-section like tuning map leads to fast and efficient calibration of the device.
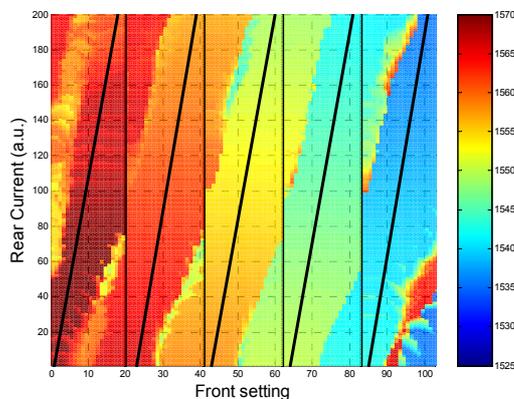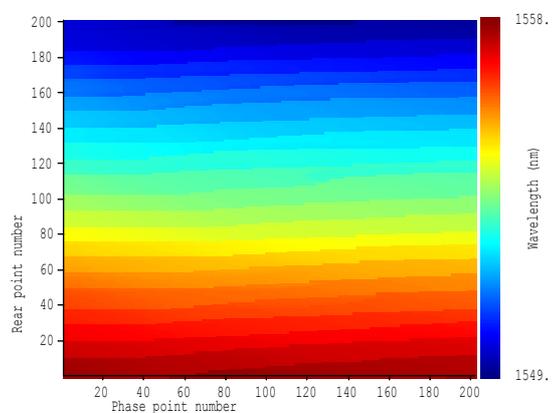

Fig. 3. Wavelength tuning map.

Fig. 4. An example of a rear-phase tuning plane.

4. Module Characterisation

26-pin butterfly packages were assembled and calibrated for 80 channels of the ITU grid; spaced at 50GHz. In fig. 5a the SMSR for each channel is plotted, where channel 1 is at 191300GHz and channel 80 at 195950GHz. The associated power variation for a SMSR >40dB is plotted in fig. 5b. Power variation across the channels was contained within 2.5dB and a minimum power of 13.5dBm achieved across the whole band. Note that this result was obtained at fixed SOA (150mA) and gain currents (200mA), with no active levelling of the power.
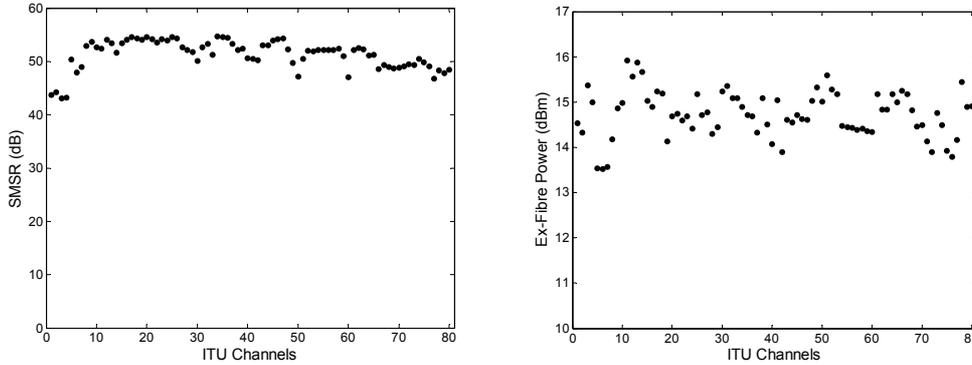
Fig. 5. (a) Side mode suppression ratio (SMSR), (b) Fibre coupled power.

5. RIN and Linewidth Measurements

RIN and linewidth measured for each of the 80 channels are plotted in fig. 6. To evaluate RIN, the noise power in an OC-192 bandwidth for each unmodulated channel launched directly into the photoreceiver was measured. Deconvolving thermal and shot noise provides an effective RIN value, typically ~150 dB/Hz, shown in fig. 6.

The ratio of average intensity to noise standard deviation in an OC-192 bandwidth provides an accurate indication of additional power penalties due to laser linewidth in a transmission experiment. Results demonstrated an output SNR > 40dB for nearly all channels, ensuring minimal impact on transmission performance. To provide an effective linewidth estimate, the measured noise was compared with the theoretical prediction for a laser with Lorentzian lineshape. As shown in fig. 6, the majority of channels have an intrinsic linewidth < 1MHz, providing transmission performance comparable to high-quality DFB sources for external modulation [4].
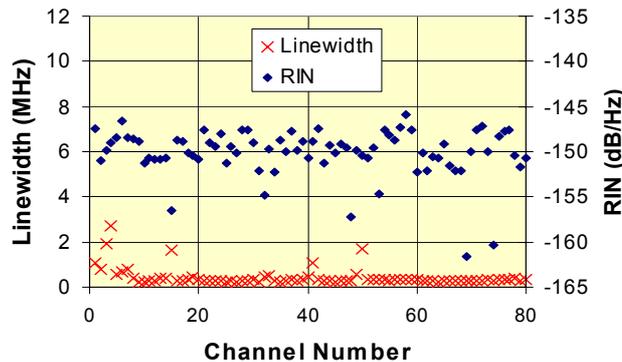
Fig. 6. (a) Linewidth for each channel, (b) RIN for each channel.

References

1. G Busico, N D Whitbread, P J Williams, D J Robbins, A J Ward and D C J Reid 'A widely tuneable Digital Supermode laser with high SMSR' Proc ECOC 2002 Copenhagen, Paper 3.3.2.
2. A J Ward, D J Robbins, G Busico, N D Whitbread, P J Williams, J R Rawsthorne, 'Modelling of phase grating based wideband tuneable lasers with simplified quasi-diugital wavelength selection' IEE (J) **150(2)** 199-203 (2003).
3. D J Robbins, J P Duck, L Ponnampalam, G Busico, R A Griffin, D C J Reid, P J Williams, A J Ward, N D Whitbread and A C Carter. 'Co-packaging of monolithic, full C-band tuneable lasers with GaAs modulators for 10Gbps transmitters' Accepted for ECOC 2003 Rimini, Italy.
4. R A Griffin, G Busico, J Duck, L Ponnampalam, D J Robbins and N D Whitbread. 'Suitability of tunable multi-section DBR lasers for advanced transmission formats' Accepted for ECOC 2003 Rimini, Italy.

10 Gb/s Mach-Zehnder modulator integrated with widely-tunable sampled grating DBR Laser

Y. A. Akulova, G. A. Fish, P. Koh, P. Kozodoy, M. Larson, C. Schow,
E. Hall, H. Marchand, P. Abraham, L. A. Coldren

Agility Communications, Inc., 475 Pine Ave, Santa Barbara, CA 93117
yakulova@agility.com

Abstract: We report on a sampled grating DBR laser monolithically integrated with a Mach-Zehnder modulator and a semiconductor optical amplifier. Transmission over 100 km of standard fiber at 10 Gb/s is demonstrated across 30 nm tuning range.
© 2003 Optical Society of America
OCIS codes: (250.5300) Photonic integrated circuits; (060.2330) Fiber optics communications

1. Introduction

A compact, high-performance widely-tunable integrated laser/modulator chip is a key component of a tunable transmitter that can dramatically lower the barriers to deployment and operation of high capacity DWDM networks. Several tunable laser technologies with integrated electroabsorption (EA) modulator operating at a bit rate of 2.5 Gb/s and beyond have been demonstrated [1-3]. Integrated transmitters based on EA-modulators although successfully deployed in metropolitan networks have received only limited acceptance in long-haul transmission systems at 10 Gb/s. The main limitations of the EA-modulator are inherent wavelength dependence of extinction ratio (ER) and chirp and trade-off between these characteristics and insertion loss. In contrast to EA-modulators, Mach-Zehnder (MZ) modulators offer the capability of precise control over chirp and extinction ratio over wide wavelength range without introducing excess loss [4]. Co-packaging of a tunable laser with a lithium niobate or III-V MZ modulator is being widely pursued by component manufactures to minimize cost and size of tunable transmitters [5]. The advantage of the co-package approach is the possibility to select laser and modulator chip characteristics independently and to ensure good optical and electrical isolation between the laser and modulator. However, further reduction of package complexity, cost, and size is achievable only through monolithic integration of a laser and a MZ modulator. Reports on a monolithically integrated III-V MZ modulator with a very narrowly-tunable gain-coupled DFB laser have demonstrated feasibility of integration and acceptable system performance at 2.5 and 10 Gb/s [6].

In this paper we discuss the design and performance of a widely tunable transmitter chip based on a Sampled Grating Distributed Bragg Reflector (SG-DBR) laser monolithically integrated with a semiconductor optical amplifier (SOA), and a Mach-Zehnder modulator (MZM). Negative and zero chirp of the transmitted signal were demonstrated by adjusting the drive voltages for two arms of MZM. Error-free transmission at 10 Gb/s for 100 km of standard single mode fiber over 30 nm wavelength range has been demonstrated for the first time for a widely-tunable laser monolithically integrated with a modulator.

2. Device design and fabrication

As illustrated in Fig. 1, the device consists of a four-section SG-DBR laser, an SOA, and a MZM, all integrated on the same InP chip. The integrated SOA compensates on-state modulator loss and cavity losses caused by free carrier absorption in the tuning sections and allows wavelength independent power leveling, beam blanking during wavelength switching, and variable optical attenuator functionality. The MZ modulator consists of two multi-mode interference (MMI) sections with curved waveguides and 400 um long lumped electrodes. The integration of the laser and SOA active regions with the tuning and modulator sections of the device has been accomplished by using an offset quantum-well structure [7]. In this simple integration technology the active region of the modulator uses the same bulk quaternary waveguide as the tuning sections of the laser. The composition of the bulk waveguide can be optimized to achieve high tuning efficiency for the laser and a target V_π over the required wide spectral bandwidth for the modulator. The device is fabricated using shallow-ridge technology to ensure low optical reflections as compared to the deep-ridge structures due to reduced index step between optical waveguides and MMI

sections [8]. An angled waveguide and wide-band anti-reflection coating at the output of the device were used to suppress the facet feedback.
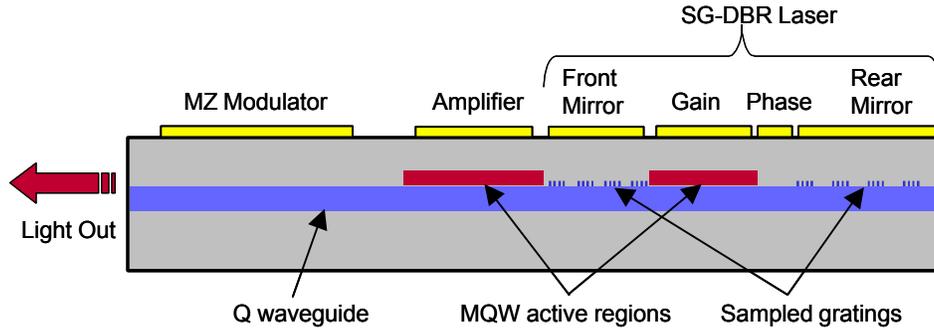

Fig. 1. Schematic of SG-DBR laser integrated with SOA and MZ modulator.

3. Results and discussion

The fabricated devices were mounted on ceramic carriers with co-planar waveguides and integrated matching resistors. For transmission measurements the chip-on-carrier was packaged into a cooled butterfly module with a co-planar RF input.

The output power vs. wavelength for a SG-DBR-SOA-MZM chip is shown in Fig. 2a). For this measurement the nominally π-phase shifted MZM is biased to produce differential phase shift of 0 radians between the two arms. The integrated chips are capable of producing more than 15 mW of power across 40 nm tuning range in the C-band. Figure 2b) shows normalized transmission characteristics for a packaged SG-DBR-SOA-MZM chip at three wavelength across C-band. DC ER in excess of 20 dB is achieved with less than 3.3 V. In single-ended drive configuration RF ER of 12 dB was measured across 40 nm tuning range with less than 3 V peak-to-peak modulation voltage (Fig. 2c).

The key for achieving uniform transmission performance of the integrated SG-DBR-SOA-MZM transmitter over wide wavelength range is in eliminating optical and electrical crosstalk and precise control of the transient chirp of the modulator. Measurements of the time-resolved chirp characteristics of the integrated chips confirmed that extrinsic chirp components due to optical feedback or electrical crosstalk are completely eliminated. The remaining chirp component is transient chirp determined by a MZM design and drive conditions. The transient chirp of p-i-n InP MZ modulator is a function of electrooptic properties of active material, splitting ratio of the two MMI sections, the differential phase shift between two arms, and the format of the modulation voltages applied to each arm of the modulator [9]. These features provide flexibility of optimizing device performance for zero or negative chirp over wide wavelength range. Figure 2c) shows wavelength dependence of the effective α-parameter extracted from the time-resolved chirp characteristics in a 3 dB region of the most transparent state of the modulator in single-ended drive configuration. Uniform chirp of -0.74+/- 0.1 is maintained across the tuning range.

Figure 3a) shows output and transmitted eye diagrams for dual- and single-ended drive conditions at 10 Gb/s for a π-shifted MZM. Maximum peak-to-peak modulation voltage for 12 dB RF ER across the C-band is 1.5 and 3 V for dual- and single-ended drive, respectively. The dual-drive condition results in "zero" chirp configuration, while single-ended operation results in "negative" chirp. Wide open eye diagrams after 50 km ("zero" chirp) and 100 km ("negative" chirp) of standard non-dispersion shifted fiber indicate that the integrated chips are capable of meeting stringent requirements for 10 Gb/s transmission. The back-to-back and 100 km BER curves were measured for negative chirp configuration for three wavelength across C-band. The lowest wavelength for this measurement was limited to 1535 nm by the tunable bandpass filter. The BER data presented in Fig. 3 b) shows error free transmission for 1600-1800 ps/nm dispersion for 1535-1563 nm wavelength range. Evaluation of dispersion penalty for longer transmission distances is currently in progress.

4. Summary

In summary, we have demonstrated a widely-tunable, 10 Gb/s transmitter chip based on a SG-DBR laser monolithically integrated with a SOA and MZ modulator. *RF* extinction ratio > 12 dB with less than 3 V modulation

voltage and negative chirp across a 40 nm tuning range have been achieved. Error-free transmission at 10 Gb/s has been demonstrated for 100 km of standard single mode fiber.
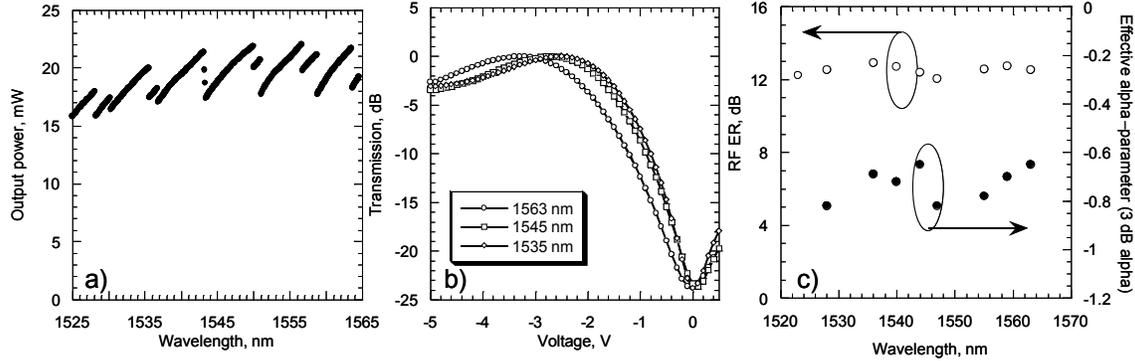

Fig. 2. a) Unleveled SG-DBR-SOA-MZM output power across the tuning range. b) Normalized transmission characteristic for three wavelengths. c) RF ER and 3 dB alpha parameter in single-ended drive configuration across the tuning range.
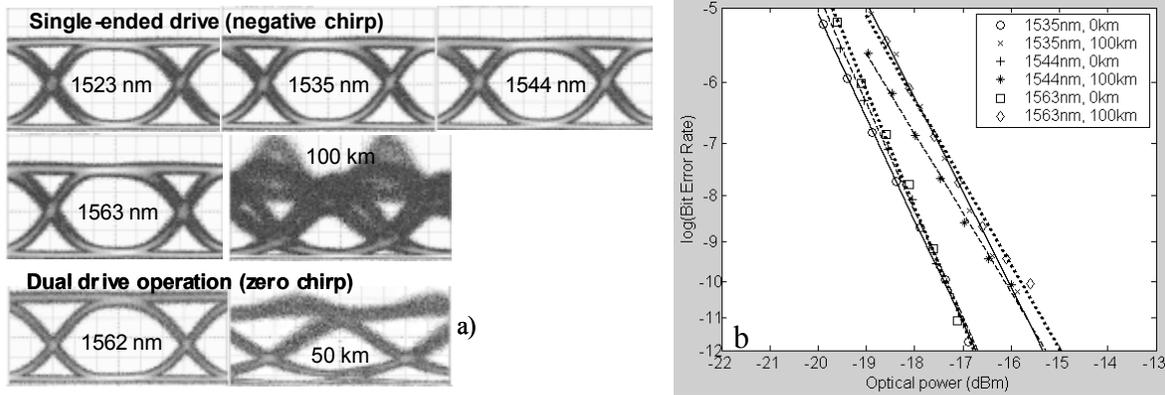

Fig. 3. a) Output eye diagrams and eye after fiber in single and dual drive configurations. b) Bit error rate curves for 0 and 100 km of standard single-mode fiber spans for three different wavelengths (10 Gb/s NRZ, 2^{21}-1 PRBS).

5. References

[1] J.E. Johnson, L.J.-P. Ketelsen, D.A. Ackerman, Zhang Liming, M.S. Hybertsen, K.G. Glogovsky, C.W. Lentz, W.A. Asous, C.L. Reynolds, J.M. Geary, K.K.; Kamath, C.W. Ebert, M. Park, G.J. Przybylek, R.E. Leibenguth, S.L. Broutin, and J.W. Stayt, Jr, "Fully stabilized electroabsorption-modulated tunable DBR laser transmitter for long-haul optical communications ", IEEE J. Select. Topics Quantum Electron., **7**, 168 -177 (2001).
[2] T. Marimoto, K. Yashiki, K. Kudo, and T. Sasaki, "Wavelength -selectable microarray light sources for DWDM photonics networks", IEICE Trans. Electron., **E85-C**, 982-989 (2002).
[3] Y.A. Akulova, G.A. Fish, Ping-Chiek Koh, C.L. Schow, P. Kozodoy, A.P. Dahl, S. Nakagawa, M.C. Larson, M.P. Mack, T.A. Strand, C.W. Coldren, E. Hegblom, S.K. Penniman, T. Wipiejewski, L.A. Coldren, "Widely tunable electroabsorption-modulated sampled-grating DBR laser transmitter**",** IEEE J. Select. Topics Quantum Electron., **8**, 1349 -1357 (2002).
[4] J.S. Barton, E.J. Skogen, M.L. Masanovic, S.P. DenBaars, L.A. Coldren, "Tailorable chirp using integrated Mach-Zehnder modulators with tunable sampled grating distributed Bragg reflector lasers", Proc. IEEE 18th International Semiconductor Laser Conference, 49 −50 (2002).
[5] R. A. Griffin, R. I Johnstone, R. G. Walker, J. Hall, S. D. Wadsworth, K. Berry, A. C. Carter, M. J. Wale, J. Hughes, P. A. Jerram, and N. J. Parsons, "10Gb/s optical differential quadrature phase shift key (DQPSK) transmission using GaAs/AlGaAs Integration", OFC'02, FD6-1 (2002).
[6] C. Rolland, "InGaAsP-based Mach-Zehnder modulators for high-speed transmission systems", OFC Technical Digest, 283 −284 (1998).
[7] B. Mason, G. A. Fish, S. P DenBaars, and L. A. Coldren, "Widely tunable sampled grating DBR laser with integrated electroabsorption modulator", IEEE Photn. Technol. Lett., **11**, 638-40 (1999).
[8] S. Lovisa, N. Bouche, H. Helmers, Y. Heymes, F. Brillouet, Y. Gottesman, K. Rao, "Integrated laser Mach-Zehnder modulator on indium phosphide free of modulated-feedback", IEEE Photon. Technol. Lett. , **13**, 1295 -1297 (2001).
[9] C. Lawetz, J.C. Cartledge, C. Rolland, J. Yu, "Modulation characteristics of semiconductor Mach-Zehnder optical modulators", J. of Lightwave Technol., **15**, 697-703 (1997).

Waveguide optical isolator integratable to LDs and SOAs

Tetsuya Mizumoto

Dept. of EEE, Tokyo Institute of Technology, 2-12-1 Ookayama Meguro-ku, Tokyo 152-8552, Japan, OITDA
Phone/FAX: +81-3-5734-2578, tmizumot@pe.titech.ac.jp

Abstract: The wafer bonding of magneto-optic garnet with III/V compound semiconductors was developed for integrating an optical isolator with semiconductor optical devices. The preliminary experiment is demonstrated in an interferometric isolator having a semiconductor guiding layer.
©2004 Optical Society of America
OCIS codes: (130.3120) waveguide isolator; (130.5990) semiconductor laser; (160.3820) rare earth iron garnet

1. Introduction

An optical isolator is the essential device that prevents unwanted reflection from disturbing the expected function of optical devices. In 1310nm and 1550nm wavelength bands, the most promising material for providing the nonreciprocal function needed for the optical isolator is a rare earth ion garnet because of its large figure of merit. Yttrium iron garnet $Y_3Fe_5O_{12}$, known as YIG, and a substituted iron garnet, such as Bi:YIG, are the most familiar group used for the optical isolator. They, however, have crystallographic properties dissimilar to III/V compound semiconductors. The growth of III/V compound semiconductors onto garnet crystals and vice versa has been a challenging task and still less developed [1,2]. This makes it difficult to integrate optical isolators with semiconductor-based optical active devices such as laser diodes and optical amplifiers. In order to alleviate this problem, we have developed a wafer bonding technique to provide a tight optical contact between garnet crystals and GaInAsP/InP wafers [3].

As for the structure of a waveguide optical isolator, a TE/TM mode conversion device, which is a waveguide version of a conventional bulk isolator, requires highly accurate control of waveguide birefringence, since the device requires the strict phase matching between orthogonally polarized guided modes [4]. Compared to the mode conversion device, an interferometric configuration has the advantage of rather large tolerance to the deviation of waveguide parameters, because it operates in a single polarization mode. We reported the measurement of the nonreciprocal phase shift in garnet waveguides that was essential for the interferometric waveguide isolator [5]. Also, the isolator operation was demonstrated in the interferometric isolator composed of the GaInAsP guiding layer on which an iron garnet was bonded [6].

In this paper, we describe a possible solution to the integration of an optical isolator with a semiconductor optical active devices.

2. Wafer bonding of iron garnet onto GaInAsP/InP wafer

The wafer bonding technique has been developed mainly for the combination of semiconductors. We applied this technique to the combination of iron garnets and III/V compound semiconductors. The wafer bonding is achieved by the following process; 1)adsorption of hydroxyl group, 2)formation of hydrogen bonding at room temperature and 3)dehydradation condensation at an elevated temperature in hydrogen atmosphere.

Table 1. Contact angle measurement for the evaluation of hydrophilicity

Treatment	Contact angle (deg)		
	InP	GaInAsP	Garnet (Ce:YIG)
w/o treatment	53.6	66.6	66.4
H_3PO_4, RT, 5min	10.7	48.0	5.0
$HCl:H_3PO_4(1:3)$, RT, 5min	--	50.5	--
$H_2SO_4:H_2O_2:H_2O$ (5:1:1), RT, 3min	10.8	--	--
O_2 plasma	--	14.8	25
O_2 plasma dipped in DI	5.6	<5.0	<5.0

For establishing a tight bonding, it is important to make wafer surfaces sufficiently hydrophilic prior to bonding. We examined the effectiveness of treatment for making hydrophilic surfaces of an iron garnet and III/V semiconductors[7]. Table 1 summarizes the results. The smaller the contact angle of water droplet, the more hydrophilic the surface is. The slight etching in H_3PO_4 is effective for an iron garnet. The oxygen plasma exposure

works well for all wafers investigated. Also, it should be noted that the wafer bonding of an iron garnet on a GaInAsP/InP wafer can be achieved with heat treatment at the temperature as low as 220ºC. Such a low temperature heat treatment is suitable for preventing the increase in the optical absorption of iron garnet.

Also, we checked the durability of bonded samples against several possible post fabrication processes, such as high temperature (600ºC) annealing, semiconductor wet etching, and plasma process. We concluded that the garnet bonded on a GaInAsP layer at 220ºC had sufficient durability against these post fabrication processes.
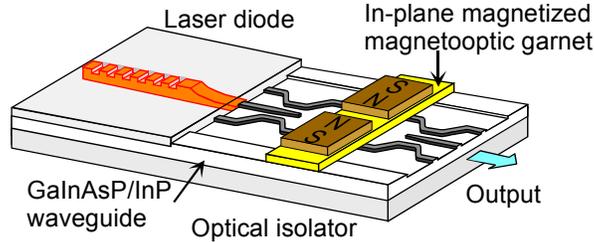

Fig. 1. Schematic drawing of an optical isolator integrated with a semiconductor laser

3. Optical isolator integratable to semiconductor optical devices

The optical isolator that has high compatibility with the integration of semiconductor optical devices has been proposed and developed. The structure of isolator is schematically shown in Fig.1. Its distinctive feature is that a GaInAsP layer is adopted for the guiding layer of isolator. All the waveguide isolators investigated so far are composed of a garnet guiding layer. Use of a semiconductor guiding layer enables us to introduce a selective growth technique that prepares an optical active region simultaneously with a passive waveguide. When we use a selectively-grown wafer, the waveguide stripes for active and passive devices are patterned in a single lithography process. Therefore, this approach is suitable for achieving the horizontal as well as vertical alignment of waveguide.

3.1 Principle of operation

The isolator shown in Fig.1 is composed of two tapered couplers, nonreciprocal phase shifters in two interferometer arms, and a reciprocal phase shifter in one of the arms. The reciprocal phase shift is provided by $\lambda/4$ arm length differences. The interferometer is designed so that the light waves propagating in two arms become in phase and 180º out of phase for forward and backward traveling waves, respectively. This can be accomplished by incorporating a 90º nonreciprocal phase shift and a 90º reciprocal one [8].

The nonreciprocal phase shift is experienced by TM modes guided in the waveguide that includes a magneto-optic material with its magnetization aligned transversely to the light propagation direction in the film plane. The phase shift is brought about by the first-order magneto-optic effect and is dependent on the thickness of guiding layer. A large phase shift is obtained when the waveguide is close to cutoff. When we use a Ce-substituted yttrium iron garnet $(CeY)_3Fe_5O_{12}$ and InP as an over-cladding and an under-cladding layer, respectively, the minimum length required for obtaining 90º nonreciprocal phase shift becomes 6.23mm at λ=1550nm for the guiding layer thickness of 0.4μm. Here, the guiding layer is assumed to be GaInAsP (λ_g=1250nm), and the Faraday rotation of $(CeY)_3Fe_5O_{12}$ is –4500deg/cm.
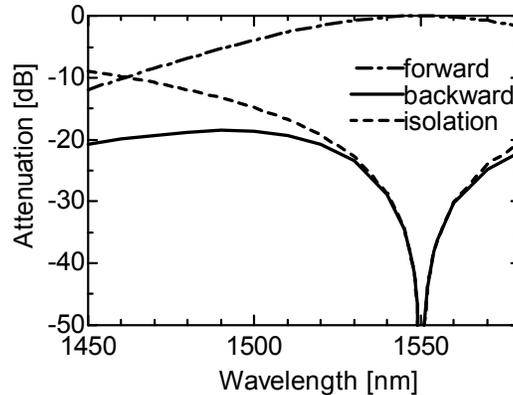

Fig. 2. Calculated wavelength dependence of the interferometric isolator. The wavelength dependence of material properties is taken into account.

3.2 Isolator performance

The wavelength dependence of isolator performance is calculated by taking into account the wavelength dependence of material properties like refractive indices and a Faraday rotation. As is shown in Fig.2, the insertion loss is less than 0.7dB, while the backward loss more than 23dB is obtainable in 1530 ~ 1565nm wavelength range.

In order to demonstrate the feasibility of the isolator shown in Fig.1, we fabricated the device using the 0.4μm-thick GaInAsP (λ_g=1250nm) guiding layer grown on a (100) InP substrate. The waveguide pattern was formed by using E-beam lithography and CH_4/H_2 reactive ion etching. $(CeY)_3Fe_5O_{12}$ grown on a (111) $(GdCa)_3(GaMgZr)_5O_{12}$ substrate was directly bonded onto the patterned GaInAsP waveguide. The performance of isolator is demonstrated in Fig.3. Since reversing the garnet magnetization is equivalent to reversing the propagation direction, we measured the change of transmittance between central ports of input and output couplers by reversing the external magnetic field direction. The measured isolation was approximately 5dB at 1550nm.

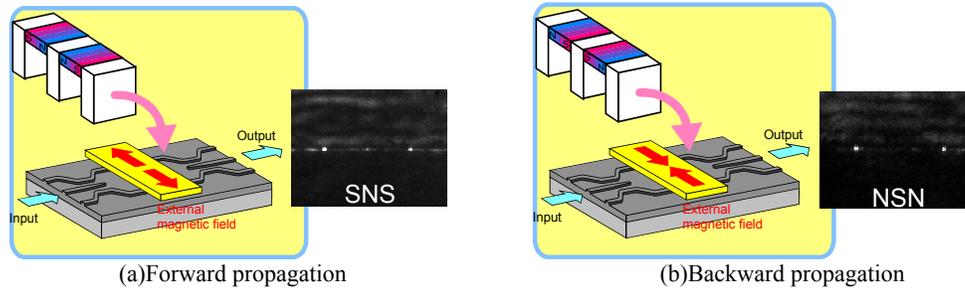(a)Forward propagation   (b)Backward propagation

Fig. 3. Measured performance of an optical isolator with a semiconductor guiding layer. Transmittance from the output port is dependent on the magnetization direction.

3.3 Device length and operating mode

We need a 6mm-long section for a 90º nonreciprocal phase shifter, when we use an InP under-cladding layer. The length should be reduced if we use the under-cladding layer with a lower refractive index. We succeeded in fabricating the GaInAsP waveguide with the selectively oxidized AlInAs cladding layer that has a refractive index of 2.45. The length of nonreciprocal phase shifter is dramatically reduced to 0.43mm using this waveguide structure.

A disadvantage of this isolator is that the nonreciprocal phase shift is ordinarily obtained for TM modes. This could be a problem for integrating with a semiconductor laser, as it usually emits a TE mode. This problem has been addressed by locally tailoring the magnetic domain structure to generate a nonreciprocal phase shift for TE modes [9]. Also, a polarization-independent configuration has been investigated [10].

4. Conclusion

The combination of garnet wafer bonding and selective growth is a promising approach for integrating isolators with LD and SOA. Also, the interferometric isolator is attractive, because the stringent phase matching is not required. Much effort is needed to accomplish the hard task of integrating the isolator with the optical active devices.

References
[1] M.Razeghi, P-L.Meunier, and P.Maurel, "Growth of GaInAs-InP multiquantum wells on garnet substrate by metalorganic chemical vapor deposition," J.Appl.Phys., **59**, 2261-2263 (1986).
[2] J.Haisma, B.H.Koek, J.W.F.Maes, D.Mateika, J.A.Pistrorius, and P.J.Roksnoer, "Hetero-epitaxial growth of GaAs on garnets," J.Crystal Growth, **83**, 466-469 (1987).
[3] M.Totoki, T.Mizumoto, K.Maru and Y.Naito, "Demonstration of direct bonding between InP and gadolinium gallium garnet (Gd₃Ga₅O₁₂) substrates," Electron. Lett., **30**, 1534-1536 (1994).
[4] T.Mizumoto, Y.Kawaoka and Y.Naito, "Waveguide-type optical isolator using the Faraday and Cotton-Mouton effects," Trans. IECE, **69**, 968-972 (1986).
[5] T.Mizumoto, K.Oochi, T.Harada and Y.Naito, "Measurement of optical nonreciprocal phase shift in a Bi-substituted Gd₃Fe₅O₁₂ film and application to waveguide-type optical circulator," J. Lightwave Technol., **LT-4**, 347-352 (1986).
[6] H.Yokoi, T.Mizumoto, N.Shinjo, N.Futakuchi and Y.Nakano, "Demonstration of an optical isolator, with a semiconductor guiding layer that was obtained by use of a nonreciprocal phase shift," Appl. Opt., **39**, 6158-6164 (2000).
[7] H.Yokoi, T.Mizumoto, M.Shimizu, T.Waniishi, N.Futakuchi, N.Kaida and Y.Nakano, "Analysis of GaInAsP surfaces by contact-angle measurement for wafer direct bonding with garnet crystals," Jpn. J. Appl. Phys., **38**, 4780-4783 (1999).
[8] F.Auracher, and H.H.Witte, "A new design for an integrated optical isolator," Opt. Commun., **13**, 435-438 (1975).
[9] M.Fehndrich, A.Josef, L.Wilkens, J.Kleine-Borger, N.Bahlmann, M.Lohmeyer, P.Hertel, and H.Dotsch, "Experimental investigation of the nonreciprocal phase shift of a transverse electric mode in a magneto-optic rib waveguide," Appl.Phys.Lett., **74**, 2918-2920 (1999).
[10] J.Fujita, M.Levy, R.M.Osgood,Jr., L.Wilkens, and H.Dotsch, "Polarization-independent waveguide optical isolator based on nonreciprocal phase shift," IEEE Photon. Technol. Lett., **12**, 1510-1512 (2000).

First experimental demonstration of a monolithically integrated InP-based waveguide isolator

Mathias Vanwolleghem, Wouter Van Parys, Dries Van Thourhout, Roel Baets
Department of Information Technology (INTEC), Ghent University – IMEC, Sint-Pietersnieuwstraat 41, B-9000 Gent, Belgium
mathias.vanwolleghem@intec.ugent.be
François Lelarge, Olivier Gauthier-Lafaye, Bruno Thedrez
Alcatel CIT, Route de Nozay, 91460 Marcoussis, France
Roel Wirix-Speetjens, Jo De Boeck
Interuniversitair Micro-Elektronica Centrum, IMEC vzw, Kapeldreef 75, 3001 Leuven, Belgium

Abstract: A theoretically predicted concept for a monolithically integrated optical waveguide isolator is experimentally demonstrated for the first time. Preliminary non-reciprocity measurements indicate isolation ratios in the range of the design values, proving the device's potential.
©2003 Optical Society of America
OCIS codes: (230.3240) Isolators; (230.3810) Magneto-optical devices; (250.5980) Semiconductor optical amplifier

1. Introduction

Increasing the integration level of planar lightwave circuits is one of the most important objectives of optical telecom component research. However, non-reciprocal optical components, such as optical isolators and circulators, are still escaping the possibility of monolithic integration. Up till now various concepts for a waveguide version of an optical isolator have been proposed and/or demonstrated experimentally [1]. Even though some of these designs achieve practical isolation ratios, they are all based on a ferrimagnetic garnet material system, making integration with standard III-V semiconductor devices rather cumbersome. Furthermore the most successful of these designs either make use of a TE-TM mode conversion principle or a Mach-Zehnder interferometer layout. The former suffer from very stringent phase matching requirements, while the latter have a large wavelength sensitivity and show poor fabrication tolerances. A few years ago, a novel concept for integrating optical isolation was theoretically proposed [2], [3]. Being basically a ferromagnetic metal-clad InP-based semiconductor optical amplifier (SOA), this novel isolator design is, in contrast with all previously reported isolator designs, simple to fabricate, shows a large wavelength operation range and allows for direct monolithic integration. We report on the first experimental demonstration of this novel isolator technology.
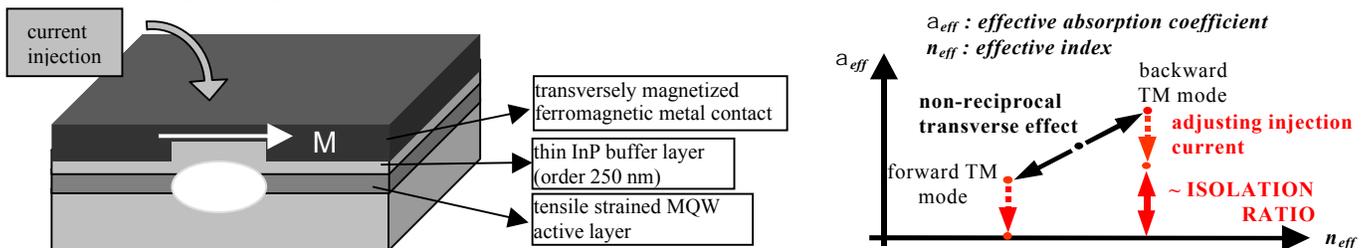
2. Principle of operation

Fig. 1: Schematic of the operation principle of the proposed isolator

An InP-based SOA with a transversely magnetized ferromagnetic metal contact close to the active core layer exhibits a non-reciprocal behaviour for propagating TM waveguide modes. This is due to the difference in reflection coefficient at the magnetized metal contact for the forward and backward propagating TM mode. This effect is known as the transverse magnetooptic (MO) Kerr effect [4] and, in a waveguide configuration, leads to direction-dependent dispersion equations for the guided TM modes. As a consequence both the effective absorption coefficient and the effective index of the guided TM modes become direction dependent. Therefore, by properly biasing the SOA (and hence using the magnetized ferromagnetic metal layer also as an electrical contact), this component can be made transparent in one direction while lossy in the other, hence isolating. This concept is illustrated in Fig. 1. It should be noted that of course the ferromagnetic properties of the contact allow a high remanent magnetization, or in other words, no external magnetic field is needed to keep the contact magnetized.

3. Design and Fabrication

A proper design of such an optical isolator first of all needs to take several key aspects into account. The chosen ferromagnetic metal must show both a sufficiently strong magneto-optic effect at the desired wavelength and a sufficiently low contact resistivity towards InP-based SOA's. The active layer of the SOA on the other hand must

provide sufficiently strong TM material gain, while at the same time suppressing TE gain (thereby avoiding gain saturation through amplification of spurious TE noise). We previously reported on the successful realization of the former two requirements [5], using a sputter-deposited $Co_{90}Fe_{10}$ ferromagnetic metal alloy. For the latter requirements, a tensile strained multi-quantum well (MQW) layer structure has been designed, optimizing the well and barrier thicknessess and their respective tensile and compensating compressive strain, in order to obtain optimum TM material gain at the desired wavelength of 1300 nm. To complete the design, the thicknesses of the InP buffer layer, and of both Separate Confinement Heterostructure (SCH) layers enclosing the MQW active layer, need to be optimized. Decreasing the thickness of the InP buffer layer, will increase the amount of TM light guided near the MO metal contact, and hence lead to an increased non-reciprocal effect but also to an increase in net optical absorption to be compensated in the forward direction. Varying the thicknesses of the SCH layers, on the other hand, can help to optimize the confinement of the TM light in the QW's, and minimize the needed QW material gain.

Using an in-house developed photonic simulation tool [6], extended with an algorithm for perturbational magnetooptic waveguide calculations, the needed TM QW material gain for forward transparency and the non-reciprocal TM optical absorption difference has been calculated in a sufficiently large portion of the 3D parameter space, formed by the three mentioned thicknesses. For every chosen InP buffer thickness, the corresponding optimal thickness combination for the SCH layers has been found by locating the maximum non-reciprocal effect within a region of theoretically achievable TM QW material gain. Figure 2 gives an example of such a calculation.
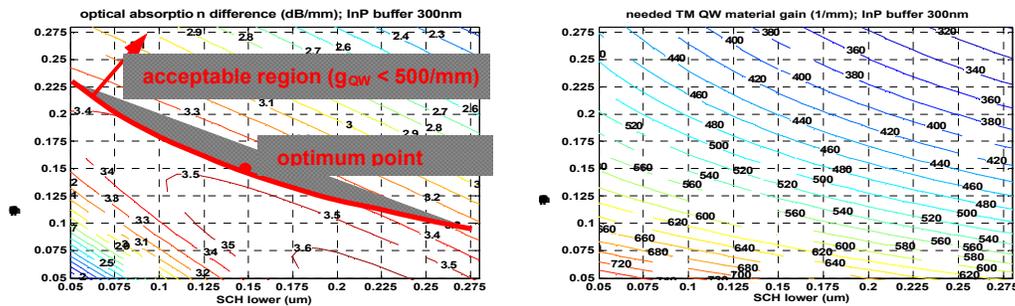

Fig. 2: simulation example of optical absorption difference and needed material gain; corresponding choice of SCH layers

Based on these kind of simulations three different prototype layer structures were grown using an optimized Gas Source Molecular Beam Epitaxy process. They were subsequently processed into ridge waveguides of varying widths (2 to 4 µm). The 50nm magnetron sputter-deposited ferromagnetic CoFe contacts have been defined through standard lift-off techniques. The top p-contact has been capped with an extra protective Ti/Au bilayer (40/110nm), while for the back contact AuGe has been used. Table 1 gives the grown layer structures and their simulated performance.

Table 1. layer structures of prototype GSMBE grown CoFe-clad tensile-strained MQW SOA's + simulation results

Layer	composition	*unstrained* l_g (μm)	strain e (%)	thickness (nm)	dopant (1/cm³)
metal	$Co_{90}Fe_{10}$	——————	0	50	
contact layer	$In_{0.53}Ga_{0.47}As$		0	15	$Be - 3*10^{19}$
contact layer	InGaAsP	1.17	0	100	$Be - 2*10^{19}$
buffer	InP		0	250 / 300 / 450	$Be - 2*10^{18} \rightarrow 5*10^{17}$
upper SCH	$In_{0.9}Ga_{0.1}As_{0.21}P_{0.79}$	1.03	0	170 / 150 / 100	nid
barrier (x4)	$In_{0.93}Ga_{0.07}As_{0.22}P_{0.78}$	1.06	+0.2	22	nid
well (x3)	$In_{0.48}Ga_{0.52}As_{0.78}P_{0.22}$	1.3	-1.1	11	nid
lower SCH	$In_{0.9}Ga_{0.1}As_{0.21}P_{0.79}$	1.03	0	155 / 150 / 120	nid
substrate	InP				$Si - 1*10^{18}$

expected isolation ratio (dB/mm)	1.8 / 3.5 / 5	max. needed material gain (1/mm)	300 / 500 / 650

4. Measurement of non-reciprocal ASE emission and characterisation

In order to prove the non-reciprocal behavior of a ferromagnetic metal-clad SOA, it suffices to observe the change in output of the TM Amplified Spontaneous Emission (ASE) under magnetization reversal in the CoFe layer. Reversing the transverse magnetization while observing the same output facet is equivalent to successively detecting forward and backward propagating light. Fig. 3 gives a schematic representation of the measurement setup. By looping the applied voltage over the coils of the electromagnet the magnetization in the CoFe layer is looped

through one complete hysteresis cycle. As a consequence of the magnetooptic non-reciprocal effect at play the detected TM ASE should emulate this hysteresis curve. Also, in order to prove that no magneto-mechanical effects take place, the TE ASE (which is insensitive to the MO effect) should be flat. The measurement example in Fig. 3 shows that both effects are clearly observed.
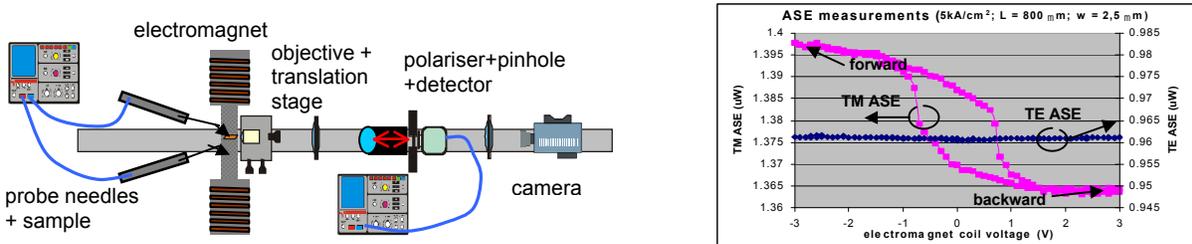

Fig. 3: experimental setup and measurement example

In order to quantify the non-reciprocal effect, the ratio of forward to backward TM ASE levels has been measured for different amplifier lengths and different injected current densities. All test samples have been processed with one tilted facet (10º), so as to avoid Fabry-Perot interference effects in the amplifier cavity. As a consequence, the ratio of the forward and backward output ASE can be very simply modeled by the following ratio of integrals

$$\int_0^L e^{(\Gamma g-(a-\Delta a/2))(L-x)}dx \bigg/ \int_0^L e^{(\Gamma g-(a+\Delta a/2))(L-x)}dx \qquad (1)$$

with Δa the non-reciprocal optical absorption difference and Γg–a the net modal loss, which is in a first approximation logarithmic dependent on the injected current density (Γg–$a = A\,lnJ – B$). Choosing A, B and Δa as fitting parameters and using a least-squares algorithm, (1) can be fitted to the ratios, measured for different current densities and different lengths L. All experiments have been carried under pulsed current conditions (pulse width 100ns, duty cycle 10%), in order to avoid thermal effects. Fig. 4 shows the results of such an experiment, performed on the 250 nm buffer thickness layer structure. A Δa of 1.25 dB/mm is obtained, approaching the design value.

– InP buffer thickness : 250nm
– ridge width : 2,5 µm; length: 500 and 800 µm
– least-squares fit of (1) to measured ratios:
  $A = 25/cm$; **$B = 100/cm$** in A lnJ – B as a fit for Γg–a
  $\Delta a = 3/cm = 1.25$ **dB/mm**
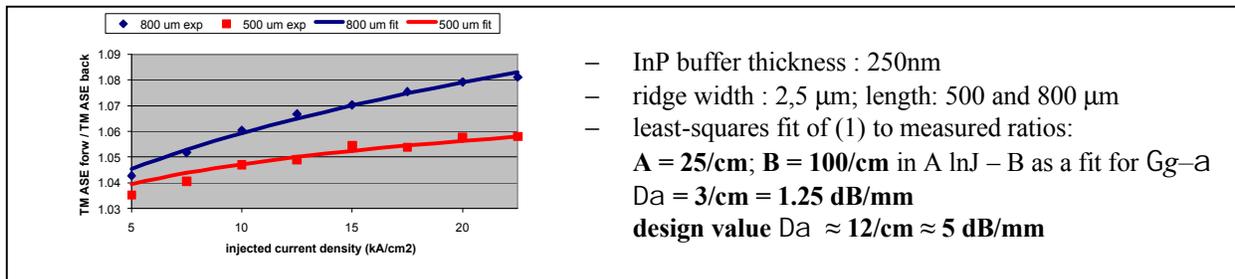 **design value** $\Delta a \approx 12/cm \approx 5$ **dB/mm**

Fig. 4: TM ASE ratio measurements on a 250 nm InP buffer sample (width = 2,5 µm)

5. Conclusion

We have designed, fabricated and successfully tested for the first time a novel concept for monolithic integration of optical isolation. These first results prove the soundness of the novel technology. It is believed that with further optimization of the layer structure practical isolation ratios in the range of 20 dB are achievable.

References
[1] R.M. Osgood et al., "Progres in Integrated Optical Isolators", in Integrated Photonics Research 2000, OSA Technical Digest, pp. 274.
[2] M. Takenaka and Y. Nakano, "Proposal of a Novel Semiconductor Optical Waveguide Isolator", Proc. of 11th Intern. Conf. on Indium Phosphide and related materials, pp.289-292, May 1999.
[3] W. Zaets and K. Ando, "Optical waveguide Isolator based on non-reciprocal loss/gain of amplifier covered by ferromagnetic layer", IEEE Photon. Technol. Lett., Vol. 11, pp. 1012-1014, August 1999
[4] A.K. Zvezdin and V.A. Kotov, *Modern Magnetooptics and Magnetooptical Materials*, IoP Publishing, 1997
[5] M Vanwolleghem et al., "Ferromagnetic-metal-based InGaAs(P)/InP optical waveguide isolator: electrical and magneto-optical characterisation", in Proceedings of 2002 IEEE/LEOS Benelux Chapter, Amsterdam, pp. 282-285
[6] CAMFR, freely available at http://www.sourceforge.net/camfr

CWDM vertical-cavity surface-emitting laser array spanning 140 nm of the C, S, and L fiber transmission bands

Jon Geske and John E. Bowers

ECE Department, University of California, Santa Barbara, CA 93106, USA

geske@ece.ucsb.edu

Devin Leonard and Michael MacDougal

Presently with: Imaging Division, Rockwell Scientific Company, 5212 Verdugo Way, Camarillo, CA 93012, USA

Abstract: We demonstrate record wavelength span from an 8-channel WDM VCSEL array operating CW to 65°C from 1470 to 1610 nm with precise 20-nm channel spacing. Devices are fabricated using nonplanar wafer bonding and fully-oxidized DBRs.

©2004 Optical Society of America

OCIS codes: (060.2380) Fiber optics sources and detectors; (250.7260) Vertical cavity surface emitting lasers

1. Introduction

Vertical-cavity surface-emitting lasers (VCSELs) are of great interest due to their advantages in low-cost manufacturing and packaging. These qualities are compatible with the emerging market for wideband coarse wavelength division multiplexing (CWDM) in low-cost, high-performance, optical networks spanning the entire low-loss and low-dispersion fiber transmission window from 1470 to 1610 nm. Integrating the CWDM sources in a wafer-scale fabrication process can achieve great cost savings for this application. Much work has been done on attaining wide wavelength span WDM VCSEL arrays operating near 1100 nm [1]. Wide wavelength span VCSEL arrays near 1550 nm have been more elusive however due to the challenges of fabricating high quality VCSELs in this wavelength window.

In wide wavelength span VCSEL arrays it is important to maintain uniform device performance across the elements of the array. Adjusting the cavity mode laterally across the surface of the wafer is sufficient to achieve small wavelength changes across a VCSEL array [2], however to keep the device properties uniform, controlling the alignment between the gain peak and the cavity mode is necessary in wide wavelength span CWDM VCSEL arrays. One way to maintain this alignment is to integrate multiple active regions across the surfaced of the wafer so different wavelength channels in the WDM array can utilize different active regions for gain.

In a previous report, we demonstrated a new technique, nonplanar wafer bonding, that is capable of simultaneously integrating multiple active regions across a wafer surface in a single wafer bonding step [3]. We reported the use of this technique to fabricate long-wavelength arrays with a narrow wavelength span using traditional AlGaAs distributed Bragg reflectors (DBRs) [4].

In this paper we demonstrate record wavelength span from an eight-channel long-wavelength WDM VCSEL array covering 140 nm from 1470 to1610 nm and operating CW above 65 °C. Precise 20-nm wavelength spacing and single transverse mode operation is maintained for all channels. These devices are pumped using a fiber-coupled 980-nm pump laser, a technique compatible with commercialized long-wavelength VCSELs [5]. This result is made possible by the simultaneous application of a new, simplified nonplanar wafer bonding procedure and through the use of broadband fully oxidized GaAs/AlOx DBRs [6].
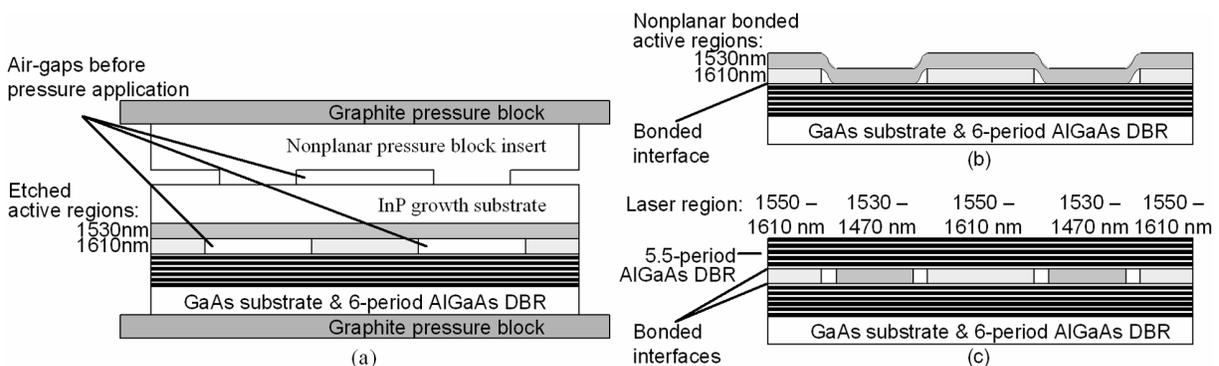

Fig. 1. Process-flow cross-section schematic of a wafer section showing: (a) nonplanar pressure block against back of step-etched InP active region wafer in bonding fixture, (b) VCSEL active regions bonded to AlGaAs DBR with InP growth substrate removed, (c) complete VCSEL array structure after bonding second AlGaAs DBR and removing GaAs substrate.

2. Array fabrication

The array fabrication process begins with two strained periodic-gain multi-quantum-well long-wavelength VCSEL active regions grown in a vertical stack on an InP wafer. The active regions have an optical-cavity length of 2.5 wavelengths at 1530 and 1610 nm and have photoluminescence peaks at 1480 and 1560 nm, respectively. In addition, the active regions have a three-period superlattice on one side for fine wavelength control in the second axis of the final two-dimensional array [4].

   Nonplanar wafer bonding is used to bond the active regions to the bottom DBR of the VCSEL structure in a procedure that closely follows the technique detailed in Reference [3] and outlined here for clarity. First, the active-region wafer surface is etched with a step-shaped profile to reveal a different active region on each step level. The wafer surface is then placed in contact with an AlGaAs DBR mirror grown on a GaAs wafer. The active-region epitaxial layers are wafer bonded to the AlGaAs layers by applying pressure and heat in a graphite fixture. A reusable nonplanar pressure block insert is used adjacent to the InP substrate in the bonding fixture. Fig. 1(a) depicts the nonplanar pressure block against the backside of the InP active region wafer before pressure is applied. The nonplanar pressure block is fabricated from InP and designed to have step heights exactly equal to those on the front of the active-region wafer thus causing the wafer to conform to the AlGaAs DBR wafer surface. In this way, both active regions exposed on the surface of the InP wafer are transferred to the planar surface of the AlGaAs DBR wafer. After bonding the wafers together, the original InP growth substrate is removed, leaving the active regions attached to the AlGaAs DBR as depicted in Fig. 1(b). The excess active-region material is removed, revealing a different active region at each lateral position along the first dimension of the AlGaAs mirror. At this point, the original 3-period superlattice that was grown on each active region is etched with a step-shaped profile to trim the cavity resonance of each of the two separate active regions in the second dimension of the wafer surface. This superlattice etch forms the location of channels 1-4 on the 1530-nm active region and channels 5-8 on the 1610-nm active region. A second AlGaAs DBR is bonded by traditional planar semiconductor-direct bonding to create the final wafer structure shown in cross-section view in Fig. 1(c).
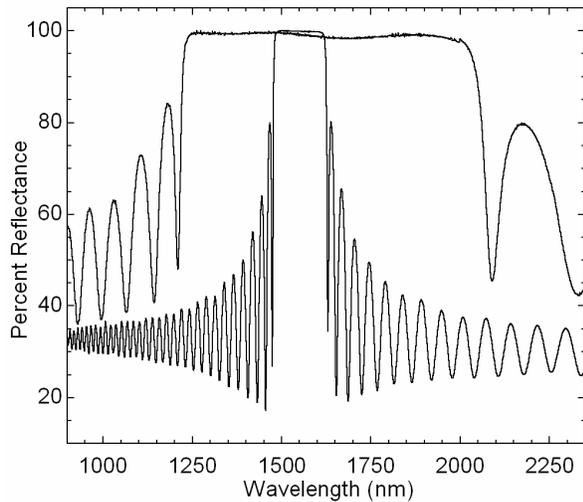

Fig. 2. Reflectivity spectrum of a 7-period fully-oxidized back mirror superimposed with reflectivity spectra from a traditional 40-period GaAs/AlAs DBR.
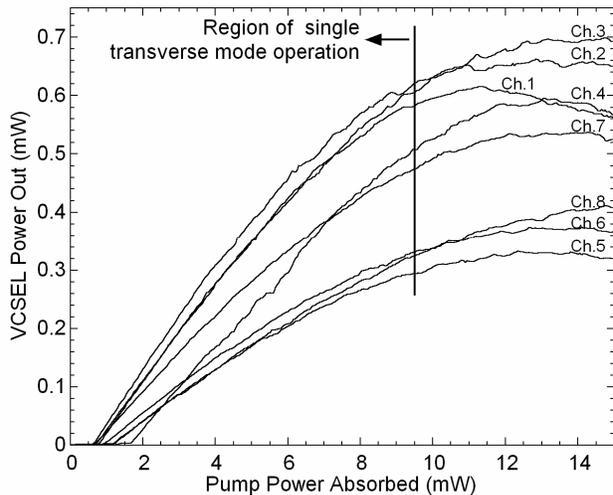

Fig. 3. VCSEL power out vs. pump power absorbed for all eight wavelength channels of a single WDM array measured at 20 °C.

   In order to generate the wide reflectivity bandwidth required for a 140-nm wide WDM VCSEL array we use 5.5-period and 6-period fully-oxidized GaAs/AlOx top and bottom DBRs respectively in this VCSEL structure. The mirrors are designed to have peak reflectivity at 1540 nm after the conversion of the AlAs to AlOx by wet thermal oxidation [6]. Oxidation occurs laterally from etched trenches in a steam environment at 430 °C for 16 minutes. Fig. 2 shows the broad area reflectivity of a 7-period oxidation calibration mirror after oxidation. The rippled appearance of the stop-band is believed to be an artifact of the broad area reflectivity measurement. The reflectivity spectrum of a traditional 40-period GaAs/AlAs DBR is superimposed for comparison. A final 1540-nm anti-reflection coating is used on the surface of the device to increase the light coupled out of the VCSEL array.

3. Device Results

The final structure is an eight-channel, two-dimensional, WDM VCSEL array. The die-to-die center spacing is 1 by 1.25 mm. Channels groups 1-4 and 5-8 are spatially separated by 500 μm with an inter-channel spacing of 250 μm. All channels operate CW above 65 °C. The array is optically pumped with a 980-nm pump laser and each device has a 980-nm pump absorption efficiency of about 90 %. Fig. 3 shows the superimposed VCSEL power out vs. pump power absorbed for all eight wavelength channels measured at 20 °C from a single WDM VCSEL array. The device array has uniform thresholds of 1.185 +/- 0.5 mW and differential efficiencies that vary between 13.8 and 7.4 %. All channels operate with a side-mode suppression ratio (SMSR) in excess of 35 dB until an absorbed pump power of 9.5 mW. Fig. 4 shows the superimposed VCSEL emission spectra at a constant absorbed pump power of 14 mW for a second device array designed specifically for single-mode operation. These devices maintain a 45-dB SMSR at all pump powers and have less than 2-dB output power variation at this constant pump power.

Variation in device properties can be attributed to several factors. Wavelength channels 1-4 and 5-8 each use an active region with a peak gain near 1480 and 1560 nm respectively. Thus there is some natural variation in threshold and the rollover point due to the differing gain peak and cavity mode offset. However, there is more variation than can be attributed to this offset alone and work remains to be done to refine this integration technique.
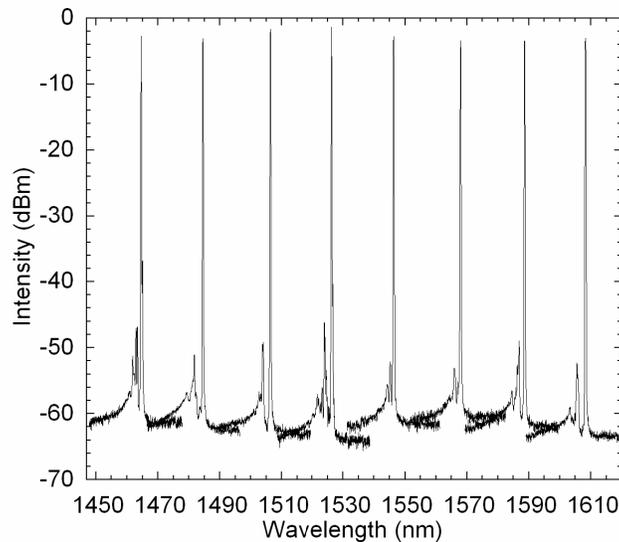

Fig. 4. Superimposed VCSEL emission spectra from the WDM VCSEL array measured at a constant absorbed pump power of 14 mW at 20 °C.

4. Conclusions

We have demonstrated record wavelength span from a long-wavelength WDM VCSEL array covering 140 nm from 1470 to 1610 nm. The devises operate beyond 65 °C and exhibit SMSR in excess of 45 dB. These devices represent a significant advance in the development of single chip sources for future use in CWDM optical network applications.

5. References

1   M. Arai, T. Kondo, A. Matsutani, T. Miyamoto, F. Koyama, "Growth of highly strained GaInAs-GaAs quantum wells on patterned substrate and its application for multiple-wavelength vertical-cavity surface-emitting laser array," IEEE J. Select. Topics Quantum Electron., 8, 811-16 (2002).
2   A. Karim, P. Abraham, D. Lofgreen, Y. J. Chiu, J. Piprek, and J. E. Bowers, "Wafer-bonded 1.55μm vertical cavity laser arrays for wavelength division multiplexing," Electron. Lett., 37, 431-432 (2001).
3   J. Geske, V. Jayaraman, Y. L. Okuno, and J. E. Bowers, "Vertical and lateral heterogeneous integration," Appl. Phys. Lett., 79, 1760-1762 (2001).
4   J. Geske, Y. L. Okuno, D. Leonard, and J. E. Bowers, "Long-wavelength two-dimensional WDM vertical cavity surface-emitting laser arrays fabricated by nonplanar wafer bonding," IEEE Photon. Technol. Lett., 15, 179-181 (2003).
5   V. Jayaraman, T. Goodnough, T. Beam, F. Ahedo, and R. Maurice, "Continuous-wave operation of single-transverse-mode 1310-nm VCSELs up to 115 degrees C," IEEE Photon. Technol. Lett., 12, 1595-7 (2000).
6   M. H. MacDougal, P. D. Dapkus, A. E. Bond, C. Lin, and J. Geske, "Design and Fabrication of VCSEL's with AlxOy-GaAs DBR's," IEEE J. Select. Topics Quantum Electron., 3, 905-915 (1997).